Faculté des Sciences

Département de physique - Unité de recherche CESAM

Group for Research and Applications in Statistical Physics

Assembly and manipulation of floating components at liquid interfaces

From controllable particles to capillary tweezers

Dissertation présentée par

Jean Metzmacher

en vue de l'obtention du grade de

Doctorat en Sciences

Année académique 2022-2023

Acknowledgements

Merci à toutes les personnes avec lesquelles j'ai pu collaborer ou échanger lors de mes activités d'encadrements. Merci à Christophe, le gourou du jeu de rôle, à l'estomac d'une ponctualité remarquable. Merci à Jacqueline, notre maman poule, PX, Pauline, Jean-Marc et Yves-Eric.

Enfin, comme il arrive aux doctorants de sortir des bureaux et des labos, il me reste encore 2 groupes importants de personnes à remercier. Merci à mes amis, du plus grand au plus petit, qui sont à mes côtés depuis des années. Même si on a pas toujours l'occasion de se voir aussi souvent qu'on le voudrait, je sais que je peux compter sur vous. Merci à ma famille qui m'a aussi toujours soutenu malgré les coups du sort auxquels elle a dû faire face.

Abstract

At the surface of a liquid, the molecules have more energy than those in the bulk. This gives birth to surface tension. In our everyday life, many manifestations of this phenomenon can be observed. The spherical shape of drops and the ability of some insects to walk on water are some examples.

In this thesis, we use surface tension and the forces that arise from it to assemble and manipulate floating components. We first show that a floating object of controllable shape can modify its interactions with its neighbours. With such objects, we form a reconfigurable self-assembly that is able to switch reversibly from one structure to another. By modifying somewhat the geometry of the components, we improve this self-assembly by giving it the ability to perform a rotational movement. Then, we show that the surface of a liquid can be shaped in a given area to manipulate floating particles. We create actuators that can be combined to form capillary tweezers. With these tweezers, we manipulate floating particles, both solid and liquid, without direct contact. The results obtained in this work can be used to create functional structures and self-assembled robots. They also offer a new technique for manipulating floating particles of any kind.

Résumé

À la surface d'un liquide, les molécules ont une énergie plus grande que celles qui sont au sein du liquide. Cela donne naissance à la tension de surface. Dans notre vie quotidienne, beaucoup de manifestations de ce phénomène peuvent être observées. La forme sphérique des gouttes et la capacité de certains insectes à marcher sur l'eau en sont des exemples.

Dans cette thèse, nous utilisons la tension de surface et les forces qui en découlent pour assembler et manipuler des composants flottants. Nous montrons d'abord qu'un objet flottant de forme contrôlable peut modifier ses interactions avec ses voisins. Avec ces objets, nous formons un auto-assemblage reconfigurable, capable de passer réversiblement d'une structure à une autre. En modifiant quelque peu la géométrie des composants, nous améliorons cet auto-assemblage en lui conférant la capacité d'effectuer un mouvement de rotation. Ensuite, nous montrons que la surface d'un liquide peut être déformée dans une zone donnée pour y manipuler des particules flottantes. Nous créons des actuateurs pouvant être combinés pour former des pinces capillaires. Avec ces pinces, nous manipulons sans contact direct des particules flottantes, aussi bien solides que liquides. Les résultats obtenus dans ce travail peuvent être utilisés pour créer des structures fonctionnelles et des robots auto-assemblés. Ils offrent aussi une nouvelle technique permettant de manipuler des particules flottantes quelque soit leur nature.

Publications

This thesis led to the publication of two articles that partially cover Chaps. 2 and 3 respectively.

J. Metzmacher, G. Lagubeau, M. Poty and N. Vandewalle. Double pattern improves the Schlieren methods for measuring liquid–air interface topography. *Exp. Fluids*, **63**, 120 (2022).

J. Metzmacher, M. Poty, G. Lumay and N. Vandewalle. Self-assembly of smart mesoscopic objects. *Eur. Phys. J. E*, **40**, 1 (2017).

Contents

0 Introduction

The Earth welcomes a great variety of living species, each one with its own specificities. To survive, lots of different strategies have been developed. Among the animal reign, Homo Sapiens became the dominant species thanks to his ability to build tools and devices. He started by working with raw materials that he found directly in his environment, like wood, stones and bones. Then, step by step, he learned to build elaborated tools and to transform these natural materials to produce, for examples, bronze or iron tools. Nowadays, Homo Sapiens is able to create a large variety of synthetic compounds and to build devices that range from microscopic chips to large structures like buildings or satellites.

With the enhancement of knowledge and technologies, more and more components of various types, shapes and scales have to be manipulated. Indeed, before any structure or device can be built, the parts that will compose it have to be moved and assembled accurately. Lots of manipulation techniques have been developed and the variety of objects that man is now able to handle with its tools is impressive. Hoists can lift large and heavy parts, robotic arms can grab dangerous substances and bring back materials from hostile environments, optical tweezers can trap and manipulate cells without the use of a solid body [1, 2, 3]. Some examples are illustrated in Fig. 1.
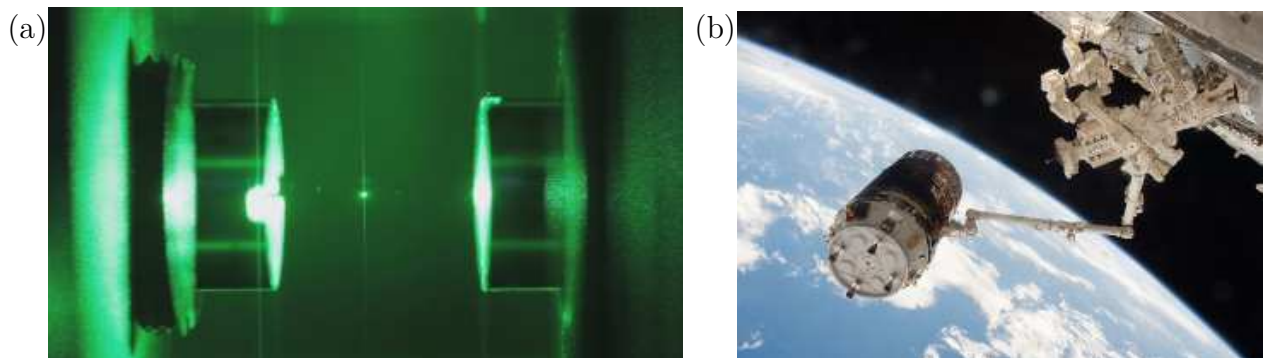
Fig. 1: Two examples of manipulation tools. (a) Optical tweezers trapping a glass nanoparticle. Picture by James Millen [4]. (b) The robotic arm of the International Space Station grapples the Japanese HTV-6 cargo vehicle. Picture by the NASA [5].

Currently, powerful machines have been developed to manipulate large and heavy objects and chemistry provides molecular self-assembly to efficiently fabricate structures from molecules [6, 7, 8]. However, to handle nano-sized components and mesoscopic objects (with sizes ranging from micrometres to millimetres), some reliable methods exist but there are not really efficient and the new/future technologies, as microelectronics, photonics or nanoscience, need to manipulate particles at these scales.

Millimetre and sub-millimetre-sized components are commonly manipulated by pick-and-place robots. Thanks to them, current electronics devices can be assembled with a high accuracy and a satisfying throughput despite being serial [9]. However, the throughput depends on the placement accuracy. If the size decreases, the difficulty to handle a component with precision increases and the throughput drops. Moreover, adhesive forces become significant for micrometre-sized objects and stiction problems will arise [10]. New technologies also required more complex devices with heterogeneous parts and an increasing number of components.

An interesting alternative to current micromanipulation techniques is self-assembly [11, 12, 13]. It can be defined as the spontaneous organisation of components into ordered patterns or structures without human intervention [11]. The assembly of these components is caused by interaction forces that exist between them. These forces can be of various types, with different ranges: magnetic, electric, capillary, ... By its nature, self-assembly is a parallel process and is therefore well adapted to large amount of components. It can also be applied to a large variety of particles, ranging from nanometre to millimetre scales. Moreover, as it results from interaction forces between the components, self-assembly avoids direct manipulation (and so stiction problems) and enables to handle easily deformable objects like drops or bubbles.

A self-assembly is usually characterized by the type of interaction force between the particles and, for example, we talk about magnetic self-assembly when the forces between the components are magnetic forces. Electric and magnetic interactions are well known but required that the components are made in a material having specific properties. Moreover, the particles have to be able to move to assemble and an external agitation, such as shaking or stirring, could be necessary. In this thesis, we choose to focus on capillary interactions between floating particles because they offer several advantages. On a liquid surface, objects can move and assemble without external agitation. There is no restriction on the material used to build the components, as long as the components are small. Indeed, as we will explain in Chap. 1, even dense materials can float if the particle is small enough (usually millimetre-sized). Moreover, capillary interactions also arise between bubbles or drops.

The aim of this thesis is to manipulate and assemble mesoscopic components floating on a liquid surface. Being able to handle accurately such particles is of great interest in physics. Indeed, the properties of a material can depend strongly on its structure. For example, diamond and graphite are both made of carbon atoms but their distinct crystal structures give them different physical properties. Assemble components into specific and controllable patterns enables to build new functional materials that can lead to new technologies and applications.

The relevant question raised in this thesis is how to interact with floating particles to assemble and manipulate them. The proposed answer is to deform the liquid surface in order to exploit capillary interactions. Two complementary strategies are developed. In the first one, controllable components are built to create specific deformations of the interface in their neighbourhood. In the second one, passive and simple components are considered and the liquid surface around them is deformed by local actuators. Fig. 2 summarizes graphically the content of this thesis.
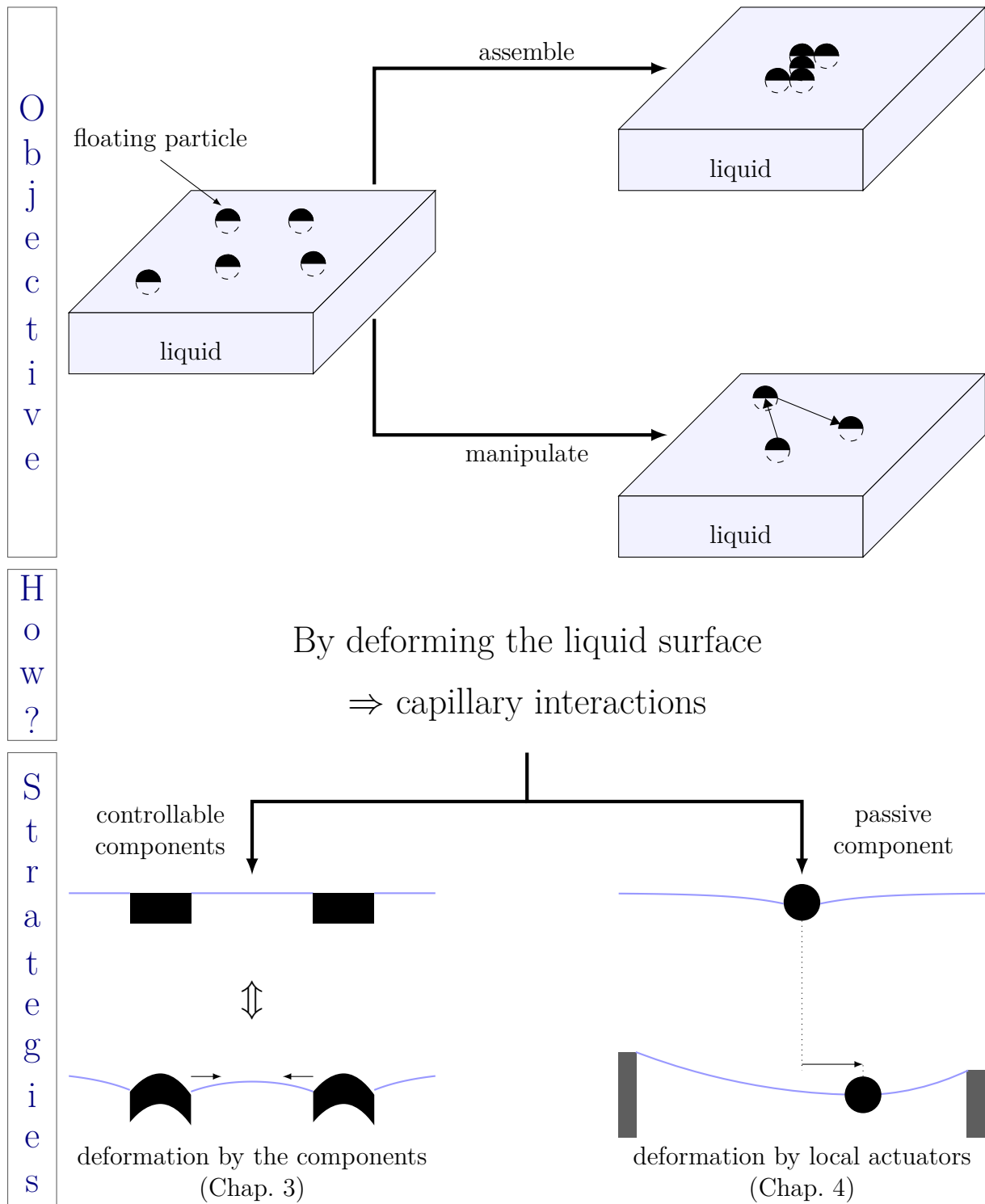
Fig. 2: Graphic representation of the work done is this thesis. Floating mesoscopic components are manipulated or self-assembled. To do that, two strategies deforming the liquid surface and exploiting the resulting capillary interactions are proposed. In the first one, the interface is deformed by controllable components and, in the second one, by local actuators.

Chap. 1 presents the physical phenomena that are at the origin of capillary interactions. We introduce the concept of surface tension and explain how it induces forces between particles that deform a fluid interface. Then, we show how the interaction can be computed for simple and complex particles. Chap. 2 is focused on the measurement of the interface topography. As we propose to manipulate floating components by deforming the liquid surface, we need a reliable and direct method to observe and quantify these deformations. We start by

presenting briefly the different types of existing methods. Then, we describe more in details a simple and classical technique that is well adapted to our needs and we discuss some improvements that have been proposed by others. After that, we present a new method that we developed to extend the range of slopes that can be measured. The following of this thesis focuses on how the interface can be shaped to induce capillary interactions to manipulate and assemble components. Chap. 3 is dedicated to our first strategy. It starts by presenting controllable components that are able to create specific deformations of the liquid surface in their neighbourhood and to change their interactions by the application of an external field. Then, we show how these particles can reversibly self-assemble and how they can be transform into rotating swimmers. Chap. 4 describes our second strategy. We develop a local actuator that creates a controllable deformation of the interface and we show how such actuators can be combined to build capillary tweezers. We demonstrate that this device is able to shape the interface around a simple particle to manipulate it. To end this thesis, Chap. 5 draws a general conclusion and suggests some possible future works.

1 State of the art

In our everyday life, matter can be found in three well-known states: solid, liquid and gas. Each one has its own physical properties. In a gas, the molecules are weakly linked and can almost freely move whereas in a solid the attractive forces between molecules are strong and they can only oscillate. Liquid is somewhat an intermediate case: cohesive forces are not strong enough to prevent molecules to move but are strong enough to keep them in a fixed volume. An interface exists between the liquid and the external environment. However, because attractive forces are not strong enough to prevent the molecules to move, a liquid flows and its interface is easily deformed. This ability to deform is the key ingredient of this work. The deformations of the surface of a liquid induce particular forces between floating objects and this is a way to control and manipulate them. In what follows, I will explain the origin of these forces and what we know so far about them.

1.1 Surface tension

In a liquid, a molecule undergoes attractive forces from all its neighbours. In the bulk, it is completely surrounded by other molecules and so, is attracted equally in all directions. At the surface, the situation is however different. A molecule has only neighbours in a half space as illustrated in Fig. 1.1. As this molecule undergoes less attraction forces, it has a higher energy than a molecule located in the bulk. This difference of energy gives birth to surface tension.

From this microscopic point of view, surface tension γ can be defined as the excess of energy of a molecule at the surface by unit of area [14]. If the bond energy per molecule in the bulk is $-\epsilon$ and if the size of the molecule is d, it can be estimated by

$$\gamma \approx \frac{\frac{-\epsilon}{2} - (-\epsilon)}{d^2} \tag{1.1}$$

and therefore

$$\gamma \approx \frac{\epsilon}{2d^2} \tag{1.2}$$

because a molecule at the surface loses roughly half of its neighbours. Depending on the molecules, the bond energy has different origins: van der Waals forces, ionic bonds, hydrogen bonds, ... In the case of water, the bond energy is particularly high because of hydrogen bonds and $\gamma \approx 0.072 \, \text{J/m}^2$.
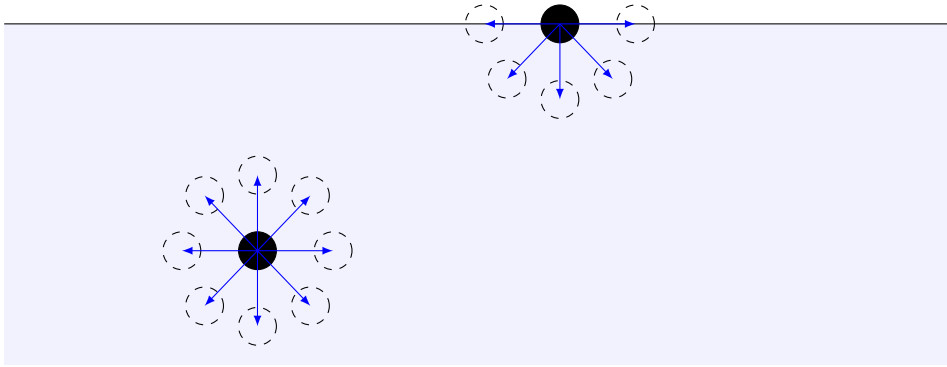
Fig. 1.1: A molecule in a liquid undergoes attractive forces (blue arrows) from all its neighbours. When the molecule is at the surface, it has only neighbours in a half space. It undergoes fewer interactions and has a higher energy than a molecule in the bulk.

Although surface tension originates from the microscopic world, it affects the macroscopic world. Manifestations of this phenomenon can be seen in our everyday life and in nature. If we fill carefully a glass with water, we can put a volume of water that is a bit larger than the volume of the glass. The surface of the water bends but the liquid does not fall outside of the glass because the interface behaves like an elastic membrane thanks to surface tension. The spherical shapes of drops and bubbles are another effect of surface tension. As a molecule at the surface have higher energy than one in the bulk, such a shape minimizes the energy of the drop/bubble because sphere is the volume that has the smallest surface area. Some animals use surface tension to move around. If we observe a pool, we may see some insects that walk on the surface. Their feet bend the interface and their weight is supported by surface tension [15, 16]. You may also find floating insects that develop other strategies as the water lily leaf beetle larva *Pyrrhalta*. It climbs menisci by arching its back and exploiting attractive forces resulting from surface tension [17]. Some of these examples are shown on Fig. 1.2.

(a) (b)

Fig. 1.2: Manifestations of surface tension in nature. (a) A bubble of soap water at the top of a syringe. The spherical shape of the bubble results from surface tension. The diameter of the tip of the syringe is 4 mm. (b) Insect walking on water. Its weight is supported by surface tension.

From the point of view of thermodynamics, γ can be defined as the free energy per unit of area [14], *i.e.*

$$\gamma = \left(\frac{\partial F}{\partial A}\right)_{T,V,N} \tag{1.3}$$

where F is the free energy, A is the surface area, T is the temperature, V is the volume of the system and N is the number of molecules. The dimension of this quantity is mass per time squared and it can be expressed in J/m². Alternatively, surface tension can be expressed in N/m. Therefore, it also corresponds to a force per unit length [14, 18]. Eqs. (1.2) and (1.3) give only the intensity of this force, not its direction.

From Fig. 1.1, we can think that surface tension is perpendicular to the interface, which is not the case. It is a force whose effect can be seen at the macroscopic scale. Simple experiments can be performed to show its effect and determine its direction. For example, consider a rectangular frame with one edge that is able to move. We immerse this frame in soapy water and then remove it. A film of soapy water is captured in the rectangular area of the frame. If we displace the mobile edge to increase the surface of the soapy film and release it, the mobile edge is pulled back towards the opposite edge, decreasing the surface as shown in Fig. 1.3. As a system will always try to minimize its energy, this simple experiment just shows that the soapy film has a lower energy when its surface is small. Molecules at the surface of the film having more energy than molecules in the bulk, an increase of the surface increases the energy of the film. The spontaneous displacement of the mobile edge to reduce the surface is a macroscopic manifestation of surface tension. In this example, we can see that the surface tension acts like a force that is parallel to the film and directed toward the inside of the film, like the tension in an elastic membrane. That is exactly why this effect is called "surface tension": the surface of liquids behaves like an elastic membrane. Mathematically, we can obtain γ by evaluating the work dW needed to increase the surface of the film by moving the mobile edge on a distance dx [14], *i.e.*

$$dW = 2\gamma l dx \tag{1.4}$$

where l is the length of the mobile edge and the factor 2 takes into account that two interfaces soapy water/air pull the soap film.
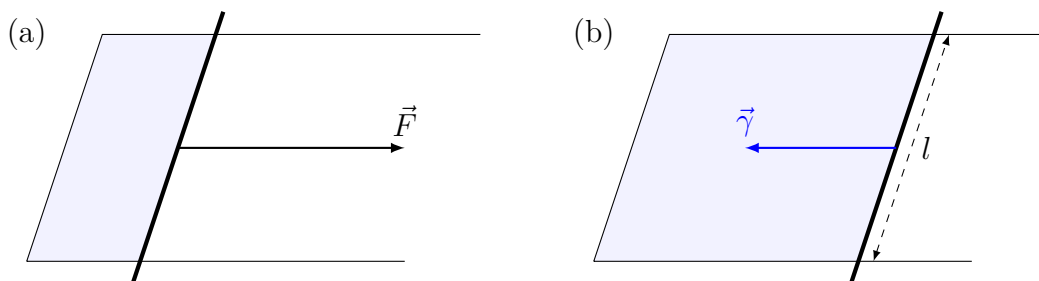
Fig. 1.3: A soapy film is trapped on a rectangular frame with a mobile edge. (a) The mobile edge is pulled with a force $\vec{F}$ to increase the surface of the film. (b) When the mobile edge is released, it is pulled back by the surface tension $\vec{\gamma}$ in the film.

Some solutions have been proposed to match microscopic and macroscopic approaches [18, 19] and Marchand et al. [18] propose an elegant explanation to this problem. To determine the orientation of surface tension in the microscopic approach, we need to define a proper sub-system and to consider all the forces acting on this sub-system. On Fig. 1.1, only the attractive forces on the molecules are taken into account but there are repulsive forces too. Both types of force have different ranges and that is at the origin of surface tension [18, 19]. Attractive forces are long-range and strongly anisotropic. They are affected by changes in the neighbourhood of the molecule. On the contrary, repulsive forces are short-range and almost isotropic. At first approximation, they can be considered as contact forces and are almost independent of the neighbourhood of the molecule [18].

Firstly, consider the forces exerted on layers of fluid parallel to the interface at different depths as illustrated in Fig. 1.4 (a). Such a layer is at equilibrium. However, there is no up-

down symmetry around an horizontal layer. Therefore, to ensure the equilibrium, attractive and repulsive forces have to balance. As attractive forces are long-range, they increase with depth as density increases and so, repulsive forces increase too.

Secondly, consider forces exert on a layer of fluid perpendicular to the interface as illustrated in Fig.1.4 (b). In this case, there is a symmetry around the layer and the equilibrium is guaranteed. There is no reason that attractive and repulsive forces have the same magnitude. Repulsive forces being isotropic, their horizontal and vertical components at a given depth should be equal in magnitude. Therefore, the repulsive forces on the vertical fluid layer should increase with depth as in Fig.1.4 (a). By contrast, attractive forces on the vertical layer have a much lower dependence on the depth [18]. In particular, the attractive force near the surface is almost equal to the one in bulk and larger than the repulsive force. So, the balance of repulsive and attractive forces gives a net attractive force that stretches the interface as it is observed at the macroscopic scale (see Fig. 1.4 (c)).
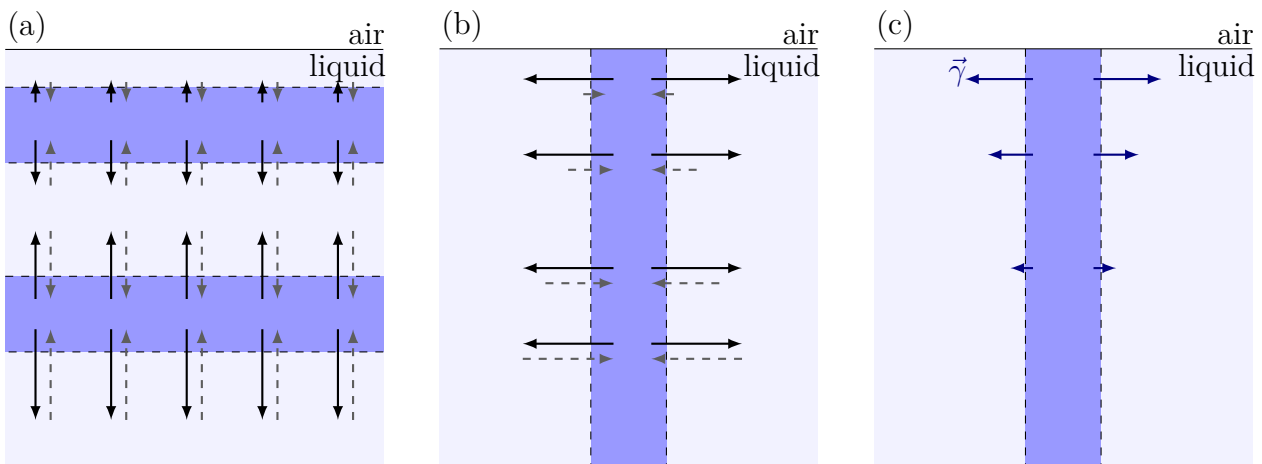
Fig. 1.4: Attractive (solid dark arrow) and repulsive (dashed gray arrows) forces exerted on different layers of fluid (darker blue areas) by the rest of the fluid. These sketches are inspired by those proposed by Marchand et al. [18] to explain the orientation of surface tension. (a) Forces exerted on horizontal layers of fluid. Since there is no up-down symmetry, attractive and repulsive forces have to balance in order to ensure the equilibrium of the fluid layer. Attractive forces are long range and increase with depth because the density increases. Therefore, repulsive forces have to increase with depth too. (b) Forces exerted on a vertical layer of fluid. The left-right symmetry ensures the equilibrium of the vertical layer. The repulsive forces are isotropic and decrease with depth as in (a) whereas the attractive forces are almost constant. (c) Near the interface, there is a net force on each side of the vertical layer. This force, which is the surface tension, is attractive and parallel to the interface.

1.2   Floatation of objects

Usually, to determine if an object could float, we consider the balance between weight W and buoyancy B. If the density of the object is lower than the density of the liquid, the object is supposed to float. Otherwise, it is supposed to sink. For large objects like boats, this is true because surface tension is negligible compared to the gravitational force. However, when the size of the object decreases, weight and buoyancy decrease much faster than surface tension because the first ones depend on the volume whereas the last one, being a force per unit of length, depends on the perimeter. Typically, surface tension becomes significant for centimetre or millimetre-sized objects.

When an object is placed at the surface of a liquid, it deforms the interface in its neighbourhood. In the case of a simple and heavy particle, the interface is bent downwards as shown in Figs. 1.5 (a) and (c). As the surface tension is parallel to the interface, the integration of surface tension along the contact line gives a net force, called the capillary force F_γ, which is vertical and upwards. In the case of a simple and light particle like a bubble trying to get out of the liquid, the interface is bent upwards and the integration of surface tension on the contact line gives a downwards capillary force as illustrated on Fig. 1.5 (b) and (d). These capillary forces can counterbalance the difference between weight and buoyancy to trap objects at the surface of the liquid.
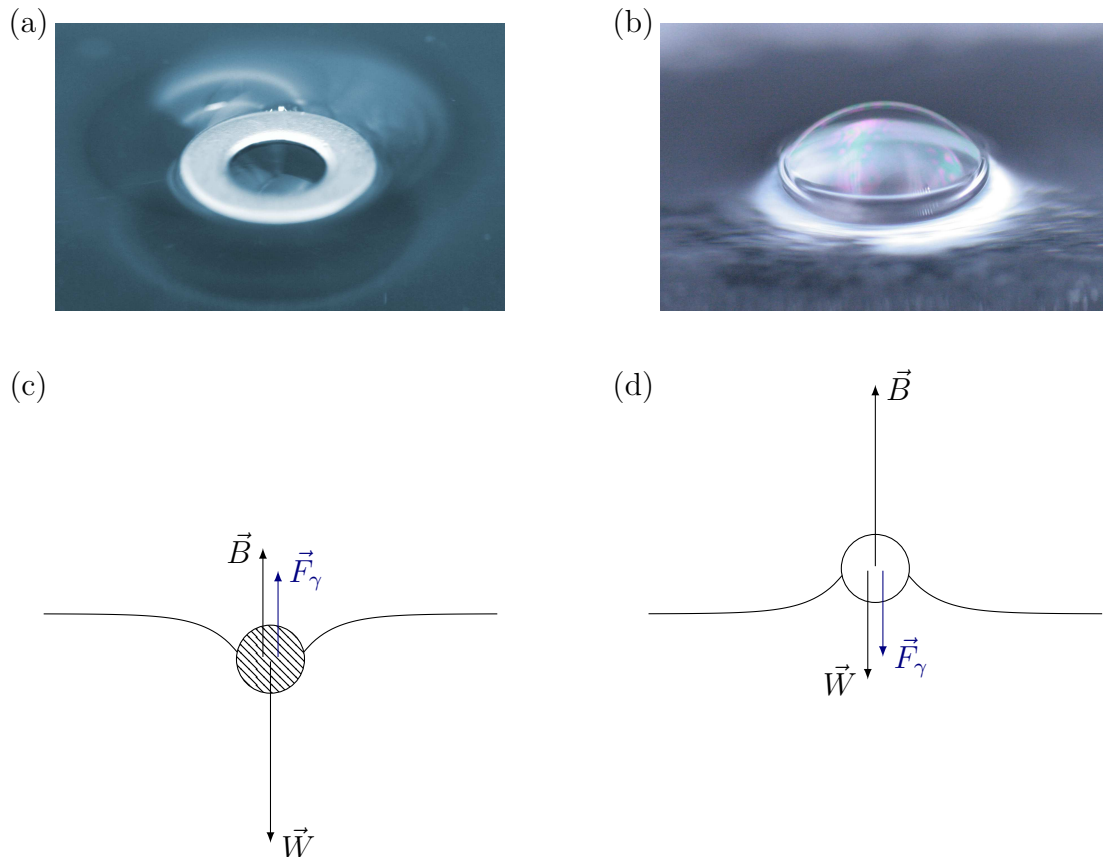
Fig. 1.5: Heavy and light objects trapped at an air/liquid interface. (a) Metallic ring of $6.8\,\mathrm{mm}$ diameter floating at the surface of water. (b) Millimetre-sized air bubble in a bath of soap water. (c) Forces on a simple heavy object trapped at an air/liquid interface. (d) Forces on a simple light object trapped at an air/liquid interface. When the density of the object is larger (lower) than the density of the liquid, the surface is deforms downwards (upwards). The integration of surface tension along the contact line results in a net force, the capillary force F_γ, that balances the difference between weight W and buoyancy B.

1.3 Laplace pressure

When the surface of a liquid is deformed and curved, there is a pressure jump across the interface. This pressure difference is caused by surface tension. Consider a small 1d portion dl of the interface as illustrated in Fig. 1.6. When it is flat, the surface tensions exerted on both sides of dl cancel exactly. On the contrary, when the interface is curved, only the x-projections of surface tension cancel. The addition of the y-projections results in a net force

that is directed towards the center of curvature of the interface. The pressure associated with this force is called the Laplace pressure.
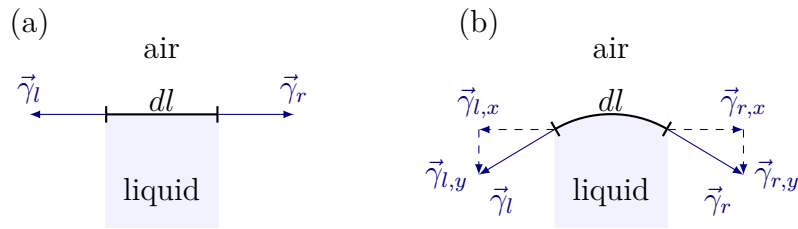
Fig. 1.6: Surface tension exerted on a small 1d portion dl of the interface. (a) When the interface is flat, surface tensions on both side of dl cancel and there is no net force. (b) When the interface is curved, only the x-components of surface tensions on both sides cancel. There is a net force that results from the addition of the y-components.

To determine the expression of the Laplace pressure, consider a droplet of radius r as illustrated in Fig. 1.7. Its equilibrium shape being a sphere, the pressure inside the drop have to be larger than the pressure outside because the center of curvature is inside the droplet. If we want to increase its radius by dr, it requires a work dW that can be expressed as

$$dW = -p_{\text{drop}}dV_{\text{drop}} - p_{\text{ext}}dV_{\text{ext}} + \gamma dS \tag{1.5}$$

where p_{drop} is the pressure inside the droplet, dV_{drop} is the volume change of the droplet, p_{ext} is the pressure in the external medium, dV_{ext} is the volume change of the external medium and dS is the surface change of the droplet [14]. As $dV_{\text{drop}} = 4\pi r^2 dr = -dV_{\text{ext}}$ and $dS = 8\pi rdr$, Eq. (1.5) becomes, at equilibrium ($dW = 0$)

$$0 = -p_{\text{drop}}4\pi r^2 dr - p_{\text{ext}}4\pi r^2 dr + \gamma 8\pi rdr \tag{1.6}$$

and the pressure jump is given by

$$p_{\text{drop}} - p_{\text{ext}} = \Delta p = \frac{2\gamma}{r} \tag{1.7}$$
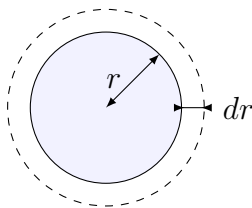
Fig. 1.7: A liquid droplet of radius r. The overpressure inside the droplet can be evaluated by computing the work required to increase its radius by dr.

A similar demonstration can be done to generalize the expression of the Laplace pressure Δp for an arbitrary interface that separates two fluids. This relation is called the Laplace's law [14]

$$\Delta p = \gamma \left(\frac{1}{R_1} + \frac{1}{R_2} \right) \tag{1.8}$$

where R_1 and R_2 are the main radii of curvature of the interface.

1.4 Capillary interaction between two spheres

When there are several particles that float at the interface, the deformation around each particle is no more symmetrical. The disturbance of the surface between them results from the combination of the deformations caused by each particle. The interaction between particles can be understood through energy considerations [20]. Consider a heavy sphere: as it is denser than the liquid it will tend to go downwards to decrease its energy. Being trapped at the interface, it can only move along the interface. When a second heavy sphere is placed at the interface, the first sphere sits in the deformation created by the second one. It simply moves down the meniscus, which brings it closer to the second heavy sphere as illustrated in Fig. 1.8 (a). When the second sphere is light and deforms the interface upwards, the heavy sphere still moves down the surface and, in this case, goes away from the light one as illustrated in Fig. 1.8 (b). Basically, particles that induce like meniscii attract and particles that induce unlike meniscii repel.
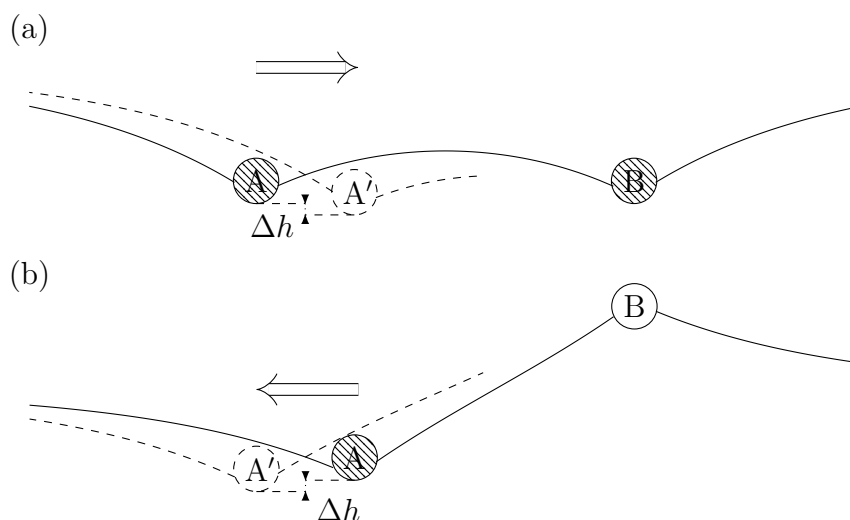
Fig. 1.8: Interactions between floating spheres. The heavy sphere A is denser than the liquid. To decrease its energy, it has to go downwards. As it is trapped, sphere A can only move along the interface. (a) Sphere A is next to a second heavy sphere, sphere B. The last bends the surface downwards. Sphere A is in the deformation created by sphere B and moves down the meniscus, which brings it closer to sphere B. (b) Sphere A is next to a light sphere, sphere B. The last bends the surface upwards. Sphere A is in the deformation created by sphere B and moves down the meniscus, which brings it away from sphere B.

The horizontal force between two floating particles can be computed with the Nicolson method [21]. It had been initially elaborated to explain the formation of bubbles raft at the surface of a liquid and was later used for floating particles [20, 22]. The Nicolson method is based on the superposition approximation: we suppose that the shape of the interface between particles is the sum of the profiles around each particle at infinite separation. This holds when the slopes are weak. Although this may seem to be a crude hypothesis in practice, the superposition approximation works well when the slopes of the interface are small, even at quite short separations between the particles [21, 22].

Within this approximation, consider two floating particles at finite distance. When particle A moves along the interface, it will moves along the deformation created by particle B. It is therefore submitted to changes in gravitational potential energy relative to infinite separation. Particle A should also experience changes in interfacial energies but these are of higher order and can be neglected if the capillarity dominates gravity [20, 22, 23]. The gravitational energy

change of particle A can be computed as the product of its net weight (the difference between weight and buoyancy) by the change of height of its mass center relative to its height at infinite separation.

The change in height of particle A at a distance x of particle B is simply given by the displacement of the interface $h_B(x)$ caused by particle B at this distance. At infinite separation, the net weight of the particle is in equilibrium with surface tension. When the interface is curved, the surface tension equilibrates no more its net weight W_{net} but $W_{\text{net}} \cos \theta$, where θ is the angle of the interface. However, if the slopes are weak, $\cos \theta \approx 1$ and this effect can be neglected. The net weight of particle A can therefore be computed as being its net weight at infinite separation. From this, we can evaluate the expression of the gravitational energy of particle A, which is the interaction energy between the particles, and then derive it to get the interaction force.

1.4.1   Profile of the interface around a sphere

The deformation of the interface around a floating object can be very challenging to compute and may require specialized numerical tools and softwares like Surface Evolver. Theoretical calculations can only be performed for simple floating objects [20, 22, 24, 25]. The shape of the interface can be obtained with the condition that the Laplace pressure is equal to the difference of hydrostatic pressure caused by the deformation of the interface [20, 21, 22], *i.e.*

$$\Delta p = \rho g h \tag{1.9}$$

where ρ is the density of the liquid, g is the gravitational acceleration and h is the vertical height of the interface. Far from the floating particle, the interface is supposed flat and $h = 0$.

By choosing a cartesian coordinates system (x_1, x_2) which is in the plane parallel to the principal sections of curvature of the liquid-air interface, the principal radii of curvature, r_1 and r_2 are given by

$$r_i = \frac{\left(1 + \left(\frac{\partial h}{\partial x_i}\right)^2\right)^{3/2}}{\frac{\partial^2 h}{\partial x_i^2}} \tag{1.10}$$

where $i = 1, 2$. If the deformation around the particle is small,

$$\frac{\partial h}{\partial x_i} \ll 1 \tag{1.11}$$

and Eq. (1.10) becomes

$$\frac{1}{r_i} = \frac{\partial^2 h}{\partial x_i^2} \tag{1.12}$$

The equilibrium of Laplace and hydrostatic pressures can then be simplified as

$$\gamma \nabla^2 h = \rho g h \tag{1.13}$$

and then rewritten as

$$\nabla^2 h = \frac{1}{\lambda^2} h \quad , \text{with } \lambda = \sqrt{\frac{\gamma}{\rho g}} \tag{1.14}$$

where λ is the capillary length, being the length scale over which the deformation of the interface decays to zero. In the case of pure water, $\lambda \approx 2.7 \, \text{mm}$.

If we consider the simple case of a spherical particle, the contact line is circular and the deformation profile around the particle only depends on r. Expressing the Laplacian operator

in polar coordinates (r, θ) centered on the particle and taking into account that there is no variation along θ, Eq. (1.14) becomes

$$\frac{d^2 h}{dr^2} + \frac{1}{r}\frac{dh}{dr} = \frac{1}{\lambda^2}h \tag{1.15}$$

This is a Bessel equation and it has a solution in terms of the modified Bessel function of the second kind of order 0 [26]. We have

$$h = QK_0(r/\lambda) \tag{1.16}$$

where Q is a constant called the capillary charge. This length can be expressed in terms of the slope of the interface at the contact line (see Fig. 1.9),

$$h'_c = \left.\frac{dh}{dr}\right|_{r=R_c} \tag{1.17}$$

where R_c is the radius of the contact line. Using Eq. (1.16), we get

$$h'_c = -\frac{Q}{\lambda}K_1(R_c/\lambda) \tag{1.18}$$

For small x, $K_1(x) \approx 1/x$ and Eq. (1.18) gives

$$Q = -R_c h'_c \tag{1.19}$$

The capillary charge can be seen as a characteristic depth and depends on the vertical force balance on the particle. When it is positive (negative), the particle deforms the interface upwards (downwards). It is a useful quantity to evaluate interactions between floating objects and we will show in the following of this chapter that these forces can be expressed in terms of capillary charges.
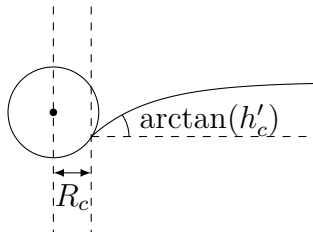
Fig. 1.9: Geometry of the interface around a heavy sphere. The contact line has a radius R_c and the angle of the slope of the interface at the contact line is $\arctan(h'_c)$.

1.4.2 Vertical force balance on a floating sphere

Consider a floating sphere on a flat interface. The deformation is symmetrical and the integration of surface tension around the contact line gives a net vertical force F_γ. The vertical force balance of this object consists in the sum of three forces: this capillary force F_γ, the weight W and the buoyancy B as illustrated in Fig. 1.10. The equilibrium of the sphere writes

$$\vec{F}_\gamma + \vec{W} + \vec{B} = 0 \tag{1.20}$$

Noting $\vec{W}_{\text{net}} = \vec{W} + \vec{B}$ the gravitational forces and projecting this equation on a vertical axis, we obtain

$$W_{\text{net}} = F_\gamma \tag{1.21}$$

As the contact line is a circle of radius r_c and as there is a cylindrical symmetry, the capillary force is given by

$$F_\gamma = 2\pi R_c \gamma_y, \quad \text{with} \quad \gamma_y = \gamma \sin\left[\arctan(h_c')\right] \tag{1.22}$$

where γ_y is the vertical component of surface tension at each point of the contact line. In the Nicolson method, the slopes are supposed weak, so $\sin\theta \approx \tan\theta$ and $\gamma_y \approx \gamma h_c' = -\gamma Q/R_c$. With these results and Eq. (1.21), the net weight of the spherical particle can be rewritten as

$$W_{\text{net}} = -2\pi\gamma Q \tag{1.23}$$

We thus obtain an expression of the net weight of the particle in terms of its capillary charge and surface tension. If the object is heavy (light), its capillary charge is negative (positive) and its net weight is positive (negative) as expected.
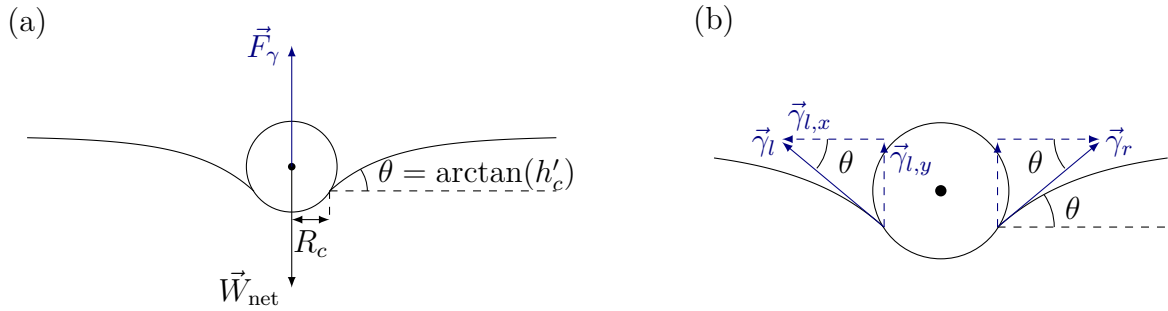
Fig. 1.10: Forces acting on a floating sphere. (a) The sphere is submitted to its net weight $\vec{W}_{\text{net}}$, which is the difference between its weight and buoyancy. As it deforms the interface with a cylindrical symmetry, the integration of surface tension along the contact line gives a net vertical force, the capillary force, that counterbalances the net weight. (b) Components of surface tension acting on the sphere. As there is a cylindrical symmetry, the x-components of surface tension around the contact line cancel and only the y-components contribute to the resultant capillary force F_γ.

1.4.3 Horizontal force between two spherical particles

Now that we have computed the interface profile around a spherical particle (Eq. (1.16)) and its net weight (Eq. (1.23)), we can evaluate the interaction force between two spheres of capillary charges Q_A and Q_B with the Nicolson method. The gravitational potential energy E (the interaction energy) of sphere A at the distance l of sphere B is

$$E(l) = W_{net,A} h_B(l) = -2\pi\gamma Q_A Q_B K_0(l/\lambda) \tag{1.24}$$

where the indices A and B refer to sphere A and sphere B. Then, the horizontal force between the particles can be computed from the energy by $F(l) = -dE/dl$. This gives

$$F(l) = -\frac{2\pi\gamma}{\lambda} Q_A Q_B K_1(l/\lambda) \tag{1.25}$$

As the electrostatic force, the capillary interaction between two floating spheres depends on the product of the capillary charges. However, the capillary force is attractive (repulsive) when the capillary charges have the same sign (opposite signs) and their range differs. Being proportional to $K_1(l/\lambda)$, capillary interactions are limited by λ and therefore short range whereas the electrostatics force, being proportional to $1/l^2$, is long range.

1.4.4 Limitations

All the mathematical developments done in this section rely on the main assumption that the deformation of the interface is small enough so that the slopes are weak. It will be the case if capillarity effects dominate gravity effects [23]. This competition can be evaluated by the Bond number Bo:

$$\text{Bo} = \frac{\rho g R^2}{\gamma} = \frac{R^2}{\lambda^2} \quad \left(= \frac{\text{gravity}}{\text{capillarity}} \right) \tag{1.26}$$

where R is the radius of the particle. If the Bond number is "small", slopes can be considered weak. Allain and Cloitre [23] perform numerical calculations of the full problem for the case of two horizontal cylinders. They show that pressure effects are mainly responsible for interaction force when Bo $\gg$ 1 and that the transition between both regimes occurs at $10 <$ Bo < 100. For a water-air interface, the capillary length λ is about $2.7\,\text{mm}$. Therefore, millimetre-sized objects are within the regime where capillary effects dominate (Bo $\leq$ 1) and the slopes are supposed weak.

1.5 Capillary multipoles

The previous section presents a simple explanation to the attraction between very basic objects. However, when the contact line around a particle is no more perfectly circular, upwards and downwards deformations alternate and the topography of the interface is much more complicated. This results in elaborated interactions between the objects. An undulated contact line can have different origins. It can come from the shape of the particle, the chemical properties or the roughness of the surface [27, 28]. For example, ellipsoidal particles create two downwards and two upwards lobes in the interface [29, 30], which looks like an electric quadrupole as illustrated on Fig. 1.11.
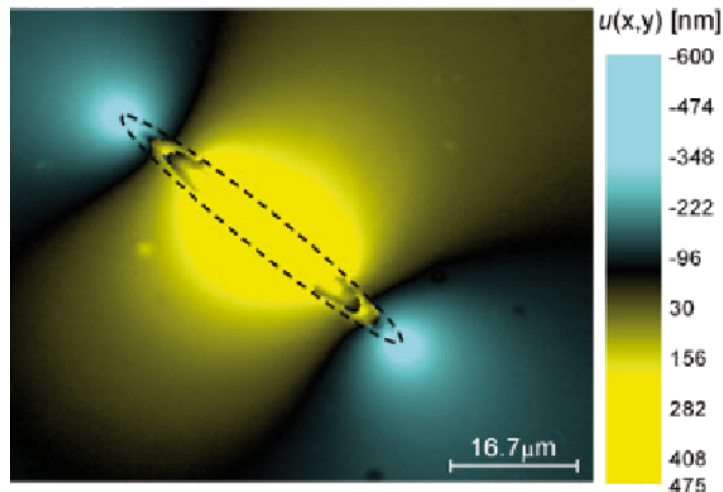
Fig. 1.11: Experimental profile of a small ellipsoidal particle floating at a water-air interface. The deformation of the surface induced by the object presents two upwards and two downwards lobes. This is similar to an electric quadrupole. The dashed line represents the boundaries of the particle while the colors indicate liquid elevation. Image from [31].

The evaluation of the interaction between complex particles reclaims a more complete and general approach. Indeed, an undulated contact line does not result (only) from the weight of the object but from its shape and its surface state. Moreover, if the particle is "too" small, typically micrometer or sub-micrometer size, its weight is too weak to deform the interface. In what follows, we consider the case of an undulated contact line whose vertical projection

is circular. First, we compute the topography of the interface and then, we show a general expression of the horizontal force between two particles. Finally, we derive this force for some particular cases.

1.5.1 Floating sphere with an undulated contact line

As we saw in Sec. 1.4.1, the profile of the interface can be computed from the equilibrium of Laplace and hydrostatic pressures. If the deformations around the particle are small, this equation can be linearised and expressed as Eq. (1.14). In the case of an undulated contact line, the profile of the interface in polar coordinates (r, θ) depends also on θ and the complete Laplacian has to be considered. Eq. (1.14) becomes

$$\frac{1}{r^2}\frac{\partial^2 h}{\partial \theta^2} + \frac{1}{r}\frac{\partial h}{\partial r} + \frac{\partial^2 h}{\partial r^2} = \frac{h}{\lambda^2} \tag{1.27}$$

The solution of this equation can be expressed as [27, 32, 33]

$$h(r, \theta) = \sum_{m=0}^{\infty} Q_m K_m(r/\lambda) \cos\left[m(\theta - \theta_m)\right] \tag{1.28}$$

where Q_m and θ_m are the capillary charge and the phase shift associated with mode m. Eq. (1.28) corresponds to a mutltipole expansion and, by analogy to electrostatic, an undulated contact line is called a capillary multipole.

1.5.2 General expression of the capillary interaction

We consider here the case of two spherical particles with an undulated contact line at a liquid-liquid interface. When such particles are in the neighbourhood of each other, the deformations induced by each sphere overlap and this results in an horizontal interaction force. This interaction force F on one particle comes from the capillary force and the hydrostatic pressure and can be expressed as [34]

$$F = (\vec{F}_\gamma + \vec{F}_p) \cdot \hat{e}_x \tag{1.29}$$

where $\vec{F}_\gamma = \int_L \vec{\gamma} dl$ is the integral of surface tension $\vec{\gamma}$ along the contact line L of the particle, $\vec{F}_p = -\iint_S p\vec{ds}$ is the integral of the hydrostatic pressure p through the surface S of the particle and $\hat{e}_x$ is the unit vector of an x axis parallel to the flat interface and passing through the vertical axes of both objects.

The general expression of this interaction force has been computed by Danov and Kralchevsky [33]. Consider a coordinate system (x, y) which lies in the plane formed by the flat surface. The x-axis passes through the vertical axes of both particles and the origin of the system is at mid-distance of the particles as illustrated in Fig. 1.12. Labelling A and B the left and right hand particles respectively, the force exerted on particle B by particle A can be expressed as [33]

$$F = -\gamma \int_{C_\delta} \vec{n}_\delta \cdot \mathbf{T} \cdot \hat{e}_x dl \tag{1.30}$$

where C_δ is a circle of radius R_δ centered on the considered particle (see Fig. 1.12), $\vec{n}_\delta$ is the outer unit normal of C_δ and $\mathbf{T}$ is the tensor of capillary interaction. Danov and Kralchevsky [33] define this tensor by

$$T_{ij} = \frac{\partial h_A}{\partial x_i}\frac{\partial h_B}{\partial x_j} + \frac{\partial h_A}{\partial x_j}\frac{\partial h_B}{\partial x_i} - \left(\frac{\partial h_A}{\partial x_n}\frac{\partial h_B}{\partial x_n} + \frac{h_A h_B}{\lambda^2}\right)\delta_{ij} \quad (i, j = 1, 2) \tag{1.31}$$

where δ_{ij} is the Kronecker symbol and the Einstein summation rule is used for the repeated index n.
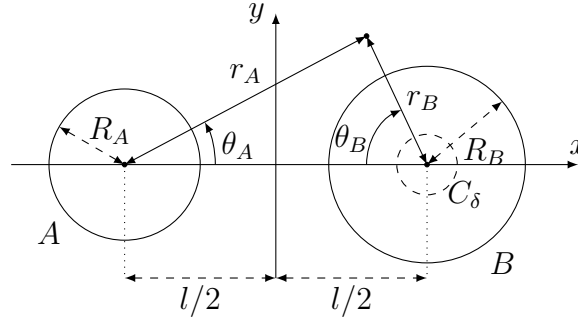
Fig. 1.12: Coordinates systems proposed by Danov and Kralchevsky [33]: cartesian coordinates (x, y) at mid distance between the particles and polar coordinates systems (r_A, θ_A) and (r_B, θ_B) centered on particles A and B respectively. The circles A and B are the projections of the contact lines of both particles. C_δ is the dashed circular contour used to derive the expression of the capillary force. It has a radius R_δ and an outer unit normal n_δ.

In the case of two spherical particles with an undulated contact line, we can use two polar coordinates (r_A, θ_A) and (r_B, θ_B), each one centered on a particle, as suggested by Danov and Kralchevsky [33] (see Fig. 1.12). These coordinates are linked with the cartesian system (x, y) by

$$x = -\frac{l}{2} + r_A \cos \theta_A \quad , \quad y = r_A \sin \theta_A \tag{1.32}$$

$$x = \frac{l}{2} - r_B \cos \theta_B \quad , \quad y = r_B \sin \theta_B \tag{1.33}$$

where l is the distance between the particles A and B. With these relations and Eq. (1.30), we can rewrite the force acting on particle B as

$$F = -\gamma R_\delta \int_0^{2\pi} \hat{e}_r \cdot \mathbf{T} \cdot \hat{e}_x d\theta_B \quad \text{at} \quad r_B = R_\delta \tag{1.34}$$

where $\hat{e}_r$ is a radial unit vector. From Eq. (1.33), we obtain

$$\frac{\partial h_Y}{\partial x} = -\frac{\partial h_Y}{\partial r_B} \cos \theta_B + \frac{\partial h_Y}{\partial \theta_B} \frac{\sin \theta_B}{r_B} \quad \text{with} \quad Y = A, B \tag{1.35}$$

Using this expression and the definition of the tensor T (Eq. (1.31)), taking into account that $\hat{e}_r \cdot \hat{e}_x = -\cos \theta_B$, the force on particle B given by Eq. (1.34) can be expressed as

$$
\begin{aligned}
F = &\gamma R_\delta \int_0^{2\pi} \left[\frac{\partial h_A}{\partial r_B} \frac{\partial h_B}{\partial r_B} \cos \theta_B - \left(\frac{\partial h_A}{\partial \theta_B} \frac{\partial h_B}{\partial r_B} + \frac{\partial h_A}{\partial r_B} \frac{\partial h_B}{\partial \theta_B} \right) \frac{\sin \theta_B}{R_\delta} \right. \\
&\left. - \left(\frac{1}{R_\delta^2} \frac{\partial h_A}{\partial \theta_B} \frac{\partial h_B}{\partial \theta_B} + \frac{h_A h_B}{\lambda^2} \right) \cos \theta_B \right] d\theta_B \quad \text{at} \quad r_B = R_\delta
\end{aligned}
\tag{1.36}
$$

As we know the profile of the interface around a sphere with an undulated contact line (Eq. (1.28)), we are now able to compute with Eq. (1.36) the force of interaction between capillary multipoles. The computations done by Danov and Kralchevsky [33] to obtain Eq. (1.30) imply that F must be independent of the radius R_δ of the contour δ used to derive the interaction force. Therefore, we can consider the special case $R_\delta \to 0$ as the multipole expansion defines the surface in the all xy-plane [33].

Interaction between monopoles

We first compute the horizontal force on the sphere B if both particles are capillary monopoles. In this case, only the term $m = 0$ is considered in the multipole expansion (Eq. (1.28)) and the deformations caused by each particle in isolation is

$$h_Y = Q_Y K_0(r_Y/\lambda) \quad \text{with} \quad Y = A, B \tag{1.37}$$

In the coordinate system (r_B, θ_B) the deformation caused by particle B depends only on r_B. Therefore, the derivatives $\partial h_b/\partial \theta_B$ cancel in Eq. (1.36) and the force reduces to

$$F = \gamma R_\delta \int_0^{2\pi} \left[\left(\frac{\partial h_A}{\partial r_B} \cos \theta_B - \frac{\partial h_A}{\partial \theta_B} \frac{\sin \theta_B}{r_\delta} \right) \frac{\partial h_B}{\partial r_B} - \frac{h_A h_B}{\lambda^2} \cos \theta_B \right] d\theta_B \quad \text{at} \quad \text{r}_\text{B} = \text{R}_\delta \to 0 \tag{1.38}$$

With Eq. (1.35), this becomes

$$F = \gamma R_\delta \int_0^{2\pi} \left[-\frac{\partial h_A}{\partial x} \frac{\partial h_B}{\partial r_B} - \frac{h_A h_B}{\lambda^2} \cos \theta_B \right] d\theta_B \quad \text{at} \quad \text{r}_\text{B} = \text{R}_\delta \to 0 \tag{1.39}$$

If $R_\delta \to 0$, $r_A \to L$ and h_A is independent of θ_B. The force simplifies as

$$F = -2\pi \gamma R_\delta \left(\frac{\partial h_A}{\partial x} \frac{\partial h_B}{\partial r_B} \right) \quad \text{at} \quad \text{r}_\text{B} = \text{R}_\delta \to 0 \tag{1.40}$$

In this expression, the first derivative can be computed as

$$\frac{\partial h_A}{\partial x} = \frac{\partial h_A}{\partial r_A} \frac{\partial r_A}{\partial x} + \frac{\partial h_A}{\partial \theta_A} \frac{\partial \theta_A}{\partial x} \quad , \tag{1.41}$$

and the last one is

$$\frac{\partial h_B}{\partial r_B} \bigg|_{r_B = R_\delta \to 0} = -\frac{Q_B}{\lambda} K_1(\frac{r_B}{\lambda}) \bigg|_{r_B = R_\delta \to 0} = -\frac{Q_B}{r_B} \tag{1.42}$$

since $\dfrac{dK_0(x)}{dx} = -K_1(x)$ and $K_1(x) \approx \dfrac{1}{x}$ for $x \to 0$ [26].

The deformation caused by particle A has a cylindrical symmetry, so $\dfrac{\partial h_A}{\partial \theta_A} = 0$. From Eq. (1.32), we have

$$r_A = \sqrt{\left(\frac{l}{2} + x \right)^2 + y^2} \tag{1.43}$$

and

$$\frac{\partial r_A}{\partial x} = \frac{l/2 + x}{r_A} \tag{1.44}$$

For $r_\delta \to 0$, $x \to l/2$ and $r_A \to l$. We obtain

$$\frac{\partial r_A}{\partial x} \bigg|_{R_\delta \to 0} = 1 \tag{1.45}$$

and the derivative gives

$$\frac{\partial h_A}{\partial x} \bigg|_{R_\delta \to 0} = -\frac{Q_A}{\lambda} K_1 \left(\frac{l}{\lambda} \right) \tag{1.46}$$

Substituting Eqs. (1.42) and (1.46) in Eq. (1.40), we find that the interaction force is given by

$$F(l) = -\frac{2\pi}{\gamma} Q_A Q_B K_1(l/\lambda) \tag{1.47}$$

30

Since $K_1(x) = K_{-1}(x)$ [26], this equation can also be written as

$$F(l) = -\frac{\pi}{\gamma} Q_A Q_B \left[K_1(l/\lambda) + K_{-1}(l/\lambda) \right] \qquad (1.48)$$

With this general approach, we recover the same result than the Nicolson approach presented in Sec. 1.4 (see Eq. (1.25)).

Interaction between a monopole and a multipole

Now, we compute the interaction force when A is a multipole of order m and B is a monopole. The interfacial profiles around the particles in isolation are

$$h_A(r_A, \theta_A) = Q_{A,m} K_m(r_A/\lambda) \cos\left[m(\theta_A - \theta_{A,m}) \right] \quad \text{and} \quad h_B(r_B) = Q_B K_0(r_B/\lambda) \qquad (1.49)$$

As in the previous case, the force on particle B is given by Eq. (1.40). To compute the derivative $\partial h_A/\partial x$ (Eq. (1.41)), we need to evaluate $\partial \theta_A/\partial x$. From Eq. (1.32), we have

$$\theta_A = \arctan\left(\frac{y}{l/2 + x} \right) \qquad (1.50)$$

Derivating this expression, we obtain

$$\frac{\partial \theta_A}{\partial x} = -\frac{y}{(l/2 + x)^2 + y^2} \qquad (1.51)$$

When $R_\delta \to 0$, $y \to 0$ and

$$\left. \frac{\partial \theta_A}{\partial x} \right|_{R_\delta \to 0} = 0 \qquad (1.52)$$

With Eqs. (1.52) and (1.45), the derivative of Eq. (1.41) becomes

$$\left. \frac{\partial h_A}{\partial x} \right|_{R_\delta \to 0} = -\frac{Q_{A,m} Q_B}{2\lambda} \left[K_{m+1}(l/\lambda) + K_{m-1}(l/\lambda) \right] \cos(m\theta_{A,m}) \qquad (1.53)$$

where we used that $\theta_A \to 0$ when $R_\delta \to 0$ and the relation [35]

$$\frac{dK_m(x)}{dx} = -\frac{1}{2} \left[K_{m+1}(x) + K_{m-1}(x) \right] \qquad (1.54)$$

Finally, with Eqs. (1.40) and (1.53), the interaction force between a monopole and a multipole separated by a distance l is given by

$$F(l) = -\frac{\pi \gamma Q_{A,m} Q_B}{\lambda} \left[K_{m+1}(l/\lambda) + K_{m-1}(l/\lambda) \right] \cos(m\theta_{A,m}) \qquad (1.55)$$

This expression has a form similar to the interaction of monopoles (Eq. (1.48)).

Interaction between multipoles

Finally, we consider the interaction between two multipoles, one of order m (A) and one of order n (B). The interfacial profiles around the particles in isolation become

$$\begin{aligned} h_A(r_A, \theta_A) &= Q_{A,m} K_m(r_A/\lambda) \cos\left[m(\theta_A - \theta_{A,m}) \right] \quad \text{and} \\ h_B(r_B, \theta_B) &= Q_{B,n} K_n(r_B/\lambda) \cos\left[n(\theta_B - \theta_{B,n}) \right] \end{aligned} \qquad (1.56)$$

In this case, h_B depends on θ_B and Eq. (1.36) can not be simplified. The calculations are much more complex than the previous cases. From Eq. (1.36), Danov and Kralchevsky [33] performed a complete computation of the interaction force between capillary multipoles and showed that it is given by

$$F(l) = -\frac{\pi\gamma Q_{A,m}Q_{B,n}}{\lambda} \left[K_{m+n+1}\left(\frac{l}{\lambda}\right)\cos(m\theta_{A,m} - n\theta_{B,n}) + K_{m-n-1}\left(\frac{l}{\lambda}\right)\cos(m\theta_{A,m} - n\theta_{B,n}) \right]$$
(1.57)

Despite the complex deformation of the interface caused by spheres with an undulated contact line, this expression has a simple form that depends on the product of the capillary charges of the multipoles, their order and their orientation. Taking m and n equal to 0, we find immediately the monopole-monopole interaction computed previously.

1.6 Self-assembly of floating objects

In the last few years, self-assembly is become a topic of great interest among the scientific community, especially at the mesoscopic scale [10, 11, 12, 13]. Capillary interactions are significant for millimeter and submillimeter floating objects and can be used to assemble them into particular structures (capillary-driven self-assemblies) [36, 37, 38]. The goal of this thesis being to manipulate and assemble floating particles through capillary interactions, capillary-driven self-assemblies are our starting point. Hereafter, we first describe how simple floating objects self-assemble into arrays. Then, we show how the geometry or the properties of the particles can be changed to create more complex structures.

1.6.1 Self-assembly of spherical objects

One of the most basic capillary-driven self-assembly is the aggregation of bubbles into a bubble raft [21, 39, 40]. This is something we can observe in a kitchen if some bubbles are produced in milk or coffee. As seen in Sec. 1.4, a bubble creates a simple positive capillary charge. When several bubbles float at the surface of a liquid, they attract each other and form a raft [39]. When they all have approximatively the same size, they form a regular hexagonal lattice as illustrated in Fig 1.13. Such bubble rafts were used as model of crystal structures [39, 40]. An interesting and simple mechanism to explained the formation of these rafts was proposed by Nicolson [21]. He elaborated an approximate method now known as the "Nicolson method" and derived an analytic expression of the capillary force. Similar compact aggregates can be obtained with other objects whose contact line is circular, as spherical beads or disks. Similarly to bubbles, these entities will behave like monopolar capillary charges.
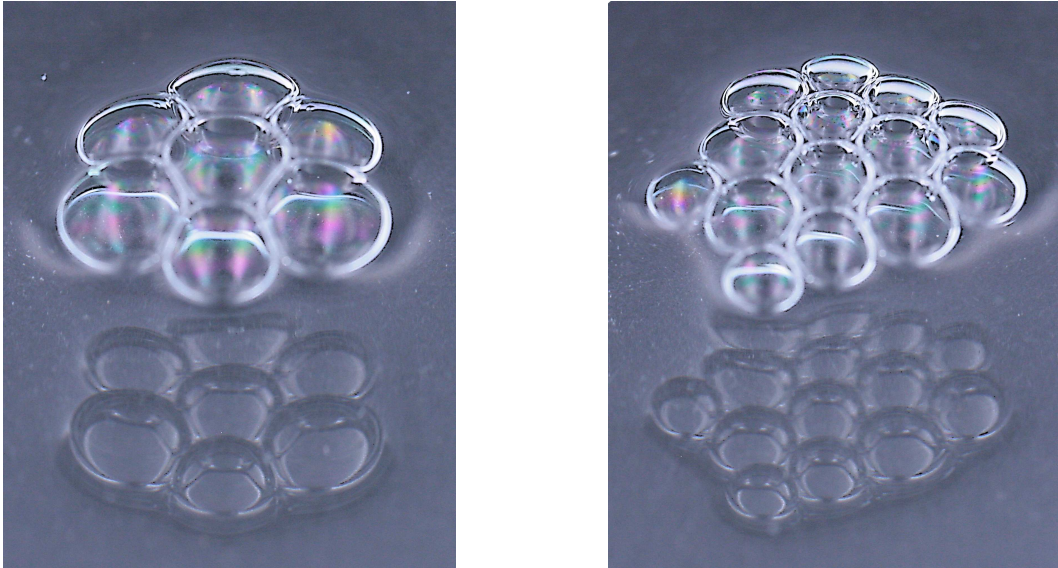
Fig. 1.13: Examples of assemblies of bubbles on soap water. Bubbles deform a liquid interface upwards, creating positive capillary monopoles. Theses monopoles attract each other to form bubble rafts.

1.6.2 Self-assembly of complex objects

When the contact line is not circular, a multipolar capillary charge is created at the interface. Objects with relatively simple shapes may exhibit elaborated interactions and assemble into sophisticated structures. For example, an ellipsoid floating with its long axis parallel to the surface induces downwards menisci at its tips and upwards menisci along its long axis [41]. This deformation is similar to a quadrupolar capillary charge. In nature, mosquito eggs are a good example of mesoscopic ellipsoidal particles. Unlike bubbles, these eggs do not form a compact aggregate but self-assemble into an open and anisotropic structure containing chains [31]. They aggregate with side-to-side or tip-to-tip contacts but not with tip-to-side contacts. That is a behaviour expected for capillary quadrupoles. Indeed, tip-to-side contact would result from the interaction of opposite charges and opposite capillary charges repel. Ellipsoids are the basic anisotropic particles. Their capillary interactions are widely studied, both theoretically and numerically as well as experimentally [29, 42, 43, 44].

Along with the shape, the orientation of the floating object is an important parameter as it modifies the contact line. Indeed, if the long axis of an ellipsoid is perpendicular to the interface, the contact line is circular and it induces a capillary monopole. The interactions will be different and the resulting assemblies will therefore have different structures. As another example, Daniello et al. [45] have study the influence of the orientation of floating cubes on the final assembly. They found that a regular square lattice is obtained when the cubes float with a face up whereas a complex raft with different configurations is formed when the cubes float vertex up.

To control the interactions between floating particles and the structure of their assembly, we need to tune the capillary charges, the deformation of the interface that an object creates. The shape and the orientation of the particle can be designed to induce specific capillary charges. However, a custom capillary charge will often require very complex shape and the orientation of floatation results from a tight equilibrium. Moreover, there is no direct and easy relationship between the shape of an object and the deformation of the interface. As we saw in Sec. 1.4, the Laplace equation, that gives the profile of the interface, can only be analytically solved for basic floating objects like spheres or cylinders [20, 22, 24, 25]. And yet, some approximations have to be made.

Another way to control the deformation around an object is to tune the hydrophilic/hydrophobic character of its edges [46, 47, 48]. This technique allows to accurately choose the positions of positive and negative charges along the particle without to design complex shapes and to compute the interface profile with specialized tools. Wolfe et al. [48] built millimetresized hexagonal plates of polydimethylsiloxane and functionalized their faces to be hydrophobic or hydrophilic. These plates are placed at a perfluorodecalin-water interface and interact through capillary interactions. The resulting self-assembly depends on the configuration of hydrophobic and hydrophilic faces and on the density of the aqueous phase [48]. It ranges from close pack structures to chains and disorder structures. Some of them are shown in Fig. 1.14. Tuning the wettability of the faces of objects also allows shape recognition [49, 50]. For example, Choi et al. [49] performed recognition and assembly of millimeter-sized polydimethylsiloxane objects floating at a perfluorodecalin-water interface. Their particles have complementary shapes and the capillary interactions are controlled by the configuration of hydrophobic and hydrophilic sides. Fig. 1.15 shows some structures obtained by Choi et al. [49].
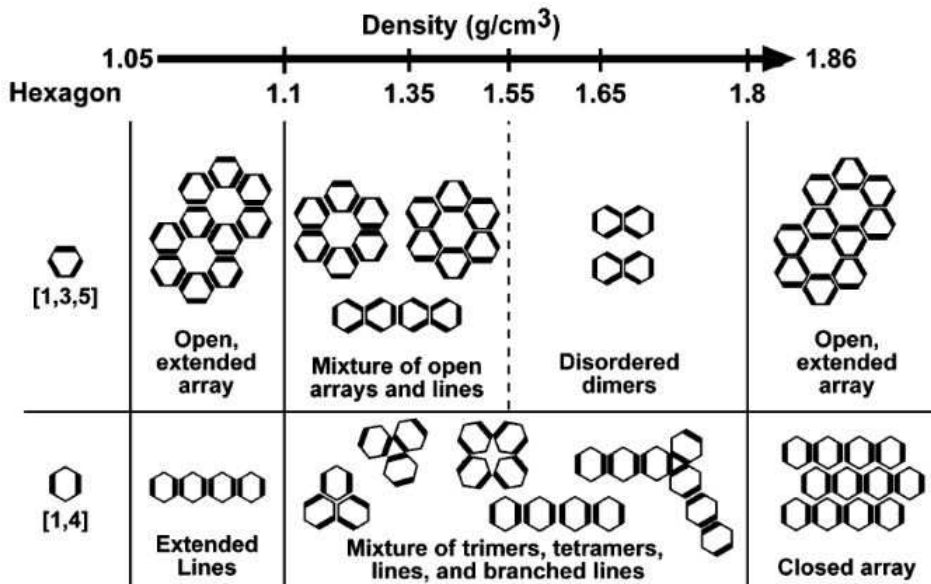
Fig. 1.14: Examples of assemblies obtained by Wolfe et al. [48] for millimetre-sized hexagonal plates of polydimethylsiloxane with different configurations of hydrophilic and hydrophobic edges. These hexagons float at a water-perfluorodecalin interface and aqueous phase of different densities are used. The thick lines represent the hydrophobic edges and the thin lines the hydrophilic edges. Image from [48].

Changing the wettabily of the edges of a particle is an efficient technique but it required specific material treatments and can be a complex task. Moreover, it obviously alters the surface of the object and that can be a problem in some applications. An alternative method is to bend the particle to induce local curvature of the interface [51, 52, 53]. Simple cross-shaped entities that can be easily produced by a low cost 3D-printer were proposed by Poty et al. [51]. The branches are bend to create capillary charges at their tip as illustrated in Fig. 1.16 (a). Their length, their number and their curvature can be adjusted to create specific capillary multipoles and control the structure of the assembly [51]. A particle with four branches of equal length, and whose successive branches are bent with opposite curvatures, creates a capillary quadrupole as shown in Fig. 1.16 (c). When such particles are placed at an air-water interface, tips of the same sign attract and the resulting assembly is a square lattice (Fig. 1.16 (b)). Starting from these four-branch objects, other structures can be easily obtained with small changes in their geometry. For example, by elongating the branches in

one direction so that the branch length ratio is $\sqrt{3}$, Poty et al. [51] obtained triangular lattices as illustrated in Fig. 1.17.
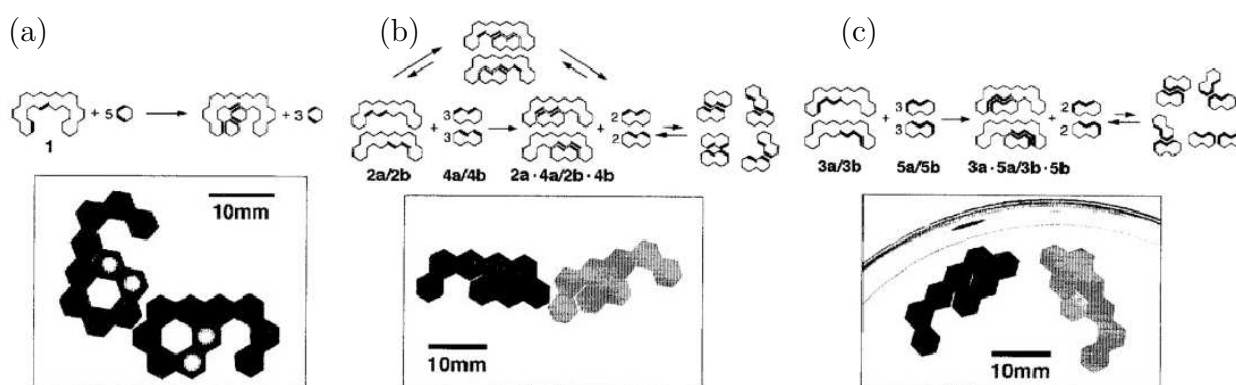
Fig. 1.15: Assembly with shape-recognition of particles composed of polydimethylsiloxane hexagons [49]. The objects are placed at the interface of perfluorodecalin and water and swirled at a low frequency. Edges represented by thick lines are hydrophobic and the ones represented by thin lines are hydrophilic. (a) A receptor assembles with two single hexagons. The agitation frequency is set to break up aggregates of single hexagons which are less stable. (b) and (c) Assemblies of chiral particles. Two receptors (2a and 2b or 3a and 3b) recognize and bound the right dimer. The agitation frequency is adjust to break unwanted and less stable arrays. Image from [49].
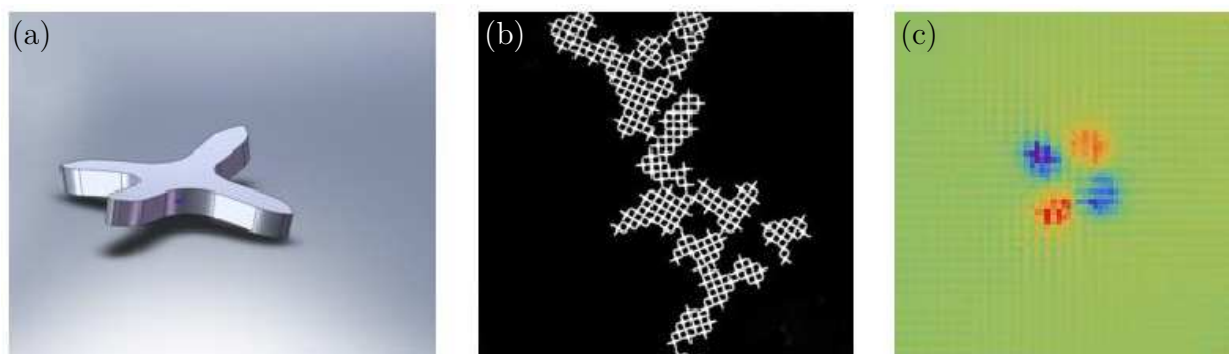
Fig. 1.16: Floating entities proposed by Poty et al. [51]. (a) Symmetric cross-shaped object. Successive branches are bent with opposite curvatures. The size of the object is 15 mm. (b) Self-assembly obtained with these particles. A square lattice is spontaneously formed. (c) Interfacial deformation around the object. A quadrupole is observed. Image from [51].
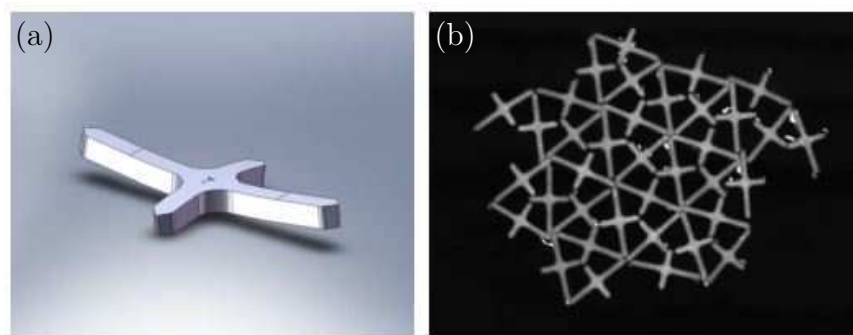
Fig. 1.17: (a) Asymmetric cross-shaped object with elongated branches in one direction. The branch length ratio is $\sqrt{3}$. Successive branches are bent with opposite curvatures. (b) Self-assembly obtained with these particles. A triangular lattice is formed. Image from [51].

Additional forces, such as magnetic or electric forces, can be combined with capillary interactions to obtain more sophisticated assemblies or to control the aggregation of the floating particles [54, 55, 56, 57]. Combining two competitive forces, as a capillary attraction and a magnetic repulsion, allows to set equilibrium distances between particles [58, 59]. Many works have been done with spherical particles to obtain crystal-like structures as the following examples. Wen et al. [60] realised planar colloidal crystals of various lattices with coated magnetic microspheres floating at a surface of glycerine and placed in an external magnetic field. Vandewalle et al. [61] studied large assemblies of soft ferromagnetic beads at an air-water interface. Subsequent works of this last group show also that lots of structures can be created with such beads by controlling the orientation of the magnetic field and that magnetocapillary assemblies can swim when submitted to varying magnetic fields [62, 63]. Some examples are shown on Fig. 1.18.
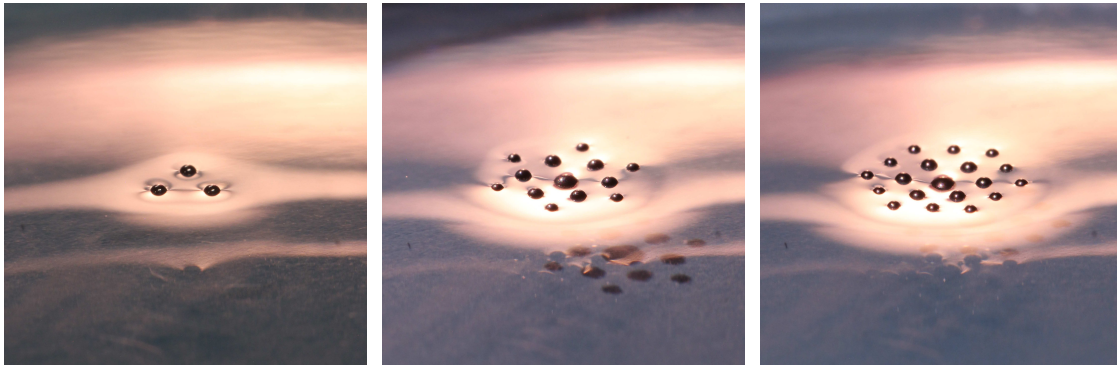
Fig. 1.18: Examples of magnetocapillary self-assemblies made of soft ferromagnetic beads. The diameters of the particles are 400 μm, 500 μm and 800 μm. Image from [64].

1.7 Summary

In this chapter, we presented phenomena specific to interfaces, described through surface tension. Despite its microscopic origin, surface tension affects the macroscopic world and numerous manifestations can be seen in our everyday life. This tension corresponds to a force per unit length and is the key ingredient of this thesis. Floating objects deform a liquid interface and are submitted to a capillary force that comes from surface tension. We saw that this force allows heavy objects to float and traps bubbles at the interface. Moreover, when multiple particles are at the surface of a liquid, the deformations of the surface overlap and capillary forces lead to short range interactions between the particles.

Capillary interactions have been studied in the literature [20, 21, 22, 32, 33, 34] and we presented a general expression to compute them. We started by showing that the deformation of the interface caused by a particle can be described with a multipolar expansion and that a floating particle can therefore be considered as a capillary multipole, by analogy to electrostatic. Then, we explained how the capillary force between two particles can be computed and expressed in a relative simple form that depends on the product of the capillary charges of the multipoles, their order and their orientation.

Capillary interactions can be used to self-assemble floating objects into various structures. We explained how aggregates can be formed with simple particles and presented strategies to build complex floating objects. In particular, we showed how a particle can be bent to induce specific deformations and specific capillary multipoles. Such complex particles allow to build elaborated structures.

In this thesis, our goal is to assemble and manipulate particles by deforming the liquid surface, exploiting the capillary interactions that these deformations will induce. This requires that we design components with specific shapes or properties to obtain the right interactions. The concept of capillary multipole will help us to design and model these components.

From this chapter, we can see that the floating mesoscopic particles that have been built so far can be divided in two groups as illustrated in Tab. 1.1: basic components (monopolar deformation) that form compact aggregates and complex components (multipolar deformation) that form elaborated open or closed structures. However, they all are passive. They are not able to change their interactions and can only aggregate into static self-assemblies. This thesis brings two main contributions to the state of art. In our first strategy, we develop active components whose interactions are controllable. These components will contribute to the elaboration of devices that will be able to change their function or behaviour. In our second strategy, we build local actuators and we show how they can be used as tweezers to manipulate floating particles. This is a new technique that allows to handle any type of floating particles, solid components as well as drops or bubbles.

Type of components	Resulting assembly	Examples of components
monopole	compact aggregate	bubbles [39, 40]
		spheres
		disks
multipole	various open and closed structures	ellipsoids [31]
		hexagons with hydrophilic/phobic faces [46, 47, 48]
		bent cross-shaped objects [51]

Tab. 1.1: Floating components can be divided into two groups: monopoles and multipoles. Monopoles self-assemble into compact aggregates. Multipolar particles self-assemble into elaborated open and closed structures.

2 Imaging a fluid-fluid interface

In order to assemble and manipulate floating mesoscopic components, we want to deform a liquid surface. As explained in Chap. 1, such deformations will induce capillary forces that can be used to move simple particles or to create specific interactions between floating components. Therefore, as deforming the surface is the key ingredient of this work, a direct and reliable method to measure the topography of fluid-fluid interface is required.

Among the different techniques that already exist, optical methods are well adapted because they are non intrusive and can perform two-dimensional measurements. Indeed, it is essential that the liquid surface is not disturbed by the imaging technique. Optical methods can be divided into two categories: reflective and refractive techniques. The main reflective methods are Moiré and fringes projections techniques [65, 66, 67] and the main refractive methods are interferometry [68, 69], shadowgraphy and Schlieren methods [70, 71, 72, 73]. In this work, water is used because it has a high surface tension, it is easily available and non toxic. The surface to image is transparent and we choose to consider only refractive-index visualization techniques. Reflective methods could also be used but it requires the addition of a liquid dye as a titanium dioxide pigment paste [74, 75].

Refractive techniques have been widely used for decades [69, 70, 73]. However, they usually require a complex optical system because collimated light is used. With the development of digital cameras and the quick advances in computing power, a new Schlieren method, the Background Oriented Schlieren (BOS) technique emerged in the 2000's [76, 77, 78, 79, 80, 81]. The principle of BOS methods is quite simple. A camera takes two pictures of a patterned background. The first picture is an undistorted image of the background (the picture of the background through a flat interface in the case of a fluid-fluid interface). The second picture is the distorted image of the background through the refractive object to image (the picture of the background through the deformed interface in the case of a fluid-fluid interface). These two images are then compared with a cross correlation software.

BOS technique has some advantages over other refractive methods [72, 82]. Because it uses non-collimated light, it only requires a basic optical system and simplifies greatly the recording. It also allows for very large fields of view, which is not the case with traditional Schlieren methods and interferometry. Moreover, BOS technique has been improved these last years and applied successfully to various problems, especially in the case of Faraday waves [83, 84], wave-droplets interactions [85, 86] and already floating objects [51, 87]. For all these reasons, the BOS technique have been chosen in this work to measure the topography of the liquid interface.

This chapter describes the BOS technique and some of its implementations that have been used in this thesis in order to measure the deformation of the liquid surface caused by floating objects or local actuators. We first present more in details the BOS method. Then, we focus on two specific implementations developed to observe the free surface of a liquid, the Free-

Surface Synthetic Schlieren method and the Fast Checkerboard Demodulation method, which offer interesting features. Next, we emphasize the limitations of both methods. After that, we present a new method that we developed in the lab in order to overcome some limitations of the previous techniques. This new method uses an enhanced optical setup that simplifies computations and avoids approximations. Finally, we show how we implemented and validated it.

2.1 Background Oriented Schlieren technique

Schlieren methods have been used for years to observe phenomena in transparent media. The first form of Schlieren imaging dates back to the 17th century and was performed by Robert Hook [70, 73]. However, it is only in the second half of the 19th century, with the works of August Toepler and Léon Foucault, that Schlieren technique has started to be developed and used in laboratories [70, 72]. Now, it has become a classical tool in various fields as shock waves [71, 88, 89, 90] or air flows [82, 91] for example.

Schlieren methods rely on a simple principle: the refraction of light in an inhomogeneous media. The inhomogeneities create local changes in the refraction index and light is deviated according to the Snell-Descartes law. This results in a "Schlieren" image containing light-and-dark patterns that are directly related to the first spatial derivative of the refractive index [92]. The optical system required is quite complex [72]. In its basic form, a non coherent "white" light is collimated by a first lens, passes through the inhomogeneous media and is then focused by a second lens. A filter, often just a razor blade, is placed at the focal point to selectively filter out refracted light rays [71]. A camera captures the light rays beyond the filter.

The alternatives to classical Schlieren techniques are shadowgraphy and laser interferometry. Shadowgraphy is close to Schlieren technique but simpler: the image is the shadow, cast on a distant screen, of the refraction of a light source by the inhomogeneous transparent media. However, in practice, shadowgraphy usually provides qualitative information [93]. Moreover, Schlieren technique is generally more sensitive, especially for weak disturbances [70]. Laser interferometry is known to offer quantitative information but its optical system is at least as complex as classical Schlieren methods. In addition, with the progress performed these last years, Schlieren techniques are now able to compete with its quantitative power [72].

The most remarkable recent development in Schlieren technique is undoubtedly Background Oriented Schlieren, also called synthetic Schlieren. This method was proposed almost simultaneously by Dalziel et al. [76] and Meier [77] and received lots of attention. The optical setup of BOS technique, illustrated on Fig. 2.1, is really simple. A camera records images of a patterned background through the inhomogeneous medium. The changes in refractive index caused by the homogeneities result in shifts of the structures of the background image. This distorted image is then compared to a non distorted reference image of the background, usually background through fluid at rest, by digital image analysis. Such a digital processing replaces parts of the usual optics and has become possible thanks to the rise of computers and the revolution of digital camera.

The main advantage of BOS technique is obviously its ease of use. Quantitative measurements can be obtained with a low cost optical setup and digital analysis can be performed with robust algorithms. Moreover, as non-collimated light is used, the BOS field of view can be very large. The basic setup of BOS brings some disadvantages too. Its main drawback is the limitation of the resolution by the statistical displacement computation [82]. Depending on the depth of view of the camera, it could also be difficult to achieve sharp focus on both targeted medium and background. Finally, BOS is sensible to vibrations of the setup that could happen between the captures of reference and distorted images.
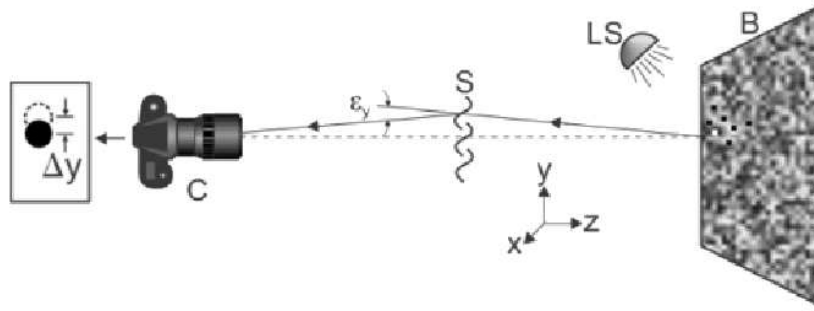
Fig. 2.1: Optical setup of the BOS technique. A camera (C) takes pictures of a patterned background (B) through an inhomogeneous (or Schlieren) medium (S). The background is illuminated by a white light source (LS). Light rays are refracted because of the change in refractive index in the inhomogeneous medium and the structures of the background appear shifted. Image from [72].

Over the years, numerous papers have been written on BOS, to analyse its performances or to improve its accuracy. The technique has been adapted to various applications [82]. For example, natural backgrounds have been used with BOS to perform large-scale outdoor experiments [90, 91] and 3D density fields have been observed with BOS by combining images from multiple cameras with tomographic reconstruction [94, 95].

In the context of this thesis, the most interesting application of BOS is the observation of the free surface of liquids. In 2009, based on the work of Kurata et al. [96] and Elwell [97], Moisy et al. [98] characterized an application of the BOS technique to measure the topography of the free surface of a fluid. They called it the Free-Surface Synthetic Schlieren (FS-SS) method. With this approach, a liquid surface can be imaged and reconstructed with the simple optical setup of BOS and the robustness of cross-correlation algorithms. The FS-SS method has been successfully used to measure the deformations of a liquid surface caused by Faraday waves [83, 84], bouncing droplets [85, 86] and floating objects [51].

2.2 Free-Surface Synthetic Schlieren method

Being a BOS technique, the FS-SS method only requires a simple setup. A random points pattern, the background, is placed below (above) a transparent container filled with a transparent liquid and a camera, from above (below), takes pictures of the refracted pattern through the liquid as illustrated on Fig. 2.2. Despite its simplicity, this method allows to accurately measure the topography of an interface. Moisy et al. [98] reported a precision of $1\,\mu$m for a view field of $10\,$cm. The reconstruction of the surface consists in three steps:

1. Computation of the displacement field between pictures of the disturbed and undisturbed surface.

2. Computation of the surface gradient from the displacement field.

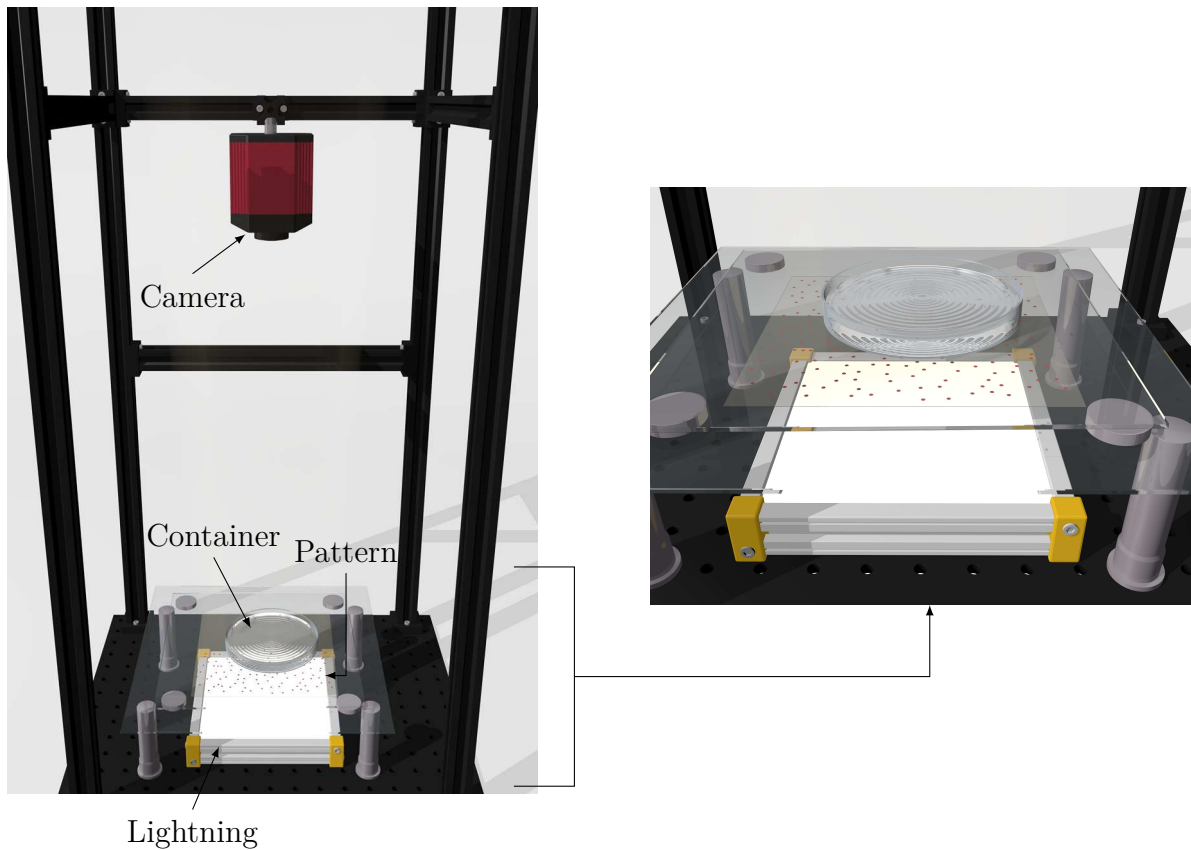3. Integration of the surface gradient.

Fig. 2.2: Illustration of a FS-SS experimental setup. A light source illuminates from below a random points pattern. Above it, a container filled with a transparent liquid is placed on a glass plate. A camera takes pictures of the surface of the liquid from above.

Computation of the displacement field

When the light ray coming from a point P of the pattern reaches the camera, it is refracted by each interface and its image P' appears displaced. If the liquid surface is disturbed, it causes an additional displacement of the image P' as shown on Fig. 2.3. The displacement field caused by the deformation of the interface is computed by comparing pictures of the disturbed and undisturbed surfaces with a Digital Image Correlation (DIC) algorithm.

Computation of the surface gradient

In the FS-SS method, Moisy et al. [98] established a relationship between the displacement field and the surface gradient by analysing the geometry of the light rays. As illustrated on Fig. 2.3, this geometry is quite complex. The incidence plane, which is defined as the plane CPP' containing the camera C, the point P and its image P', is inclined and does not contain the optical axis. Therefore, the displacement PP' does not take place along the radial direction with respect to the optical axis but in a direction $\hat{s}$, which corresponds to the intersection of the horizontal plane and the incidence plane CPP'. Because of that, Moisy et al. [98] used three approximations to compute the surface gradient from the displacement field. These approximations limit the method to weak slopes, weak deformations and weak paraxial angles, and are the following:

(i) *Paraxial approximation.* To be satisfied, the distance between the pattern and the camera must be much larger than the distance h_p between the pattern and the interface.

(ii) *Weak slope.* This implies that the surface slope θ and the incident angle i are weak ($\sin(i) \approx \tan(i) \approx i$ and $\cos(i) \approx 1$). So, only first order terms in i and θ are considered in the computations.

(iii) *Weak amplitude.* This implies that the local height of the liquid h_l is supposed to be equal to the mean height of the undisturbed surface h_0.

Considering theses approximations, it can be shown that the gradient field can be computed from the displacement field with a linear relationship [98]

$$\vec{\nabla}h = -\frac{\delta\vec{r}}{h^*}, \quad \text{with} \quad \frac{1}{h^*} = \frac{1}{\alpha h_s} - \frac{1}{H} \tag{2.1}$$

where $\alpha = 1 - \dfrac{n_a}{n_l}$, $h_s = h_0 + h_c\dfrac{n_l}{n_c} + h_a\dfrac{n_l}{n_a}$ is an effective distance between the pattern and the surface of the liquid and H is the distance from the camera to the pattern.
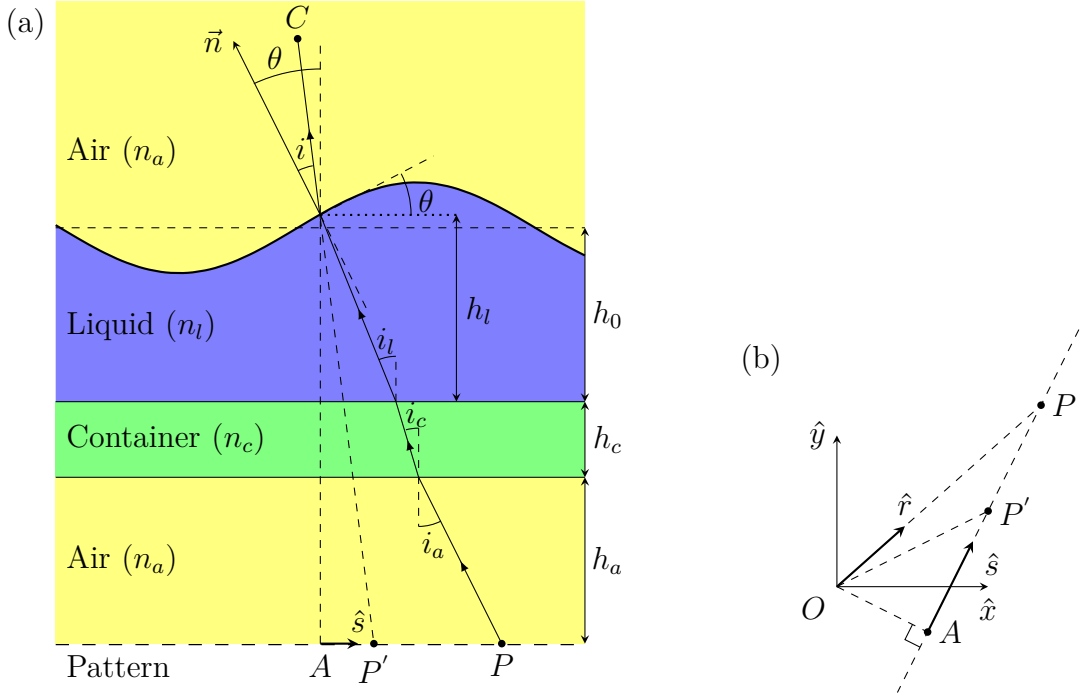
Fig. 2.3: In the original FS-SS method, an inclined optical ray coming from the pattern point P appears to come from the image P'. The incidence plane CPP' does not contain the optical axis and is inclined. (a) Inclined incidence plane CPP'. (b) Positions of the point P and its image P' on the xy plane (pattern plane). The direction $\hat{s}$ corresponds to the intersection of the xy plane and the incidence plane.

Integration of the surface gradient

Finally, the surface gradient is integrated to reconstruct the interface. This is done with a least-square algorithm.

2.3 Fast Checkerboard Demodulation method

Various improvements and alternatives have been proposed to the original FS-SS method [99, 100, 101, 102]. Among them, Wildeman [100] developed the Fast Checkerboard Demodulation (FCD) method. This technique is particularly interesting because it keeps the basic optical setup of the FS-SS method and enhances the digital computation of the displacement field (step 1). Instead of a DIC algorithm with a random points pattern, it uses a Fourier analysis with a 2D checkered pattern. The geometrical computations and approximations are the same than the FS-SS method.

2.3.1 Computation of the displacement field

A 2D periodic pattern image I_0 can be expressed as

$$I_0(\vec{r}) = \sum_{m=-\infty}^{\infty} \sum_{n=-\infty}^{\infty} a_{mn} e^{i(m\vec{k_1}+n\vec{k_2})\cdot\vec{r}} \tag{2.2}$$

where $\vec{r}$ is the position (x, y) of the pixel of the image, a_{mn} is the Fourier coefficient, $\vec{k_1}$ and $\vec{k_2}$ are the wavenumber vectors of the pattern I_0. In the Fourier space, the periodic pattern behaves like a carrier, as in frequency modulation of airwaves. The peaks k_c of this carrier are given by $\vec{k_c} \in m\vec{k1} + n\vec{k2}$. When the periodic pattern is seen through a disturbed interface, a deformation signal $\vec{\delta r}$ modulates the phase of the carrier peaks and the distorted pattern image I can be expressed as

$$I(\vec{r}) = \sum_{m=-\infty}^{\infty} \sum_{n=-\infty}^{\infty} a_{mn} e^{i(m\vec{k_1}+n\vec{k_2})\cdot(\vec{r}-\vec{\delta r})} \tag{2.3}$$

From pictures of the undisturbed (flat) and disturbed interfaces, $g_0(\vec{r})$ and $g(\vec{r})$, the carrier and deformation signals, can be respectively extracted with usual Fourier filtering techniques:

$$\begin{aligned} g_0(\vec{r}) &= a_c e^{(i\vec{k_c}\cdot\vec{r})} \\ g(\vec{r}) &= a_c e^{(i\vec{k_c}\cdot(\vec{r}-\vec{\delta r}))} \end{aligned} \tag{2.4}$$

Then, the phase field is easily computed by

$$\phi(\vec{r}) = \Im(\ln(gg_0^*)) = -\vec{k_c} \cdot \vec{\delta r} \tag{2.5}$$

Performing these computations for two linearly independent carrier peaks gives a system that can be solved for $\vec{\delta r}$.

2.3.2 Benefits of the FCD

DIC algorithms are well known and intensively used in lots of applications like Particle Image Velocimetry [103, 104, 105]. However, they have some drawbacks [106, 107]. The main one is that the displacement is implicitly supposed constant at the window scale, which limits the resolution. DIC algorithms are also slow and prevent real-time imaging [72]. To increase the resolution, we can use algorithms based on recursive methods with multi-scale windows [108, 109] but these are complex and extremely time consuming.

Keeping a basic optical setup, the FCD improves greatly the resolution and the computation speed. With its image analysis based on Fast Fourier Transform, the displacement field is computed at each pixel of the image instead on interrogation windows. The FCD processing is also much faster and allows real-time imaging. Moreover, being a global method, it is also more robust to noise and masked areas.

2.4 Limitations of FS-SS and FCD methods

The computation of the displacement field between pictures of the undisturbed and disturbed interfaces is the first step to reconstruct an accurate surface. As we have just seen, the FCD method offers some interesting benefits compared to the FS-SS method. However, to reconstruct the topography of the surface from the displacement field, the FCD method shares the same geometrical approximations than the FS-SS method. Because of these approximations, even if the displacement field is perfectly known, both methods suffer from the following main limitations [98]:

1. As the interface is reconstructed by integrating the surface gradient, uniform changes in the interface height are not detected.

2. For strong curvatures or large surface-pattern distances, caustics appear and it is no longer possible to compute properly the displacement field.

3. Slight vibrations of the setup can add noise components to the displacement field.

4. Since calculations are linearized, the method is limited to weak deformations, weak slopes and weak paraxial angles.

The two first limitations are intrinsic to BOS technique and the third one can be prevented with a stable optical setup. The last and most restrictive one is mainly caused by the geometrical approximations used to rely the displacement field to the surface gradient. In the calculations, only first order terms are considered and the local liquid depth of the deformed interface is supposed equal to the liquid depth of the undisturbed interface. Moreover, errors on the measurement of the liquid depth can impact drastically the surface gradient estimation.

2.5 Double Pattern Synthetic Schlieren method

When a mesoscopic object floats at the surface of water, the deformations around it are usually small and the FCD method should give accurate measurements. However, if local actuators are used to shape the liquid interface, the deformations can become much larger. In order to be able to accurately measure such moderate or large deformations/slopes, we developed a new BOS method, the Double Pattern Synthetic Schlieren (DP-SS) method, that relies on an improved optical setup. Moreover, this new method does not depend on the liquid depth and can be used in various applications in which the liquid depth varies or is difficult to measure like spreading drops. However, rays crossings and caustics still prevent proper measurements of strong curvatures.

Thanks to its enhanced optical setup, the DP-SS method improves the computation of the surface gradient from the displacement field (step 2). The others steps are not updated. The displacement field can be computed by a DIC algorithm or by the FCD method. In the following, let us consider a step-by-step description of additional improvements leading to the DP-SS method.

2.5.1 Bitelecentric objective

The approximations used in both FS-SS and FCD methods come from the complexity of the geometry of the light rays. To simplify it, a first step is to modify the optical setup by placing a bitelecentric objective with a high aperture on the camera. With this objective, only vertical rays (rays parallel to the optical axis) coming from the pattern reach the camera. This allows

to avoid parallax effects and to greatly simplify the optical ray tracing and calculations, at the price of a more elaborated setup.

As only vertical rays reach the camera, the incident plan, defined as the plane containing the camera C, the point P and its image P', contains the optical axis and is vertical (Fig. 2.4). Therefore, the gradient is equal to the slope of the curve in the direction $\hat{r}$ and we get the following relationship

$$\vec{\nabla} h = \tan(i)\hat{r} \tag{2.6}$$

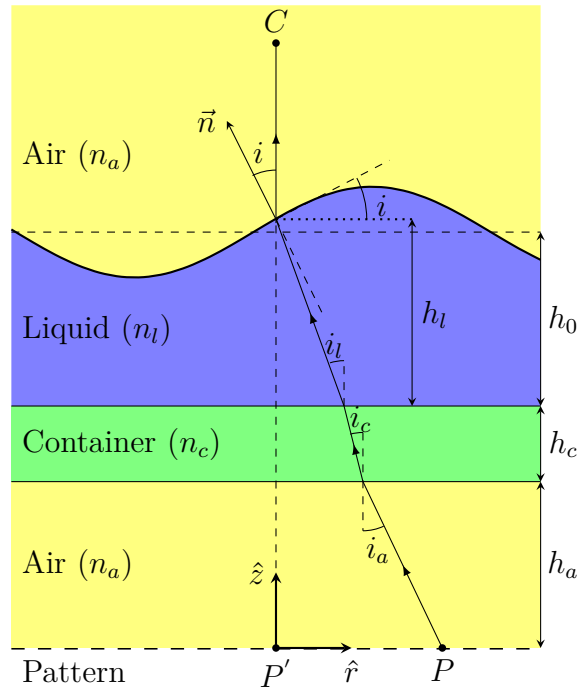between the gradient field and the incident angle i without any approximation.

Fig. 2.4: Incidence plane obtained with a bitelecentric objective. As only vertical refracted rays reach the camera, the image P' of point P is located at the intersection of the optical axis and the pattern. Therefore, the incidence plane CPP' is vertical.

2.5.2 Double pattern

In order to avoid geometrical approximations, a second step is the use of a double pattern. Each component of this double pattern is placed at a specific height, as illustrated in Fig. 2.5. The distance h_p between both patterns can be fixed and accurately known. In this setup, the camera has to take four images instead of two: (i) pattern 1 through the undisturbed interface, (ii) pattern 2 through the undisturbed interface, (iii) pattern 1 through the disturbed interface and (iv) pattern 2 through the disturbed interface.

By comparing both images of pattern 1, the displacement PP' between a point P of the pattern 1 and its image P' trough the deformed surface can be computed by a DIC algorithm or by Fourier demodulation (if a checkered pattern is used). The displacement QQ' between a point Q of the pattern 2 and its image Q' through the deformed surface can be computed exactly the same way. The distance h_p between the patterns being known, the angle i_a can be computed from these two displacements by

$$i_a = \arctan\left(\frac{\delta r}{h_p}\right) \tag{2.7}$$

where $\vec{\delta r} = \vec{PP'} - \vec{QQ'}$. Applying the Snell-Descartes law at each interface, we get the following system of equations

$$\begin{cases} n_a \sin(i) = n_l sin(i - i_l) \\ n_l \sin(i_l) = n_c \sin(i_c) \\ n_c \sin(i_c) = n_a \sin(i_a) \end{cases} \quad (2.8)$$

By solving this system, we obtain a relationship between the incidence angle i and the angle i_a:

$$i_a = \arcsin \left\{ \frac{n_l}{n_a} \sin \left[i - \arcsin \left(\frac{n_a}{n_l} \sin(i) \right) \right] \right\} \quad (2.9)$$

This relationship cannot be inverted but, numerically, we can use i_a obtained from Eq. (2.7) to interpolate the function and evaluate i. Once we get the incidence angle i, the gradient can be computed with Eq. (2.6). However, this gives only the magnitude of the gradient. Its orientation ϕ can be determined from the components of the displacement field by

$$\phi = \arctan \left(\frac{\delta r_y}{\delta r_x} \right) \quad (2.10)$$

Knowing the magnitude and the orientation of the gradient, we can compute its x and y components and integrate them to reconstruct the surface slope.
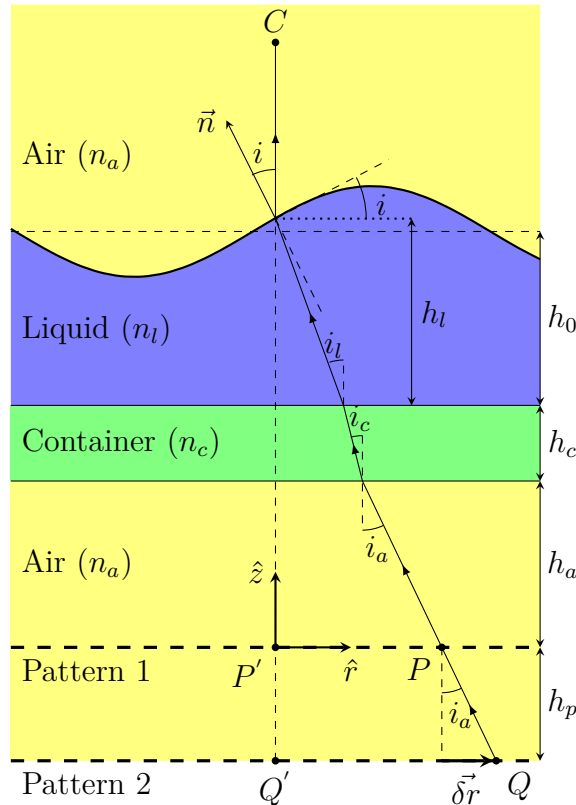
Fig. 2.5: The geometry of optical rays when a second pattern at a different height under the container is used. A second displacement QQ' can be computed. Knowing the difference of height h_p between the patterns, the angle i_a can be computed from δr, the difference of both displacements PP' and QQ'. A relationship can be established between i_a and the incidence angle i by applying the Snell-Descartes law at each interface. This relationship does not depend on the liquid height.

2.5.3   Benefits of the DP-SS method

The bitelecentric objective simplifies greatly the geometry of the light rays and the double pattern allows to avoid geometrical approximations. Moreover, computations become independent of the liquid depth. The only height implied in the calculations is the distance between the patterns. All the intermediate layers between the top screen and the interface, as the container wall, do not appear in Eq. (2.9). With these improvements, the method is no more limited to weak deformations and moderate to large deformations can be measured accurately. The DP-SS method could also be used in new applications in which the depth of the undisturbed liquid is not constant.

2.5.4   Drawback of the DP-SS method

The addition of a bitelecentric objective is necessary to simplify the geometry of the light rays but is also probably the main drawback of the DP-SS method. This makes the optics more difficult to implement but it still avoids some components of classical Sclieren technique. The bitelecentric objective also limits the field of view, which is not a problem is this work because we consider mesoscopic components.

   With its double pattern, the DP-SS method is more time consuming as four images have to be captured and two displacement fields have to be computed. Having to take pictures of two patterns could also prevent to image deformations that are not perfectly static. However, this can be solved by using patterns of different colors as explained in Sec. 2.6.1.

   Being a BOS technique, the DP-SS method is still limited to moderate slopes. Indeed, (very) strong slopes cause ray crossings, resulting in multiple images of the same point and preventing to compute the displacement field.

2.6   Implementation of the DP-SS method

The DP-SS method was implemented in the lab, tested and compared to the FS-SS and FCD methods. In what follows, we present our experimental setup and two typical applications in order to validate and emphasize its advantages.

2.6.1   Setup and computations

The double pattern is composed of two color patterns, one red and one blue, which are generated numerically with the Matlab scripts written by Wildeman [110] and made available on GitHub. These patterns are printed on 4 mm thick glass plates and are placed at different heights. The vertical distance between both patterns is fixed by spacers of accurate height. The setup is illustrated on Fig. 2.6. The blue pattern is on the bottom face of the top (blue edge) glass plate and the red pattern is on the top face of the bottom (red edge) glass plate in order to only have an air layer between them. Above the double pattern, a transparent container is placed on a glass plate. A 2448×2048 color camera equipped with a bitelecentric objective with a 118.06 mm $\times$ 98.47 mm field of view is suspended above the container.

   Pictures of the patterns are taken through the undisturbed and the disturbed surfaces of the transparent medium placed in the container. The R and B channels are extracted from these color images and binarized by thresholding in order to separate each pattern. The blue pattern appears dark on the R channel while the red pattern appears dark on the B channel.

   The angle i_a is computed from the displacement fields of both patterns with Eq. (2.7). From Eq. (2.9), a cubic spline interpolation is used to get the angle i from i_a. Then, the surface gradient is directly obtained from Eq. (2.6) and integrated to get the height of the

interface. The calculations of the displacement fields and the integration of the surface gradient are performed with the Matlab script written by Wildeman [110].
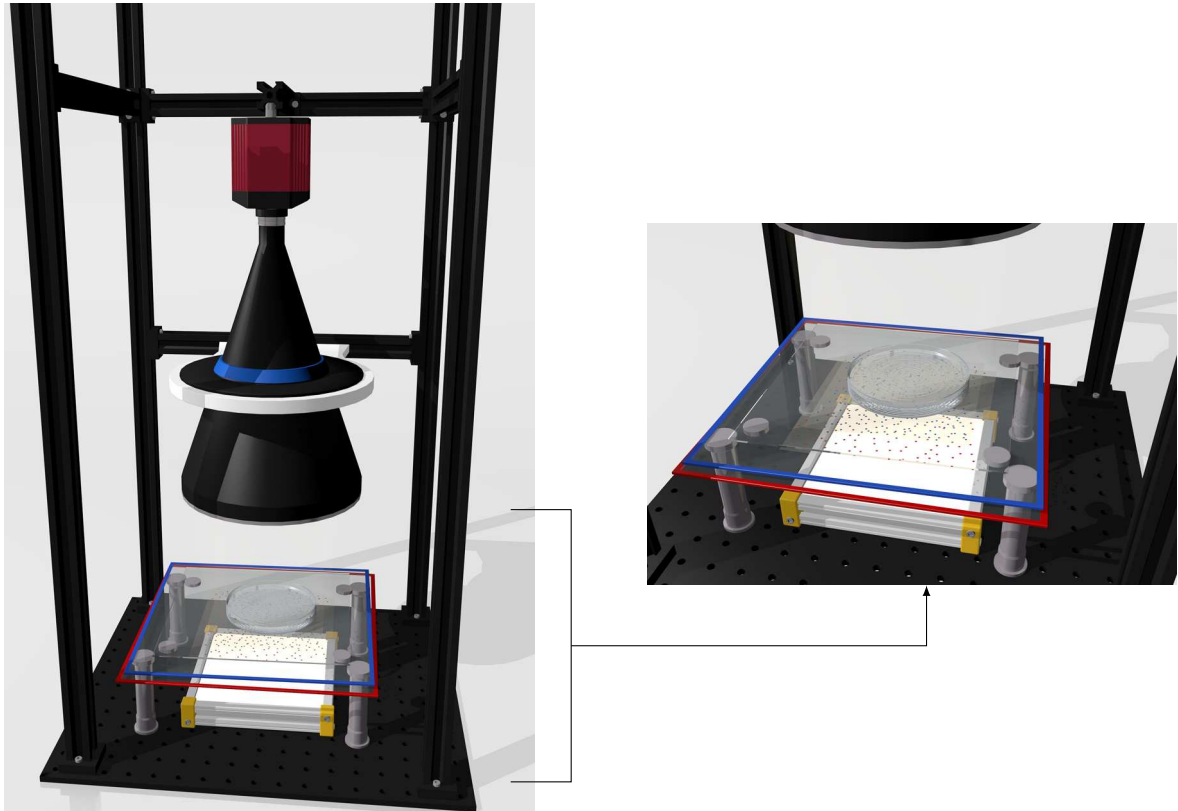

Fig. 2.6: Illustration of the proposed experimental setup. A camera with a bitelecentric objective is placed above a container and a double pattern. Each pattern is printed on a glass plate and placed at a specific height below the container. The blue one is on the bottom face of the blue edge glass plate and the red one is on the top face of the red edge glass plate. As there is only an air layer of constant thickness between the patterns, the surface gradient can be computed from Eqs. (2.6)-(2.9) and then integrated.

Depending on the application, the measurements of the topography of the transparent interface are done with either random points patterns (in Sec. 2.6.2) or checkerboards (in Sec. 2.6.3). Images of theses patterns, as taken by the color camera, are shown on Fig. 2.7. The random points double pattern is used with a DIC algorithm. The size of the dots is 0.2 mm, which corresponds to a size of about 4 pixels on the camera. This is a little bit larger than the optimal size of 2-3 pixels [111] but it is easier to separate the color dots when they are larger. To fulfil the criterion of approximately 5 dots per interrogation windows, considering a minimal window of 16x16 pixels, the density of points is set to 0.26. The double checkerboard is used with the FCD algorithm. The size of the squares is set to 0.5 mm long.
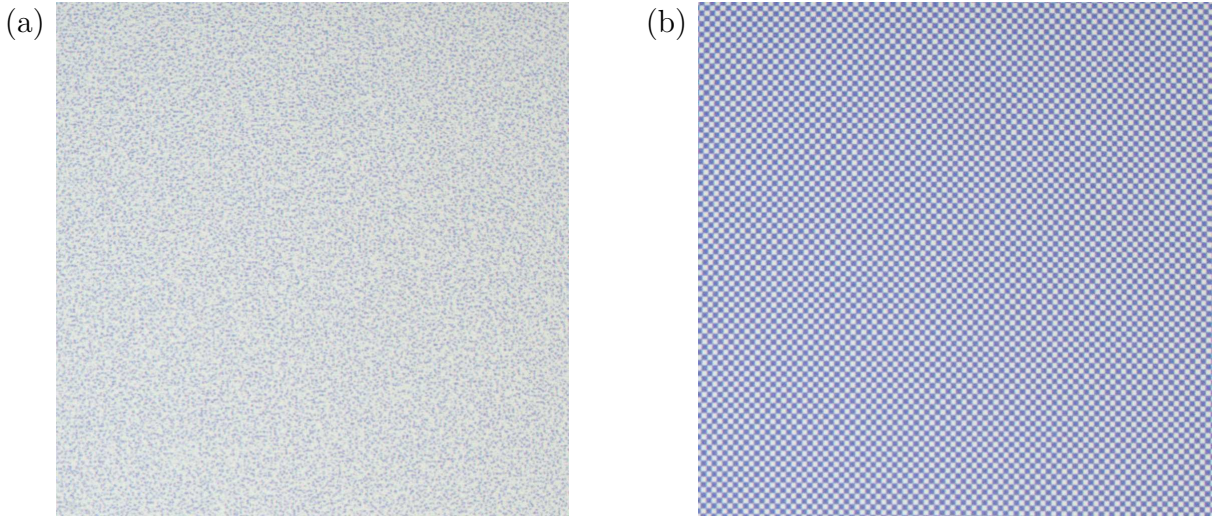
Fig. 2.7: Images of the blue patterns used to compute the displacement fields. These images are taken by the camera with a region of interest of 1024 x 1024 pixels. (a) Blue random points pattern used with a DIC algorithm. The size of the dots is 0.2 mm and the density is 0.26. (b) Blue checkerboard used with the FCD algorithm. The side of the squares is 0.5 mm long.

2.6.2 Slope measurements

In order to validate our improvements, the DP-SS method was used to image the surface of glass wedges with specific angles and the measured slopes were compared to the true wedge angles. These glass wedges are circular and have a diameter of 25.4 mm. Their angle ranges from 2° to 25°. In order to avoid errors caused by the sharp borders of the wedges, pictures taken by the camera are cut and the measurements are only done on square windows inscribed in the circular wedges. As all the points of the deformed image are displaced, random points patterns are used and the displacement fields are computed by the DIC algorithm written by Wildeman [110]. The FCD method is not adapted in this case because the displacement of all points can be bigger than the checkerboard wavelength. For each wedge, five measurements are done with random orientations. The mean angles measured for the different wedges are shown on Fig. 2.8. We can see that the DP-SS method performs better than the FS-SS method when the slope increases. Indeed, we measured angles up to 25° with an excellent accuracy whereas the FS-SS method becomes inaccurate for the largest angles. This is because Moisy et al. [98] consider only first order terms in computations.

The other main limitation of the FS-SS method is the weak amplitude approximation, which is masked when only the mean angle of a wedge is considered. Because of this approximation, the FS-SS method underestimates (overestimates) the slope when the local height is lower (greater) than the mean height. By computing the mean angle on a symmetric area around the center of the wedge, underestimations and overestimations cancel. To illustrate the limitation of the weak amplitude approximation, the local measured angle of a 18.15° degrees wedge with both methods is shown on Figs. 2.9 and 2.10. The orientation of the wedge is -36.13° degrees from the x axis. Although the mean value of the slope is close to the true one (as it can be seen on Fig. 2.8), Figs. 2.9 and 2.10 show that the FS-SS method fails to recover the correct angle along the wedge. The value is overestimated or underestimated, except at the center. With the DP-SS method, a constant angle is obtained as expected.
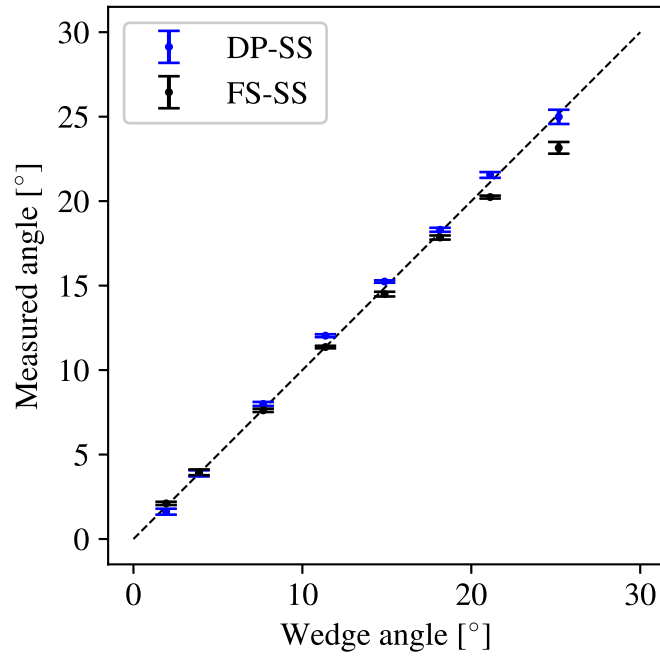
Fig. 2.8: Mean angle of wedges measured by the DP-SS and FS-SS methods as a function of the true angle value. Slopes up to 25° have been measured with an excellent accuracy by the DP-SS method whereas the FS-SS method becomes worse when the angle increases. The displacement fields are computed by the DIC algorithm written by Wildeman [110].

Fig. 2.9: Local measured angle of a 18.15° wedge. The orientation of the wedge is -36.13° from the x axis. (a) FS-SS method. (b) DP-SS method. The displacement fields are computed by the DIC algorithm written by Wildeman [110].

Fig. 2.10: Profile of the measured angle along the wedge orientation. The slope of the wedge is 18.15° and its orientation is -36.13° from the x axis. The abscissa r is the distance from the center. The displacement fields are computed by the DIC algorithm written by Wildeman [110].
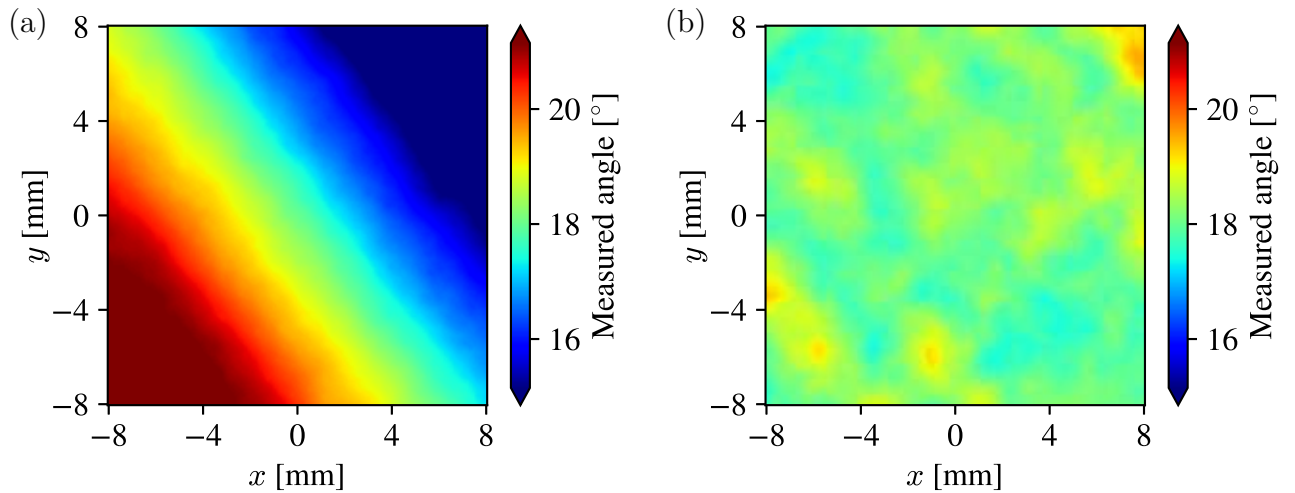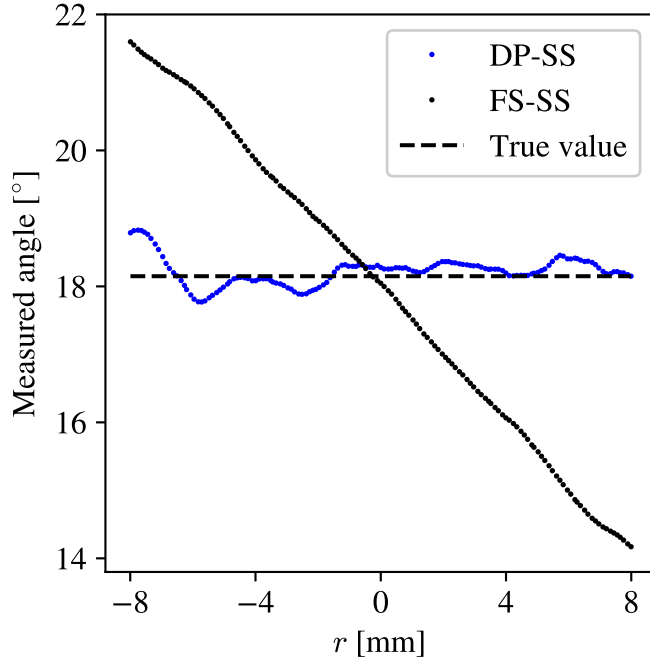
2.6.3 Floating object

As we saw in Sec. 1.2, the theoretical profile of the liquid around simple floating objects takes the form of a capillary multipole (Eq. (1.28)). In the case of a spherical particle with a constant contact line, the liquid deformation h is reduced to a capillary monopole, being the product of a capillary charge Q and a modified Bessel function of the second kind of order 0 as expressed by Eq. (1.16). This expression can be fitted on experimental profiles to compute capillary charges. Fig. 2.11 shows the typical surface profile around a heavy sphere.
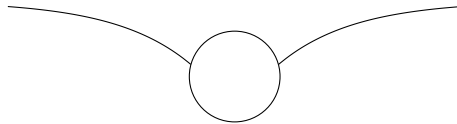

Fig. 2.11: Sketch of the surface deformation around a heavy floating sphere (the density of the sphere is greater than the density of the liquid). The surface profile around the particle takes the form of capillary monopole and the depth of deformation can be characterized by a capillary charge.

In the FS-SS and FCD methods, the displacement field depends on the liquid height as one can see on Fig. 2.3. To reconstruct the interface, Moisy et al. [98] established a relationship (see Eq. (2.1)) between the displacement field and the surface gradient that implies the mean liquid height. If the liquid height is not measured accurately or changes during the experiments, it will cause (large) errors on the reconstructed interface. In the case of a floating sphere, it will impact the capillary charge Q. As an example, the capillary charge of a floating sphere of 3 mm radius have been computed with the FCD method for a water bath of 7.04 mm deep and underestimation of this depth of 5% and 10% have been considered. The results are shown in Tab. 2.1. As expected given Eq. (2.1), the capillary charge is overestimated (in absolute value) when the water depth is underestimated. The error on the capillary charge is not so important in this case because a 4 mm thick glass plate is placed between the pattern and the container. This attenuates the change in the effective distance h_s that appears in Eq. (2.1).

Water height [mm]	Capillary charge [mm]
7.04	-0.679
7.04 - 5%	-0.719
7.04 - 10%	-0.743

Tab. 2.1: Capillary charge of a floating sphere measured with the FCD method in a water bath of 7.04 mm deep. Errors on the liquid height impact the capillary charge. For example, the effects of underestimating the water height by 5% and 10% are shown. The sphere has a 3 mm radius. The displacement fields were computed with the FCD algorithm written by Wildeman [110].

In the DP-SS method, the surface gradient can be computed exactly with Eqs. (2.6)-(2.9), and these computations do not imply the liquid height. In order to check that the reconstructed interface is really independent of the liquid height, we measured the deformations around a 3 mm radius sphere floating in water baths of different depths and we fitted the experimental data with Eq. (1.16). The FCD algorithm written by Wildeman [110] is used to compute the displacement fields. Fig. 2.12 shows the mean profile around the sphere in water baths of 10.84 mm and 7.04 mm deep. The data overlap and are in good agreement with the theoretical profile. The capillary charges obtained by fitting the experimental points are similar (see Tab. 2.2). The DP-SS method recovers well the same profile (and thus the same capillary charge) in both water baths without measuring the liquid height. The displacement fields on the top pattern are illustrated on Fig. 2.13 for the 7.04 mm deep bath. Similar displacement fields are obtained on the bottom pattern. Fig. 2.14 shows the reconstructed surface.

Fig. 2.12: Mean profile of the surface around a 3 mm radius sphere floating in water as a function of the distance r from its center. The measurements were done with the DP-SS method for water baths of 10.84 mm and 7.04 mm deep. The data overlap and are in good agreement with the theoretical profile (Eq. (1.16)). The displacement fields were computed with the FCD algorithm written by Wildeman [110].

The measurements of the DP-SS method are also compared with those of the FCD method. Fig. 2.15 shows the mean reconstructed profile of the surface around the 3 mm radius sphere floating in a water bath of 7.04 mm depth with both methods. The profile recovers with the FCD method is similar to the one obtained with the DP-SS method.

Water height [mm]	Capillary charge [mm]
10.84	-0.631
7.04	-0.623

Tab. 2.2: Capillary charges of a floating sphere measured with the DP-SS method in two water baths of different depths. Both capillary charges are similar, confirming that the method is well independent of the liquid height. The sphere has a 3 mm radius. The displacement fields were computed with the FCD algorithm written by Wildeman [110].

(a)

(b)
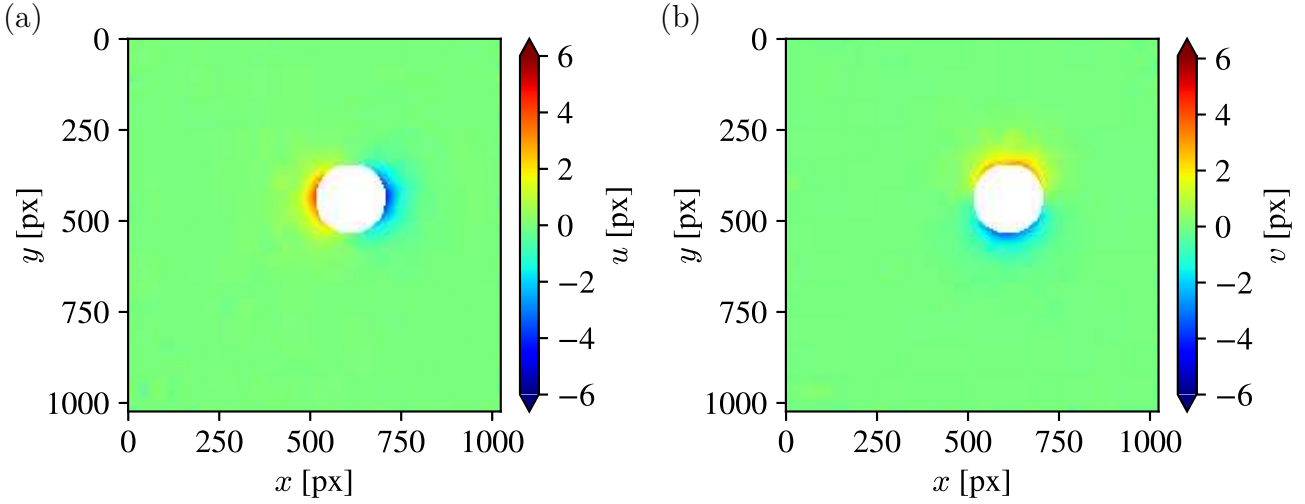
Fig. 2.13: Measured displacement fields on the top pattern for a 3 mm radius sphere floating in water. Similar displacement fields are obtained for the bottom pattern. The water bath is 7.04 mm deep. (a) Displacement field u along the x direction. (b) Displacement field v along the y direction. The displacement fields were computed with the FCD algorithm written by Wildeman [110]

Fig. 2.14: Reconstructed surface around a 3 mm radius sphere floating in water bath of 7.04 mm deep with the DP-SS method. The displacement fields were computed with the FCD algorithm written by Wildeman [110]
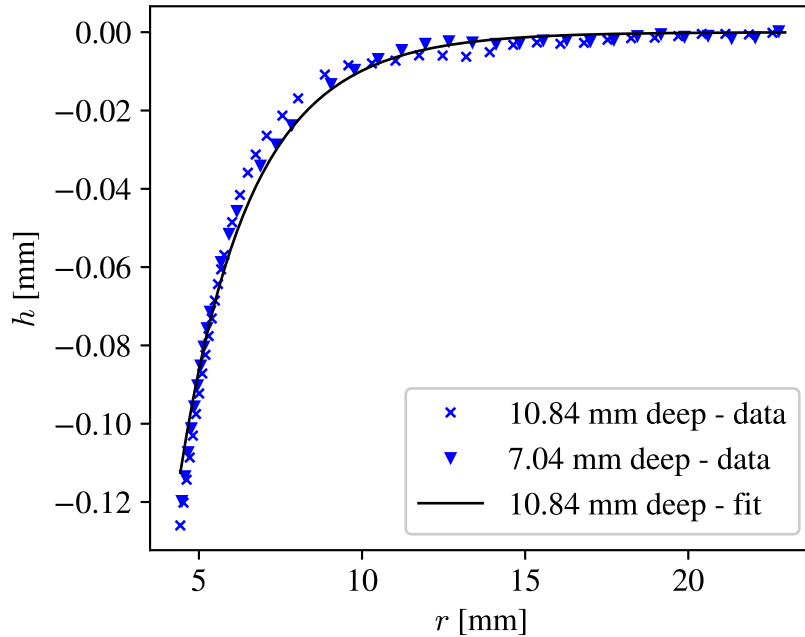
Fig. 2.15: Mean profile of the surface around a 3 mm radius sphere floating in water as a function of the distance r from its center. The measurements were done in a water bath of 7.04 mm deep with the FCD and DP-SS methods. The displacement fields were computed with the FCD algorithm written by Wildeman [110].
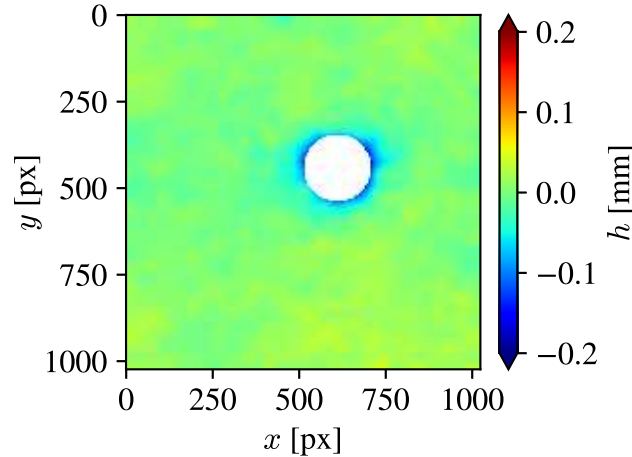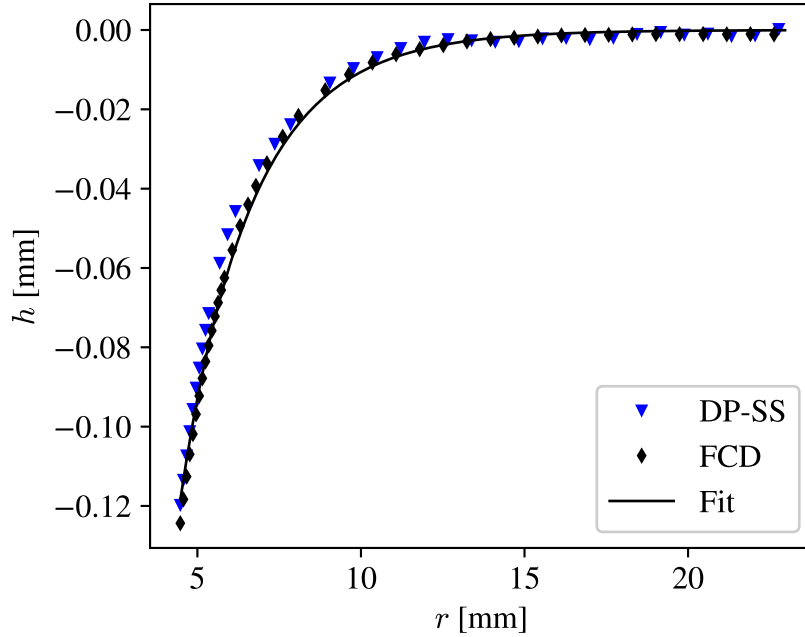
2.7   Summary

This thesis is based on the deformations of a liquid interface. Therefore, a reliable and efficient method to measure the topography of a surface is required. Among the different methods that exist, the BOS technique has been chosen because it is non intrusive, adapted for a transparent liquid, it only requires a simple optical setup and it has already been successfully used to image small waves and deformations caused by mesoscopic objects [51, 83, 84, 85, 86, 87].

BOS was adapted to various experiments and Moisy et al. [98] characterize in 2009 the FS-SS method, an implementation of BOS to measure the topography of the free surface of a liquid. We presented the principle of BOS and described the FS-SS method. Some improvements have been proposed to this technique and we were particularly interested in the FCD method. We considered this latter because it improves significantly the resolution and the computation speed while keeping the simple optical setup of the FS-SS method.

Despite its advantages, the FCD method, as the FS-SS method, is limited to weak deformations. In the case of floating mesoscopic particles, the interface is disturbed in the neighbourhood of the object and the deformations can be considered small. However, if the surface is shaped by local actuators, the slopes can become large. To overcome the limitation of the FCD method, a new method, the DP-SS method, was proposed. It uses a bitelecentric objective and a double pattern in order to avoid geometrical approximations and enable to measure moderate slopes and deformations. Strong or very strong curvatures still cannot be measured because of ray crossings, which is a drawback inherent to BOS technique.

We showed that the addition of the bitelecentric objective simplifies greatly the geometry of the light rays. A relationship between the gradient field and the incident angle can be immediately obtained without approximations. We also showed that a double pattern, composed of two patterns at specific heights, allows to compute the incidence angle without approximations and without measuring the height of the transparent medium. The DP-SS

method opens the way to new applications in which the liquid height varies or cannot be easily measured. We demonstrated in two different experimental situations the advantages of the proposed method.

To successfully measure moderate to large deformations, however, the DP-SS method must sacrifice the simplicity of the optical setup, which is its main drawback. The field of view is limited by the bitelecentric objective but remains large enough for this work. With the double pattern, the DP-SS is also more time consuming and the digital image analysis is a bit more difficult to perform.

In the rest of this thesis, we will measure the deformations of a water surface caused by controllable objects or local actuators in order to understand how floating particles can be assembled and manipulated. Depending on the extent of the deformations, the FCD or the DP-SS method will be used. For weak slopes, as it should be the case for controllable mesoscopic components, the FCD method will be preferred as it gives similar results to DP-SS method but is simpler. When the deformations will become too large to be accurately measured by the FCD method, the DP-SS method will be used. In Chap. 3, the first measurements were performed by the FS-SS method because they were made before the development of the FCD method.

3 Assembly of controllable floating components

As explained in Chap. 0, the aim of this thesis is to manipulate and assemble floating meso-scopic components by deforming the liquid surface and exploiting capillary forces. To achieve this, the prerequisite is to be able to image a fluid-fluid interface and that was the topic of Chap. 2. Now that we have implemented reliable methods to measure the topography of a liquid interface, we can start to develop strategies to reach our goal.

The first strategy we propose is to build controllable components that create specific defor-mations of the surface in their neighbourhood. As it was explained in Chap. 1, the deformations of the interface caused by floating components induce capillary interactions that lead to their self-assembly. The main difficulties are to create the right interactions and manage to modify them.

In the literature, numerous examples of capillary driven self-assemblies are given [112, 113], but creating complex structures or functional systems is still a challenge [12]. Different techniques have been proposed to create particular deformations around a floating object as it can be seen in Sec. 1.6.2. To build controllable components, we choose to start with cross-shaped particles as Poty et al. [51].

This chapter first presents the design of cross-shaped floating objects that are able to change their interactions by the application of an external field. Then, it shows how these controllable components can interact to form a self-assembly that is able to switch reversibly between two structures. Next, some asymmetry is introduced in these entities to transform them into rotating swimmers and create a rotating reversible self-assembly.

3.1 Controllable floating components

Controllable components that are able to change the structure of their assembly allow to create functional systems that can lead to new technologies and applications. To build such compo-nents, we use liquid vinylpolysiloxane (Zhermack Elite Double 32) to produce soft cross-shaped objects by polymer moulding. This polymer has a low Young modulus ($E = 1.332\,\mathrm{MPa}$), which allows relevant elastic deformations [114]. As illustrated in Fig. 3.1, the cross-shaped com-ponents have a hole in their center in order to favour significant deformations of the four branches. Their sides are also beveled so that the liquid could be pinned at the edges of the top face when it floats. Near the center, a neodymium magnet (1 mm thick) is inserted in each branch. The branches are 10 mm long and 4 mm wide.

When the soft components are placed in a vertical magnetic field, the magnetic dipoles tend to align themselves with the field orientation. This induces a deformation of the branches, as

illustrated in Figs. 3.1 (a) and 3.1 (b) where the effect of respective downwards and upwards fields are shown on the same object. If a component is deformed when it floats at the surface of a liquid, capillary charges are expected to appear at the extremities of the branches. The magnetic field is generated by Helmholtz coils. As the objects will float in the center of the coils, the magnetic field can be considered as nearly uniform.
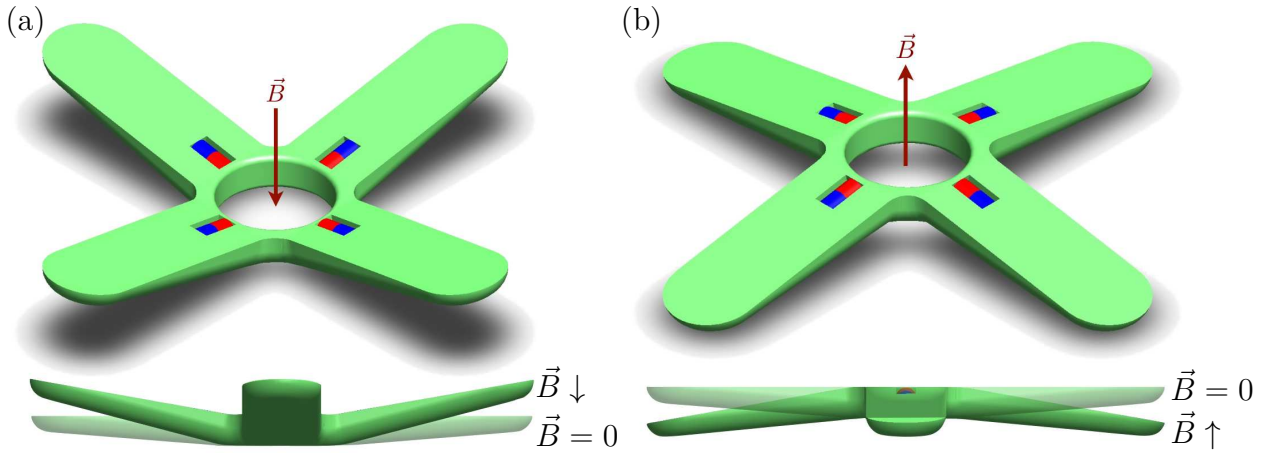

Fig. 3.1: Close view and side view of the cross-shaped soft object we consider in this section. All magnets are oriented towards the center of the object. (a) When submitted to a vertical downwards field, the dipoles inserted in the branches induce a positive deformation. (b) When the field is reversed, the dipoles induce a negative deformation of the branches.

Depending on the orientation of the dipoles, the deformation of the branches in a vertical magnetic field can create either positive or negative capillary charges. Various configurations of capillary charges on a component can be considered, which allows to control repulsion /attraction between identical floating particles. In this thesis, we decided to work with a single configuration with all dipoles pointing on the center, as sketched in Fig. 3.1. Following the previous work on cross-shaped objects carried out by Poty et al. [51], it is expected that components with similar capillary charges on all tips will self-assemble into a square lattice. Other configurations can be obtained with magnets having different orientation in the branches. The number of branches and their length ratio can also be modified to reach other structures.

Due to the moulding process, all the parts of a component are not in contact with the same material when the vinylpolysiloxane cures. This has an impact on their properties, especially their hydrophobic/hydrophilic behaviour. Therefore, the contact angles of the different parts of the cross-shaped objects were measured with a contact anglemeter CAM 200 from KSV Ltd. All the surfaces of the component are hydrophobic: the side and the lower faces, in contact with the material of the mould, have a contact angle $\theta_l = 133 \pm 1°$ and the upper face, in contact with air, has a contact angle $\theta_u = 98 \pm 1°$. Thanks to their hydrophobic nature, these objects are partially wetted when they float at the surface of water. With the bevelling of their sides, the edges between the upper and the side faces are sharp (see Fig. 3.1). The components being denser than water, the meniscus will therefore be pinned on these sharp edges [115]. Pinning means that contact angle is no more a key property of our objects.

3.2   Self-assembly of controllable components

When the controllable components are deposited on a liquid-air interface, they will deform the surface and experience interactions with their neighbours that may lead to aggregation

into specific structures. In the absence of external magnetic field, the pining of the contact line on the upper side of the objects insures that weak capillary charges are created and so, the components experience only weak capillary interactions. In addition to the capillary interactions, the permanent magnets located near the center of the floating bodies result in a small magnetic repulsion between dipoles coming from neighbouring components. This magnetic repulsion dominates the interactions between the objects as we will see later. When an external magnetic field is applied, the branches bend and capillary charges are created at the tips of the cross-shaped components, which should lead to their self-assembly into a specific structure.

3.2.1   Experimental device

In order to study the self-assembled patterns of the proposed controllable components, a large container filled with water is used. Its sides have a sharp triangular edge that can be used to pin the liquid interface and adjust the curvature of the surface. The container is placed into Helmholtz coils producing a vertical and uniform magnetic field, ranging from 0 G to 55 G. To observe the components, a camera is placed above the container. Fig. 3.2 shows a sketch of the experimental device.
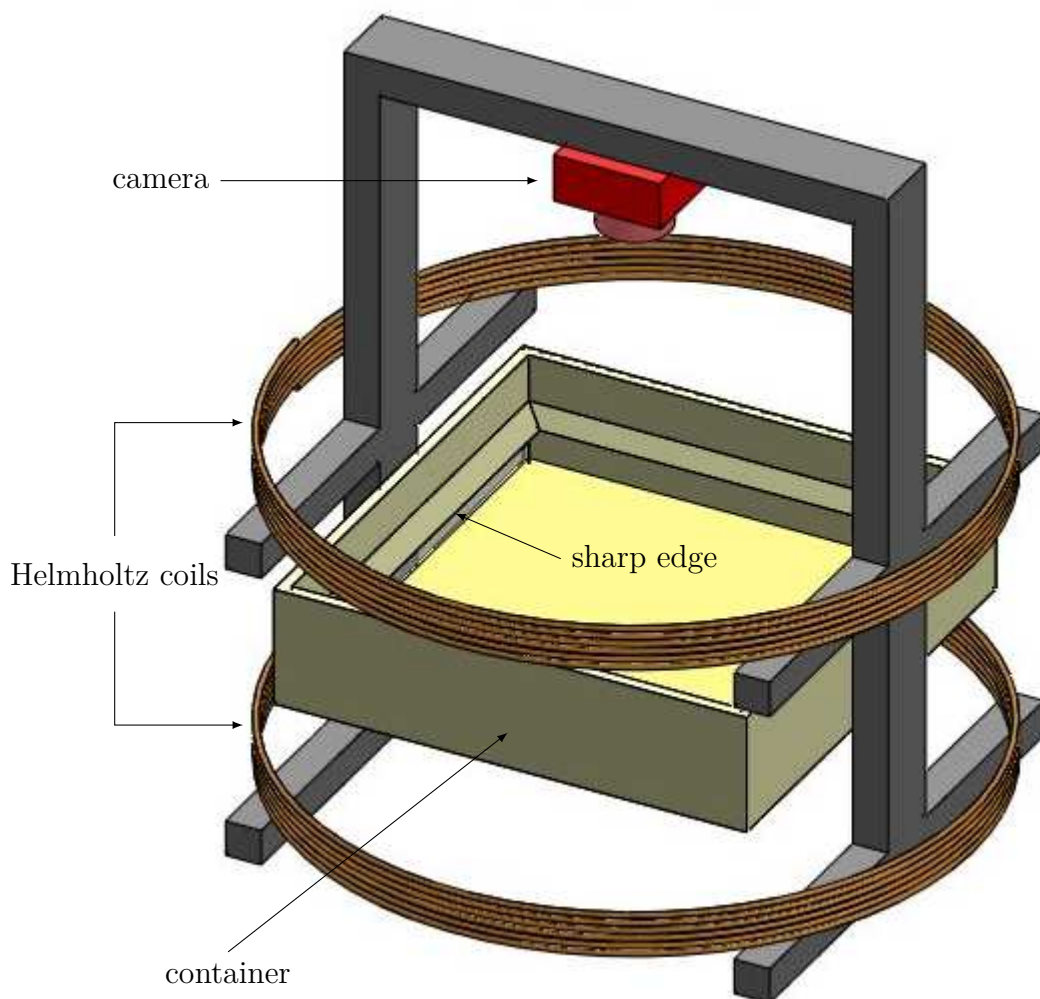

Fig. 3.2: Sketch of the experimental device used to control the assembly of our floating components. The triangular edge on the sides of the container allows to pin the liquid interface and control the curvature of the surface.

To characterize the deformations of the interface caused by the controllable components and quantify their capillary charges, the FS-SS method, described in Sec. 2.2, was used. The other techniques presented in Chap. 2, FCD and DP-SS methods, were implemented later.

3.2.2 Controllable components

We first studied the deformation of the water surface around a single controllable component with and without an external magnetic field. Imaging these deformations allows to compute capillary charges and understand how several components will interact.

The experimental profiles were measured with the Free-Surface Synthetic Schlieren method [98] that was described in Sec. 2.2, and are shown in Fig. 3.3. In the absence of magnetic field, we expect weak deformations around an object because of the sharp edges that pin the contact line. Nevertheless, Fig. 3.3 (a) shows a significant downwards meniscus around the center of the component. The object being denser than water, this is the consequence of its weight. Around the branch tips, only (very) weak deformations of the surface are observed. However, because of the downwards meniscus around the center and its softness, the component can naturally bend and weak upwards deformations can appear at its tips as we will see later.

When the vertical magnetic field is switched on, the dipoles tend to align and bend the branches upwards. Positive deformations are therefore expected at the tips of the component. Fig. 3.3 (b) shows that such positive menisci are well obtained. We can also observe that the downwards deformation around the center of the object seems strengthened. This can be easily explained. When a dipole tends to align with the external field, the tip of the branch rises up while the other end pushes on the liquid surface, increasing the deformation at the center.

As it was explained in Chap. 1, the deformations of a liquid surface by a floating object can be characterized by capillary charges. These charges can be used to compare the menisci created by different particles and quantify their interactions. In the literature [20, 21, 22, 32, 33, 36], theoretical calculations consider mainly spherical particles because of the extreme difficulty to compute an analytical (and even a numerical) expression of the deformation of the interface around an object with complex geometry. For the general case of a floating sphere with an undulated contact line, we saw that the profile of the interface around the object can be expressed as a capillary multipole with Eq. (1.28). However, the proposed controllable components are clearly not spherical. As we can see on Fig. 3.3, the deformations of the surface are localised around different parts of the object: a downward meniscus around the center and an upwards meniscus at each tip. Therefore, we modelled the controllable component as a set of spherical particles: one at the center and four at the tips of the branches. A capillary multipole is attributed to each of these particles and the total deformation due to the component is obtain by summing all the contributions, following the superposition principle used in the Nicolson method [21].

According to the observations we made on Fig. 3.3, the downwards deformation around the center of the component can be represented by a capillary monopole Q_c. Concerning the branches, as the tip rises up while the other end pushes the surface, they are modelled by dipoles located at the middle of the branches. As the component is symmetrical, all dipoles are considered identical. They correspond to a charge $-Q_{br}$ at the center of the object and an opposite charge $+Q_{br}$ at the tip of the branch. The total deformation caused by a controllable component is given by the sum of the central monopole and the four dipoles on the branches.

This model was fitted on the data of Fig. 3.3 with only two fitting parameters, Q_c and Q_{br}. The positions of the charges and the orientations of the dipoles were determined with Fig. 3.3. The monopole and the dipoles were computed with Eq. (1.28) taking $m = 0$ and $m = 1$ respectively. Fig. 3.4 shows the resulting surface profiles. Despite its simplicity, we can

observe that the proposed model is in good agreement with the experimental data, especially when a vertical magnetic field is applied to the controllable component.
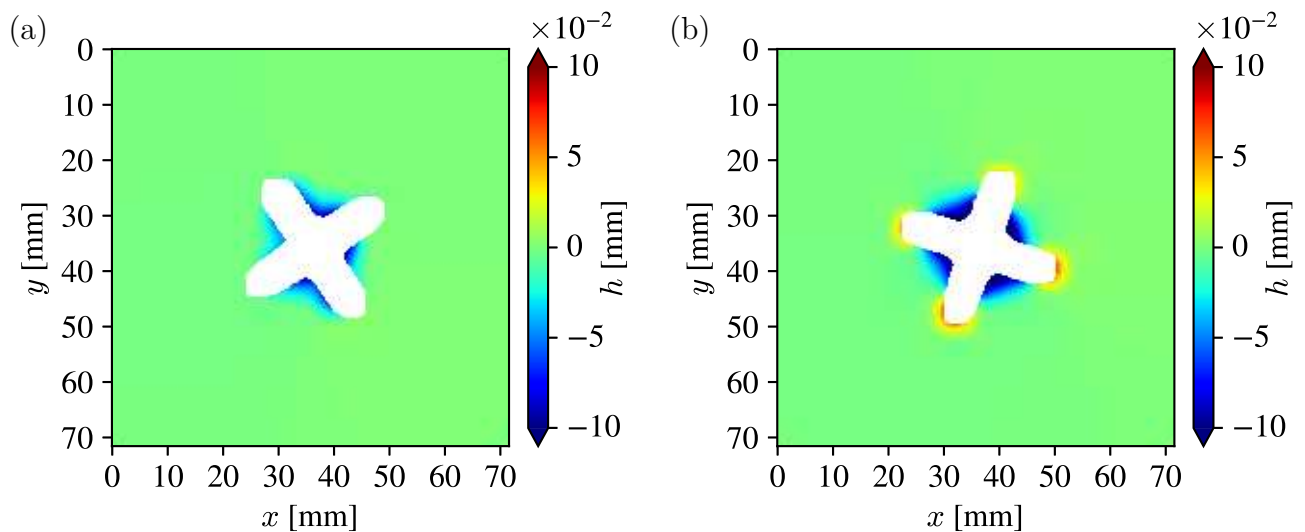

Fig. 3.3: Profile $h(x, y)$ of the water surface around a controllable component in a color scale, as measured by the Free-Surface Synthetic Schlieren method [98]. (a) Free floating crossed object with $B = 0$. The natural deformation creates a downwards (blue) deformation near the center. Weak upwards deformations may appear at the branch tips. (b) When the magnetic field is switched on ($B = 41\,\mathrm{G}$), the upwards deformations are well pronounced at branch tips. Capillary interactions between similar objects are expected to be more important in this case than in (a).
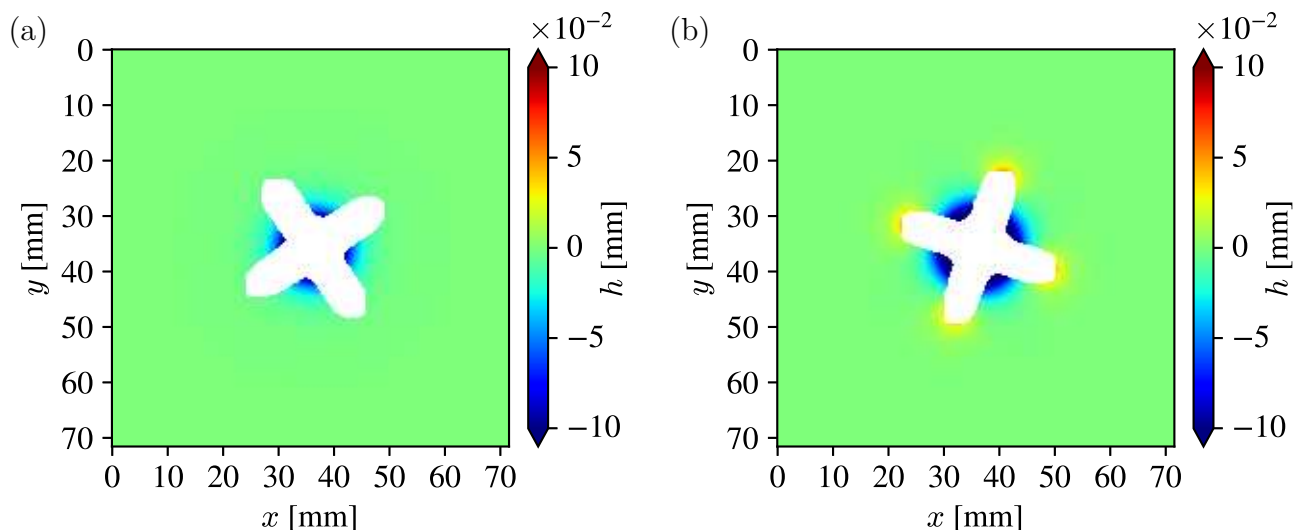

Fig. 3.4: Profile $h(x, y)$ of the liquid surface around the same controllable component as Fig. 3.3, as fitted using a model which is the superposition of a central monopole and four identical dipoles. The monopole and the dipoles have been computed with with Eq. (1.28) taking $m = 0$ and $m = 1$ respectively. The profiles should be compared to the ones of Fig. 3.3. (a) Free floating crossed object with $B = 0$. (b) Free floating crossed object when the magnetic field is switched on ($B = 41\,\mathrm{G}$).

Thanks to our model and by fitting the liquid profiles close to the tips/center, we can extract the capillary charges Q_{br} and Q_c in order to evaluate how a floating component is controlled by the external magnetic field. Fig. 3.5 shows the relationship between the external field and the dipolar capillary charge at each branch. We can observe that Q_{br} evolves linearly

61

with the external field. This dependency can be understood by considering the energies that come into play. When the magnetic field is switched on, two energies, the elastic and magnetic ones, are in competition at each branch and the energy by unit volume is given by

$$u = -\mu B \varepsilon + \frac{1}{2} E \left(\varepsilon - \varepsilon_0 \right)^2 \tag{3.1}$$

where μ is the dipole moment per unit volume, E is the Young modulus, ε is the dimensionless deformation, and ε_0 is the natural deformation on the liquid surface for $B = 0$, as evidenced in Fig. 3.3 (a). The second term of the equation, the elastic energy, is related to the capillary charge of the branch. Let θ be the angle between the horizontal plane and a branch, the dimensionless deformation can be defined as $\varepsilon = \sin\theta$. As it was shown in Chap. 1, a capillary charge can be expressed by Eq. (1.19) from the radius of the particle and the slope of the interface at the contact line. In the case of the branch of a component, considering small angles ($\tan\theta \approx \sin\theta$) the capillary charge takes the form $Q_{br} = L\sin\theta$, where L is the branch length. Therefore, the dimensionless deformation can be rewritten as

$$\varepsilon = \frac{Q_{br}}{L} \tag{3.2}$$

The equilibrium configuration is obtained by taking $\frac{\partial u}{\partial \varepsilon} = 0$ and gives

$$Q_{br} = Q_{br,0} + \frac{\mu B L}{E} \tag{3.3}$$

where $Q_{br,0} = L\varepsilon_0$ is the natural capillary charge of a branch. With these physical ingredients, a linear behaviour of the capillary charge Q_{br} as a function of the magnetic field is well obtained, in excellent agreement with the experimental data of Fig. 3.5. When the magnetic field is zero, the natural capillary charge on branches $Q_{br,0}$ is very weak, around $0.003\,\mathrm{mm}$. The ratio $\mu B/E$ could be considered as a magnetoelastic number which characterizes the ability to deform under a magnetic field.

The evolution of the central monopole Q_c as a function of the external magnetic field, which is shown on Fig. 3.6, is also linear. This can be understood from the following arguments. When the magnetic field is applied, in order to try to align, the dipoles have to rise up the tip of the branches but also push the other end downwards, as the contact line is pinned along the sharp edges of the component. The object is therefore pushed down until the vertical component of surface tension counterbalances this force. It increases the depth of the liquid deformation, in particular around the center of the object. So, it strengthens the capillary charge Q_c. However, the increase of Q_c with the magnetic field is much less important than the increase of Q_{br}. Indeed, the central monopole varies from $Q_{c,0} \approx -0.8\,\mathrm{mm}$ to $Q_c \approx -1.5\,\mathrm{mm}$ whereas the charge on the tips varies from $Q_{br,0} \approx 0.003\,\mathrm{mm}$ to $Q_{br} \approx 0.18\,\mathrm{mm}$.

These results show that the proposed components respond significantly to an external magnetic field and that the capillary charge at their tips can be easily tuned. They can therefore be considered as controllable components. Tuning the capillary charge of the tips allows to change the interactions between objects, as we will show in the following section, and to create functional assemblies able to change their structure.

It should also be noted that our results are in good agreement with the Nicolson method and Eq. (1.23). This equation tells us that the global capillary charge should remain constant if the weight of the object does not change. By bending the branches of a controllable component, we do not modify its weight. From the linear fits of Figs. 3.5 and 3.6, we can extract the derivatives of Q_{br} and Q_c as a function of B. They are respectively equal to $0.004\,\mathrm{mm/G}$ and $-0.017\,\mathrm{mm/G}$. The global charge Q_{tot} of a component being the sum of the four dipoles and the monopole, these values show that the variation of Q_{tot} as a function of the magnetic field is nearly zero, as predicted by Eq. (1.23).
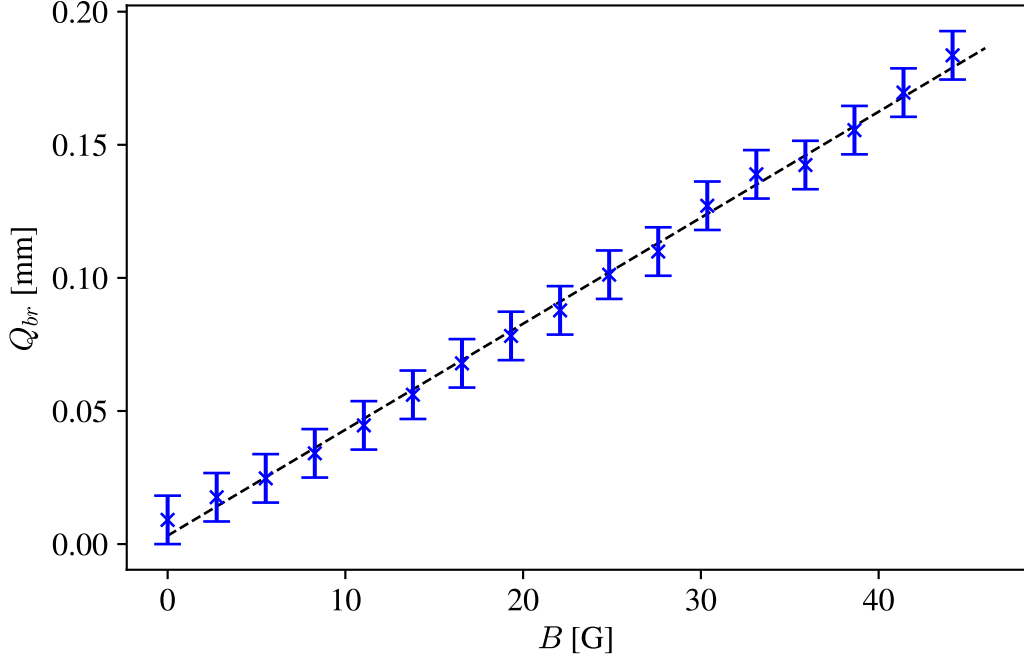
Fig. 3.5: The capillary charge Q_{br} on each dipole as a function of B. A linear trend intercepts the vertical axis determining a weak natural capillary charge $Q_{br,0} \approx 0.003$ mm, close to zero.
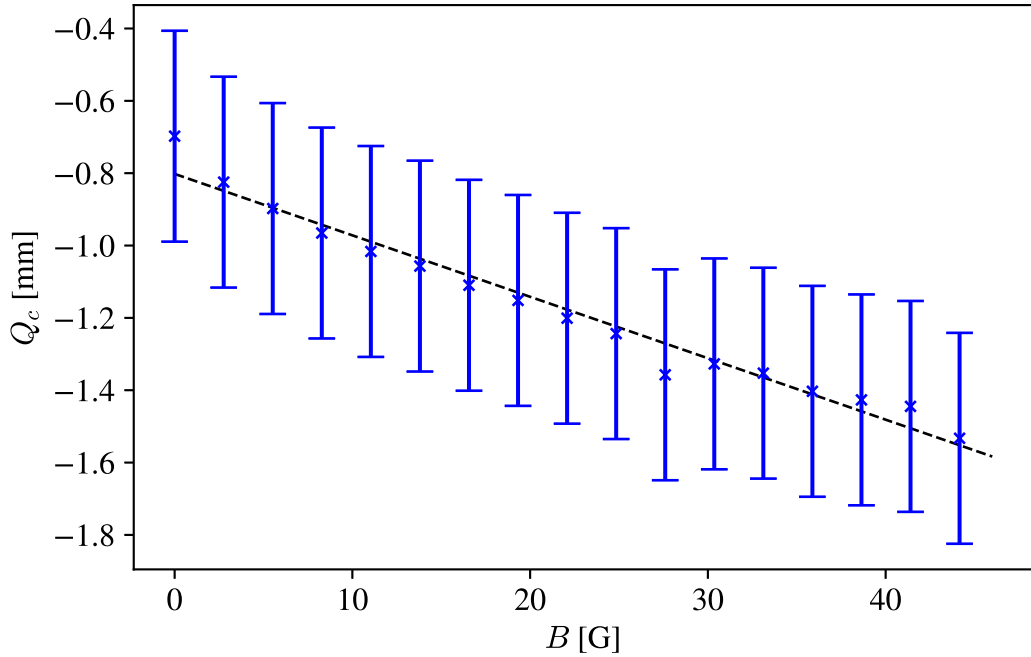

Fig. 3.6: The capillary charge Q_c of the central pole as a function of B. A linear trend intercepts the vertical axis determining the natural capillary charge $Q_{c,0} \approx -0.8$ mm.

3.2.3   Self-assemblies

Now that we know how a controllable floating component behaves in an external magnetic field, let us consider a few of them in a large container. The container has a sharp triangular edge on its sides in order to pin the contact line and avoid as much as possible the capillary interactions with the borders. Self-assembly takes place in the center of the container, where the magnetic field can be considered as nearly uniform.

Fig. 3.7 presents top pictures of the container in which freely floating controllable components are in interaction. In the first picture (a), the objects are interacting without the

presence of an external field. In this case, we saw in the previous section that the capillary charge on the branches is close to zero and that a monopole is present at the center. From Chap. 1, we know that capillary monopoles of the same sign attract (see Eq. (1.48)). Therefore, weak capillary attraction are expected between the components since there are identical. However, the objects also experienced a magnetic repulsion because of the magnets in their branches. In Fig. 3.7 (a), we can observe that this magnetic repulsion dominates the capillary attraction. Indeed, the components remain separated from each other and two neighbouring objects tend to rotate by 45° from each other. This results in a disorder structure in which the particles are separated by some distance.
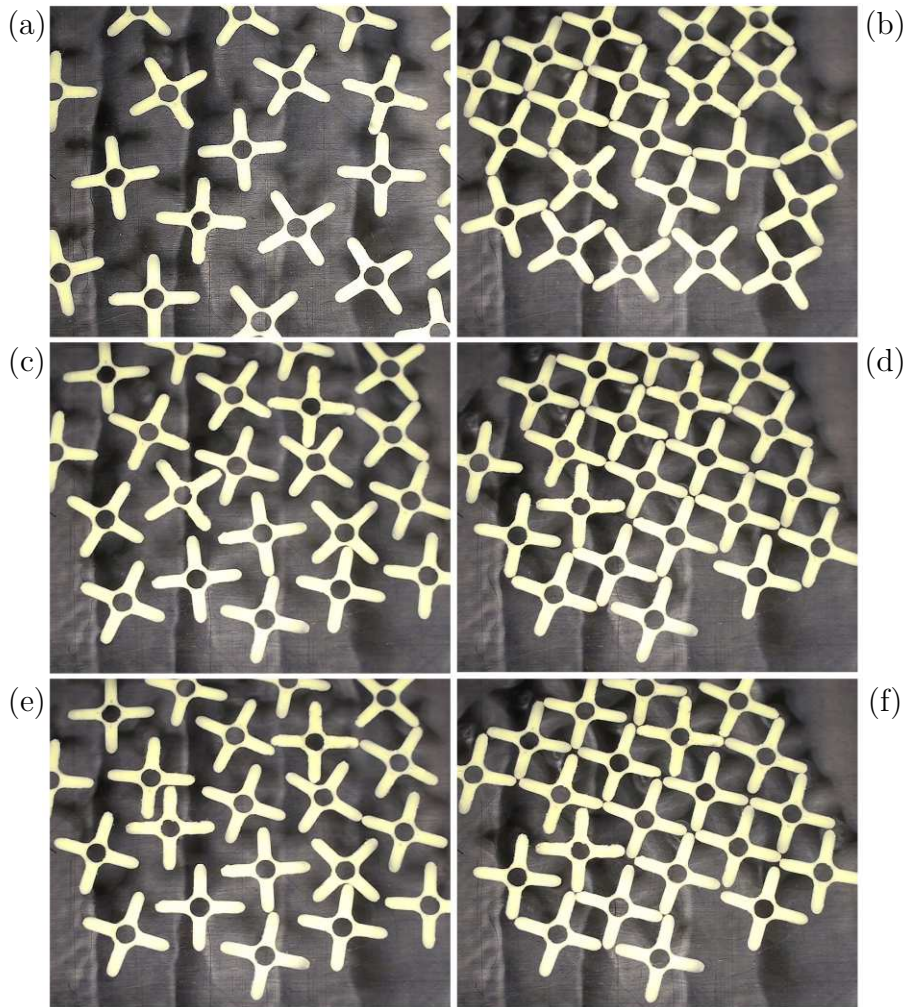

Fig. 3.7: Images of the center of the container where a few controllable components are freely floating with or without a magnetic field. The series of pictures (a) to (f) corresponds to alternating sequences during which the field is off/on. Left column: magnetic field off; right column: magnetic field on.

In Fig. 3.7 (b), a vertical magnetic field is applied through the system, starting from the situation (a). As shown in Sec. 3.2.2, dipolar capillary charges appear on the branches. The positive charges Q_{br} at the tips of neighbouring entities attract and the strength of this attraction can be tuned with the external field in order to dominate magnetic repulsion. This leads to the formation of a square pattern.

When the magnetic field is switched off, the capillary dipoles on the branches become close to zero and the magnetic repulsion again dominates the assembly. Fig. 3.7 (c) shows that a disordered structure similar to the one of Fig. 3.7 (a) is obtained. The distances between neighbouring components are reduced but this is just because the system is not yet

fully relaxed. By repeating alternating sequences during which the magnetic field is on/off (Figs. 3.7 (d) - (e)), the controllable components can switch reversibly between a square pattern and a disordered structure. Therefore, we succeed to build particles that are able to change their interaction to control their self-assembly. This opens the way to functional systems that can change their behaviour as a function of an external parameter.

Another interesting behaviour can be seen on Fig. 3.7. When the magnetic field is applied for the first time, the assembly (Fig. 3.7 (b)) is an an imperfect crystal with defects such as vacancies and grain boundaries. The components stick together but their ordering is incomplete. By suppressing (or decreasing) the external field, magnetic repulsion dominates and the objects detach from each other, keeping nearly similar positions and orientations. When the magnetic field is applied a second time, a better arrangement is obtained as illustrated on Fig. 3.7 (d).

The capillary self-assembly being reversible, cycles switching the magnetic field on/off allow a slow reorientation of the components and can be used to decrease the fraction of defects in the target structure. Indeed, the third cycle shown on Figs. 3.7 (e) and (f) improves again the pattern. The enhancement of the structure by such cycles should depend on parameters such as (i) timescales for vanishing/increasing magnetic fields, (ii) strength of the magnetic fields and (iii) cycle numbers. In addition to be able to switch between patterns, controllable components can therefore also be used to enhance crystal-like structures.

3.3 Controllable floating spinner

In the previous sections, the controllable components were subjected only to constant fields. It has recently been demonstrated that oscillating fields may be used to manipulate a floating self-assembly and induce locomotion [116, 117, 118, 119]. In (micro-)robotics, moving is an important ability. A self-assembly with this ability is therefore very interesting and can be used to perform tasks, such as mixing for example. In the following of this chapter, we will study the behaviour of our controllable components in an oscillating magnetic field and enhance them in order to obtain objects that are able to move and create a moving self-assembly.

3.3.1 Optimization of the component shape

Before applying oscillating magnetic fields on the controllable components, their design is updated in order to enhance the deformation of the branches and to decrease the central monopole. We use another liquid vinylpolysiloxane (Zhermack Elite Double 8) with a lower Young modulus ($E = 0.32$ MPa) [114]. The four branches are fixed on a central ring of 7 mm radius. The width of the branches is reduced to 2.4 mm and their length is increased to 13.6 mm in order to reduce the magnetic repulsion between neighbouring objects and achieve larger deformations. The sides of these updated components are still beveled and the same neodymium magnets (1 mm thick) are inserted at the basis of the branches. The new design of the controllable components is illustrated on Fig. 3.8.

In order to check that this new design really enhances the deformation of the branches and decreases the central monopole, we compare the surface deformations created by an "old" component and a new one for the same magnetic field. The measured liquid profiles for both objects are shown on Fig. 3.9. In the absence of external magnetic field, we see that the capillary charge of the component is strongly decreased with the new design. When a vertical magnetic field is applied, stronger capillary charges appear at the tips of the branches of the updated component. These observations demonstrate that the updated design of the object achieves its objectives.
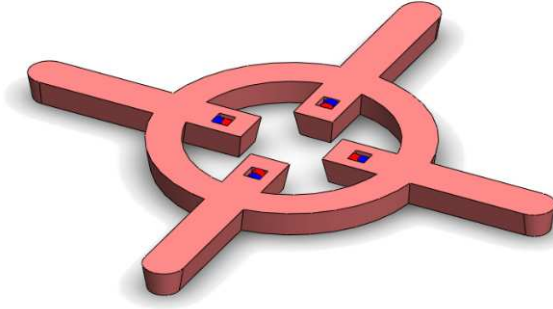
Fig. 3.8: View of the updated controllable component. This new design decreases the central monopole and enhances the deformation of the branches.
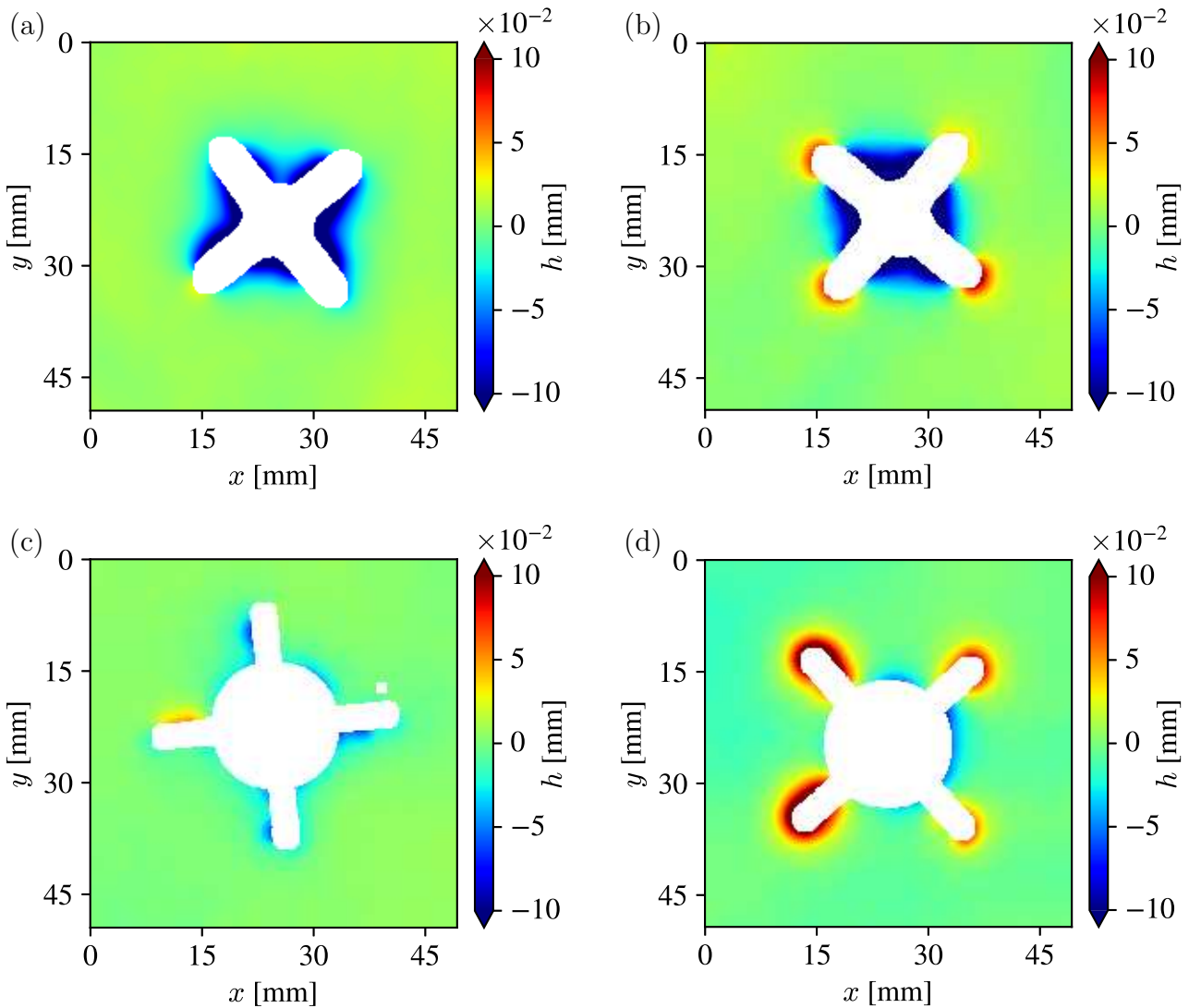

Fig. 3.9: Profile $h(x, y)$ of the liquid surface around both versions of the controllable component, as measured by the Fast Checkerboard Demodulation method [100]. (a) First version of the component when $B = 0$. (b) First version of the component when the magnetic field is switch on ($B = 34.6$ G). (c) Second version of the component when $B = 0$. With the second design, the central capillary charge is strongly decreased. (d) Second version of the component when the magnetic field is switch on ($B = 34.6$ G). The capillary charges at the tips of the branches of the second design are stronger than the ones of the first design.

3.3.2 Controllable components in an oscillating magnetic field

As we saw previously, when a vertical magnetic field is applied, the magnets inside a component tend to align with the field and bend the branches. If the external field oscillates, the branches will also oscillate between upwards and downwards bending. This movement of the branches is expected to produce waves at the surface of the liquid. Fig. 3.10 shows pictures of the water surface when a vertical magnetic field is applied to a floating controllable component. Depending on the frequency of the oscillation, different waves are observed. At low frequencies ($f \lesssim 10\,\text{Hz}$), a controllable component creates a circular wave that surrounds it. At high frequencies ($f \gtrsim 15\,\text{Hz}$), the wave field looks like ripples. It is composed of multiples waves emitted by the different parts of the component, the branches and the central circle. We can also see that the wavelength decreases when the frequency increases.

From these observations, we can conclude that two different regimes of waves exist and this is not surprising. Indeed, the equilibrium shape of the free-surface of a liquid comes from the action of both force of gravity and surface tension forces. When the surface is subjected to an external perturbation, the balance between these forces and the liquid inertia results in capillary-gravity waves [120]. In the case of shallow water, the dispersion relation of the capillary-gravity waves is given by [120, 121]

$$\omega^2 = gk + \frac{\gamma k^2}{\rho} \tag{3.4}$$

where $\omega = 2\pi f$ is the angular frequency, g is the gravitational acceleration, γ is the liquid-air surface tension, k is the wave number and ρ is the liquid density. Introducing the wave speed $c = \omega/k$, Eq. (3.4) can also be written as

$$c = \sqrt{\frac{g}{k} + \frac{\gamma k}{\rho}} \tag{3.5}$$

Depending on the wavelength $\lambda = 2\pi/k$, two cases can be identified [121, 122]:

1. For long wavelengths ($k \ll (\rho g/\gamma)^{1/2}$), the effects of surface tension are negligible and the wave is a gravity wave. Eqs. (3.4) and (3.5) can be reduced to the first term.

2. For short wavelengths ($k \gg (\rho g/\gamma)^{1/2}$), the effects of surface tension dominate and the wave is a capillary wave. Eqs. (3.4) and (3.5) can be reduced to the second term.

At the transition, when $k = (\rho g/\gamma)^{1/2}$, Eq. (3.5) implies a minimum wave speed of [121, 122]

$$c_{\text{min}} = \sqrt[4]{\frac{4g\gamma}{\rho}} \tag{3.6}$$

For water, $c_{\text{min}} = 0.23\,\text{m/s}$ and the corresponding wavelength is $\lambda^* = 1.7\ 10^{-2}\,\text{m}$ [122]. In the case of the controllable components, the perturbation of the interface is caused by the oscillation of the branches on which the interface is pinned. The frequency of the waves is therefore equal to the frequency of the external magnetic field. From the values of c_{min} and λ^*, we can compute the frequency f^* corresponding to the transition between gravity and capillary regimes. This gives

$$f^* = c_{\text{min}}/\lambda^* = 13.5\,\text{Hz} \tag{3.7}$$

This value is in perfect agreement with what is observed in the experiments. Therefore, when an oscillating magnetic field is applied on a controllable component, the long wavelengths that appear at low frequencies ($f < f^*$) are dominated by gravity effects whereas the short wavelengths that appear at high frequencies ($f > f^*$) are dominated by surface tension effects.
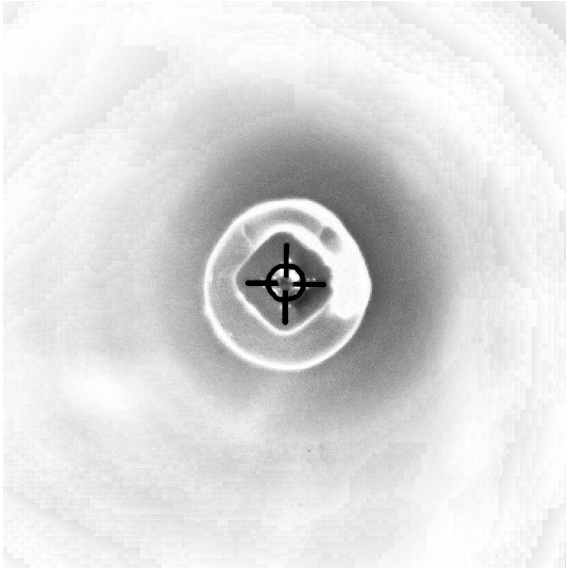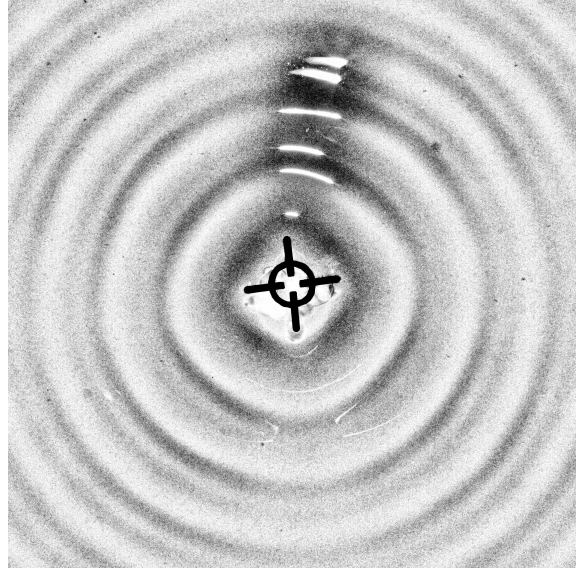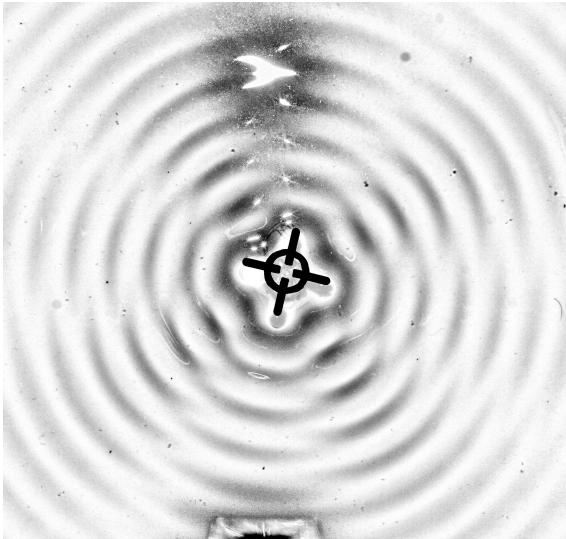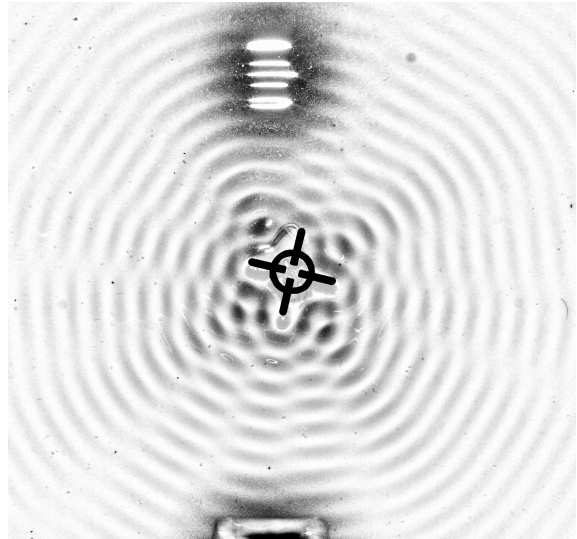
(a) $f = 8\,\text{Hz}$

(b) $f = 10\,\text{Hz}$

(c) $f = 15\,\text{Hz}$

(d) $f = 25\,\text{Hz}$

Fig. 3.10: A controllable component floating at the water surface when a vertical oscillating magnetic field is applied. As the magnets contained in the branches tend to align with the external field, the branches oscillate and create waves at the surface of the liquid. Depending on the frequency of the oscillation, different waves are observed. (a)-(b) At low frequencies ($f \lesssim 10\,\text{Hz}$), a circular wave is created. (c)-(d) At high frequencies ($f \gtrsim 15\,\text{Hz}$), the wave field looks like ripples. It is composed of multiple waves emitted by the different parts of the component.

3.3.3 Asymmetric controllable component

In the animal world, numerous techniques have been developed to achieve locomotion at the water surface [123, 124]. At the millimetre and centimetre scales, insects are a great source of inspiration for robotics. Various artificial swimmers have been built to mimic them [125, 126, 127, 128]. In particular, Rhee et al. [128] developed the SurferBot that is inspired by the honeybee. When trapped at the surface of water, this insect propels itself by emitting capillary waves. The SurferBot is a robot that is easy to build. It consists of a rectangular base, a vibration motor and a button cell battery [128]. The positions of the motor and the battery are set to give a front-rear asymmetry to the SurferBot [128]. When the motor of

the robot vibrates, this asymmetry results in the formation of a fore-aft asymmetric capillary wave field and the SurferBot makes a steady unidirectional motion [128].

The example of the SurferBot shows that capillary waves can be used to propel floating objects. However, the capillary wave field have to be asymmetrical. For our controllable components to use this strategy, we have to modify their design. As we want to keep their ability to reversibly self-assemble in a square structure, their cross shape is preserved. A triangular protrusion is added on one side of the branches in order to give them an asymmetry. In this way, two types of asymmetric components are obtained as illustrated on Fig. 3.11. Objects with a triangular protrusion added on the right (left) side of the branches are called right (left) spinners.
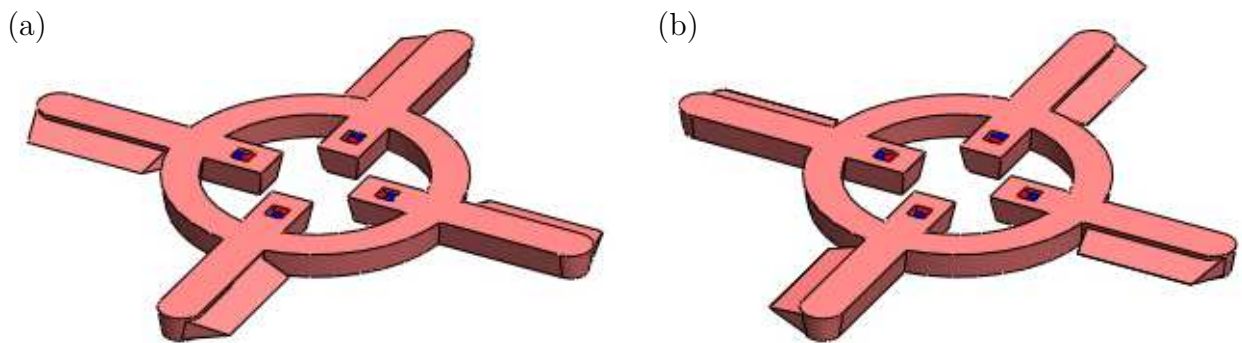

Fig. 3.11: Asymmetric floating components obtained by adding a triangular protrusion on one side of the branches. (a) Triangular protrusion on the left side of the branches (left spinner). (b) Triangular protrusion on the right side of the branches (right spinner).

When an asymmetric controllable component is placed on a liquid surface, the triangular protrusions are completely immersed. The contact line is still pinned at the edge of the top face. Similarly to the SurferBot, an asymmetric component is expected to create capillary waves of different amplitudes when an oscillating magnetic field of high frequency ($f > f^*$) is applied. Fig. 3.12 shows the resulting wave field. The half of the branch which has the protrusion is heavier and the protrusion slows down its motion. Therefore, the capillary waves generated by this half has a lower amplitude. This can be observed on Fig. 3.12 by looking near the tips of the branches. Moreover, the capillary waves created on the side of the branch with the protrusion are out of phase whereas the ones created on the other side are nearly in phase. This is highlighted by black circles on Fig. 3.12. Because of these differences, a larger amount of momentum is transferred by the halves of the branches that have no protrusion. Given the cross-shaped geometry of the components, this results in a rotation in the direction of the triangular protrusions. Objects with a protrusion on the right (left) side of the branches rotate clockwise (counter-clockwise) as shown on fig. 3.13. Our asymmetric components are therefore floating spinners. When the frequency of the magnetic field is low ($f < f^*$), capillary effects are dominated by gravity. There are no capillary waves and the components do not rotate.

In order to characterize the rotation speed of these controllable spinners, we measured their orientation when the oscillating magnetic field is on. Fig. 3.14 shows the cumulated angle covered by a spinner as a function of the time. A linear relationship is obtained and the rotation speed of the spinner is therefore constant as it was expected. Indeed, the frequency of oscillations being constant, the transfer of momentum is also constant over time. Therefore, the acceleration is zero which implies a constant speed.
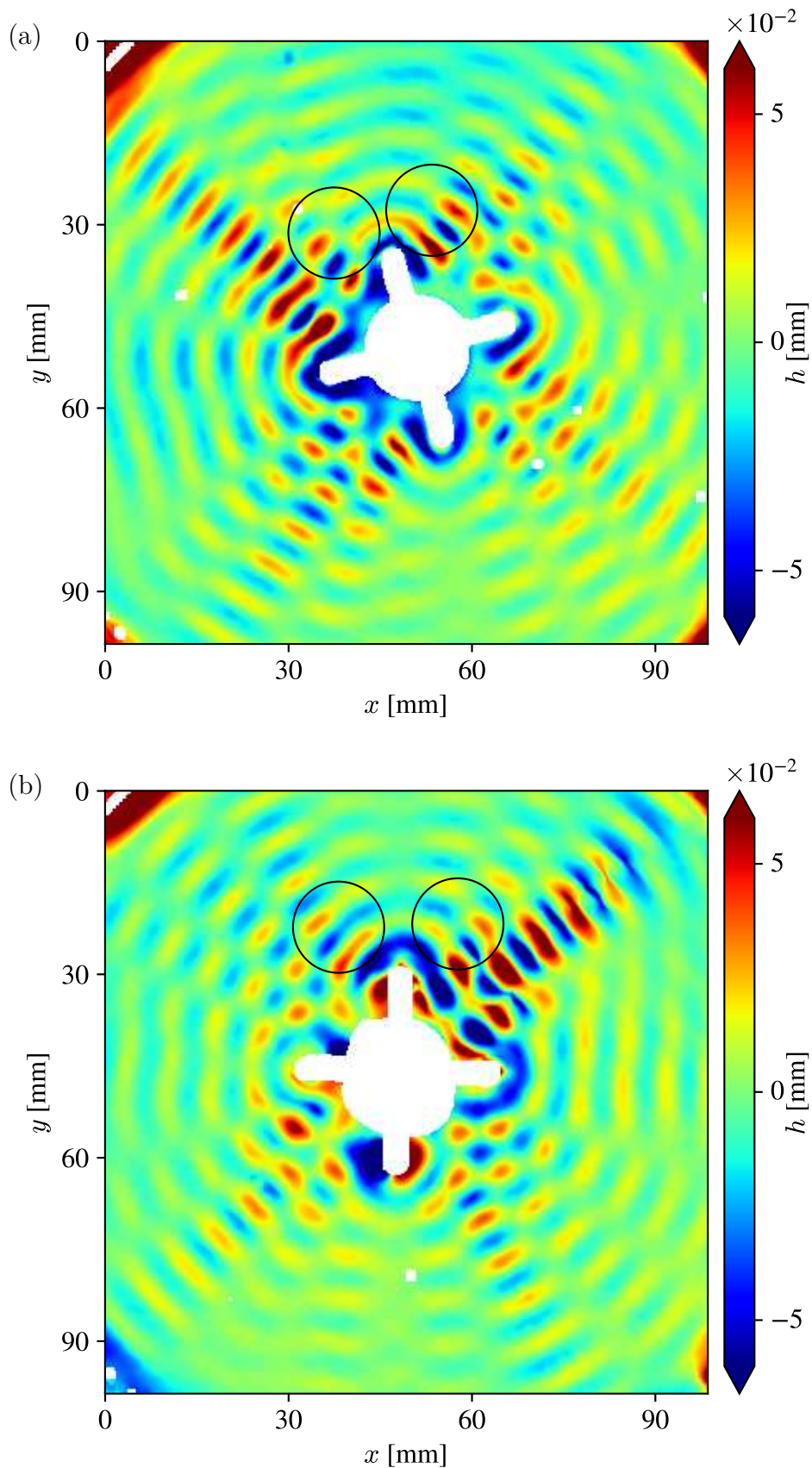
Fig. 3.12: Wave fields produced by asymmetric components in an oscillating magnetic field. These objects are obtained from our controllable components by adding a triangular protrusion on one side of the branches. The Fast Checkerboard Demodulation method has been used to measure the topography of the interface. (a) Counter-clokwise (left) spinner. (b) Clockwise (right) spinner.
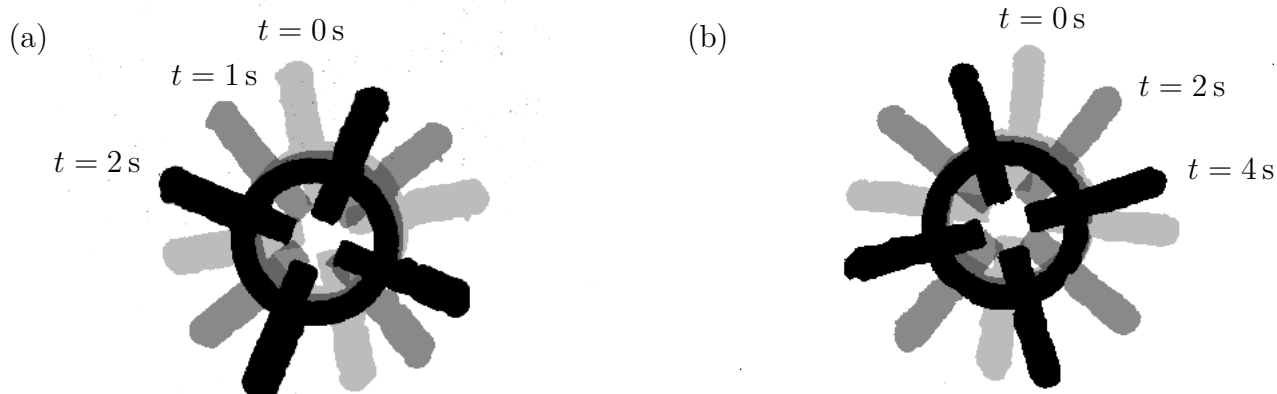
Fig. 3.13: Pictures at different time steps of an asymmetric floating component at an air-water interface when a vertical oscillating magnetic field is applied. As the less massive halves of the branches produce waves of greater amplitude, a net momentum is transfer from the liquid to the object pushing it towards the heavier half of the branches and a rotation is observed. The magnetic field has an amplitude of 21 G and a frequency of of 35 Hz. (a) Counter-clockwise (left) spinner. (b) Clockwise (right) spinner.
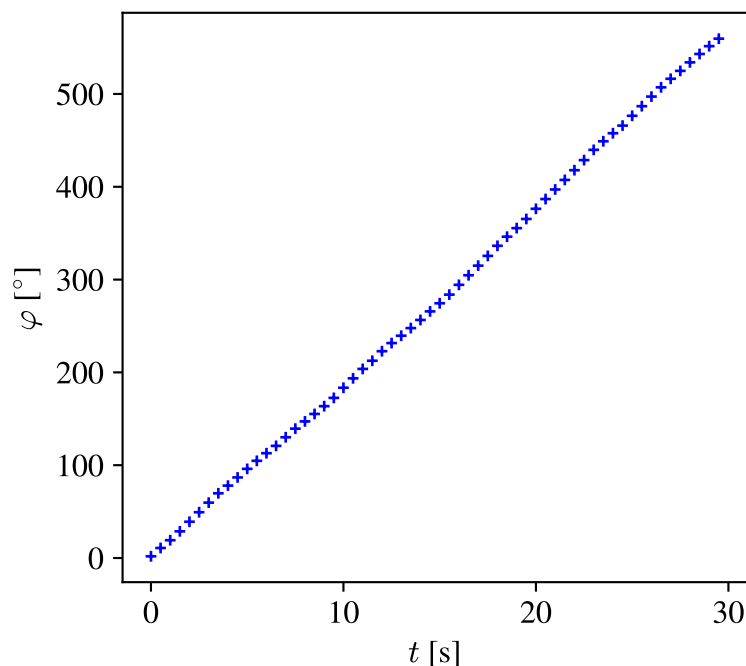
Fig. 3.14: Cumulated angle of rotation φ of a controllable spinner as a function of time t when it is submitted to a vertical oscillating magnetic field. A linear relationship is observed. The rotation is therefore regular. The magnetic field has a magnitude of 21 G and a frequency of 35 Hz.

3.4 Rotating self-assembly

With the controllable spinners, we have components that are able to rotate in a vertical oscillating magnetic field and to self-assemble in a vertical constant magnetic field. Both types of fields can be combined in order to create a moving self-assembly as illustrated in Fig. 3.15. To do that, a few controllable spinners are placed at an air-water interface. First, a vertical constant magnetic field is applied. As we previously saw, positive capillary charges are created at the tips of the branches of the objects and they self-assemble through capillary

interactions (Fig. 3.15 (a)). Then, an oscillating component is added to the constant field as illustrated on Fig. 3.16. The branches oscillate and the objects try to rotate (Figs. 3.15 (b)-(f)). However, while oscillating, the branches keep an upwards bending because of the constant offset. They still have positive capillary charges at their tips. The capillary interactions remain strong enough to keep the spinners in contact with each other, which leads to the rotation of the entire self-assembly.

With a few enhancements of the design of the floating components, the self-assembly has gained a new capacity while still being able to switch from a disordered state to a square structure. This shows that controllable components can be used to transform a simple self-assembly into a robot that can be controlled remotely. Other modifications may be considered to try to obtain an unidirectional motion.

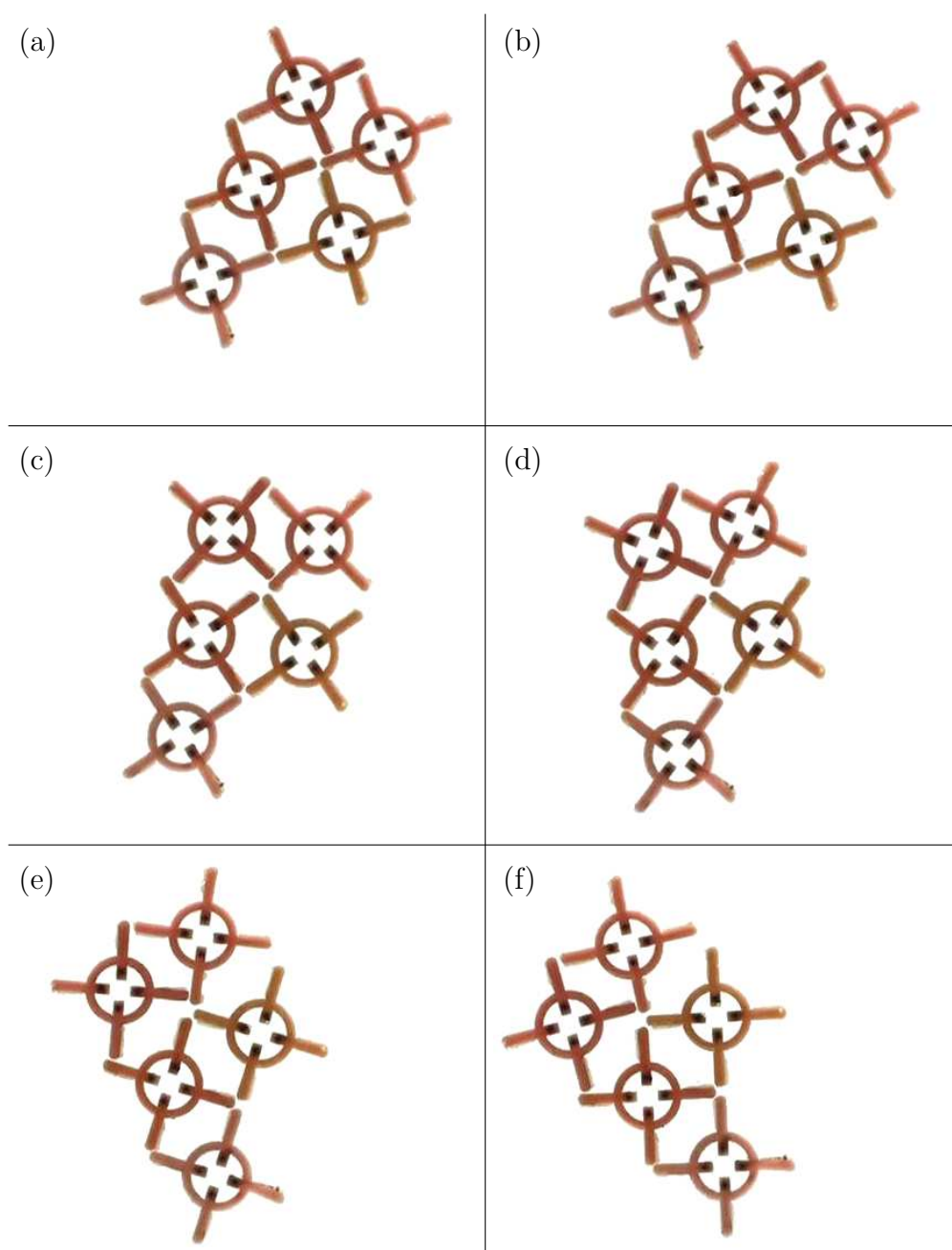**Fig. 3.15:** Rotation of a self-assembly composed of counter-clockwise (left) spinners. (a) A constant magnetic field is applied to self-assemble the objects. (b) - (f) An oscillating component at a frequency of 35 Hz is added to the constant field. By vibrating, the spinners generate capillary waves that make the assembly rotate counter-clockwise. The time step between two successive images is 8.28 s.
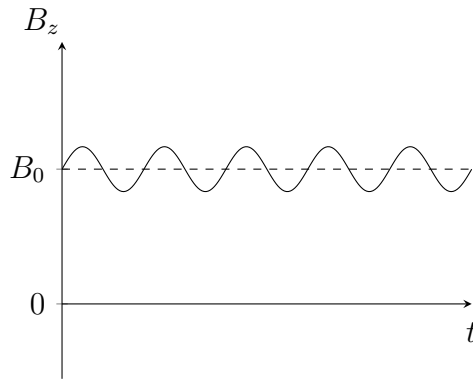
Fig. 3.16: Typical shape of the vertical magnetic field applied on a self-assembly of spinners to make it rotate. This field results from the addition of a constant offset B_0 and a sinusoid.

3.5 Summary

In order to manipulate and assemble floating mesoscopic particles, the first strategy proposed in this thesis is to build controllable components that are able to change their capillary interactions. This chapter showed how such components can be built from soft cross-shaped objects and neodymium magnets. The control of these entities is achieved with a vertical magnetic field.

We showed that the proposed floating components can be bent to deform the liquid interface. Using the superposition principle, we modelled an object as a combination of a monopole and four dipoles in order to determine its capillary charges and evaluate how it is controlled by an external magnetic field. A linear relationship was obtained between the charge at the tips of the component and the magnetic field.

In the absence of external magnetic field, the interactions between freely floating components are dominated by magnetic repulsion. This results in a disordered structure in which the objects remain at a certain distance from each other. When a vertical magnetic field is applied, the capillary charges at the tips of the components can be tuned so that the capillary attraction between tips overcomes the magnetic repulsion. This leads to a reversible self-assembly having a square pattern. However, the structure can be imperfect, with vacancies or grain boundaries for example. We showed that successive cycles switching the magnetic field off/on allow a slow reorientation of the components and reduce the fraction of defects.

When a vertical oscillating magnetic field is applied, a controllable component floating at an air-water interface emits waves. At low frequencies, these waves are dominated by gravity effects whereas capillary effects dominate at high frequencies. We showed that capillary waves can be used to create rotation of the components by adding some asymmetry between the left and right sides of the branches. The resulting spinners can be reversibly self-assembled into a square structure by applying a constant vertical magnetic field. An oscillating component can then be added to the constant field to put the entire self-assembly into rotation.

The proposed controllable components succeeded to create specific capillary interactions and change them in order to control their self-assembly. Their capacity to switch between structures can find many applications in microfabrication as creating functional systems and complex structures. Moreover, being able to perform some motion, the controllable components could be transformed into a self-assembled robot and used to performed various tasks, such as mixing for example.

4 Manipulation by local actuators

In Chap. 3, we considered a flat interface locally deformed by floating components and we actuated these components in order to control their capillary charges. This strategy allowed us to realise a self-assembly that is able to switch reversibly between two structures and even rotate. These results, among other works [43, 48, 51, 55, 87], illustrate how capillary driven self-assembly is a promising and powerful manipulation technique to create elaborated structures of a large number of particles. However, it is not always possible to modify the geometry or the properties of floating components to control their capillary interactions. Sometimes, we could also want to manipulate a single object. In both cases, the first strategy proposed in this thesis cannot be applied. Therefore, to manipulate such particles, we need another strategy that does not rely completely on the component and its design.

The second strategy proposed in this thesis is to deform globally the liquid interface with local actuators rather than locally. As it was explained in Chap. 1, a heavy (light) particle tends to go downwards (upwards) along the interface to decrease its energy. Therefore, if the interface is deformed in such a way that it takes the form of a valley (hill), a heavy (light) object will spontaneously fall (climb) to the bottom (top). The shape of the liquid surface could be adjusted by local actuators to place the bottom of the valley (or the top of the hill), and therefore the particle, at a specific location. Such a technique would have the advantage to manipulate floating objects independently of their nature. No modification of the components is required, this is the shape of the interface that is changed. Floating liquid droplets as well as bubbles would be moved and positioned as easily as hard particles.

Many applications can be found in microfabrication. Deforming the surface with local actuators could allow to control the location of a self-assembly and to place a particular component at a specific location. It could also be used to assemble heterogeneous particles in a single assembly. Other applications can be found in microfluidics. For example, floating chemicals could be mixed or transport to a specific area where they would be analysed.

This chapter first presents an actuator that is able to create locally a dipolar capillary charge. It shows then how several actuators can be combined to form capillary tweezers. Next, the ability of this device to position and transport all sorts of particles is demonstrated.

4.1 Dipolar Capillary Actuator

To build a local actuator that is able to deform a liquid surface, we were inspired by our controllable components. The same actuation mechanism, the orientation of a dipole in an external magnetic field, has been used. The proposed actuator is composed of 3 parts: a floater, a support and a coil as illustrated on Fig. 4.1 (a). The floater is a thin 4.5 mm radius disk with two cuts in its edge and a squared protrusion in its center. A 1 mm thick magnet

is inserted in the protrusion, parallel to the disk. The side of the floater is bevelled to create a sharp edge along the top face that pins the contact line. The support keeps the floater at a fixed position and consists of two pillars that pass through the cuts of the floater. The coil surrounds the pillar and the protrusion of the floater. We called this actuator the Dipolar Capillary Actuator (DCA).
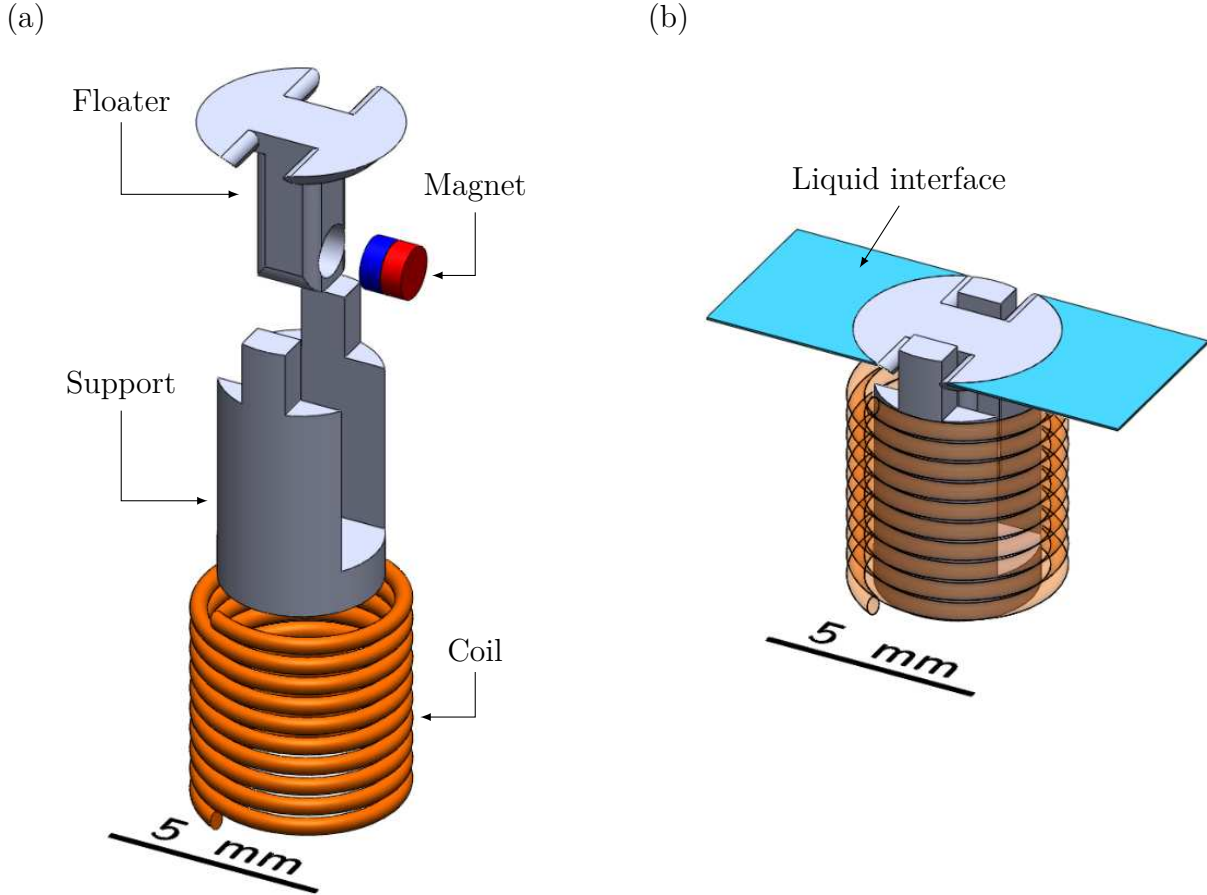
(a)   (b)

Fig. 4.1: Illustration of the Dipolar Capillary Actuator (DCA). A floater containing a small magnet is placed at the liquid interface above a support. This support has two pillars that pass through cuts in the edge of the floater. A coil surrounds the support and the magnet. (a) Exploded view of the DCA. (b) DCA placed in a liquid. The natural position of the floater is horizontal because its center of mass is just below the center of the disk.

When the DCA is placed in a liquid, the floater lies at the surface with a natural position which is horizontal because its center of mass is just below the center of the disk (Fig. 4.1 (b)). In order to deform the interface, an electric current is injected into the coil. This induces a vertical magnetic field around the magnet inserted in the floater. The magnet tries to align itself with the magnetic field which tilts the floater. Since the contact line is pinned at the sharp edge of the floater, this deforms the liquid surface. The behaviour of a DCA in a vertical magnetic field is illustrated on Fig. 4.1.

As we saw in Chap. 1, the profile h of the interface around a particle with an undulated contact line can be described as a capillary multipole. In the case of the DCA, a deformation presenting two lobes of opposite signs is expected when the floater tilts. The profile of the interface around the DCA should therefore correspond to a capillary dipole that can be mathematically expressed by Eq. (1.28) taking $m = 1$. This gives

$$h(r, \theta) = Q K_1(r/\lambda) \cos(\theta - \theta_0) \tag{4.1}$$

where θ_0 is the orientation of the device. In order to check that a capillary dipole is created by the DCA, a current was injected into its coil and the deformation of the interface was measured with the FCD method. Then, the experimental data were fitted by Eq. (4.1) to obtain the theoretical profile. Fig. 4.3 shows both results. We can observe that the measured surface presents well a dipolar deformation and is in excellent agreement with the theoretical profile.
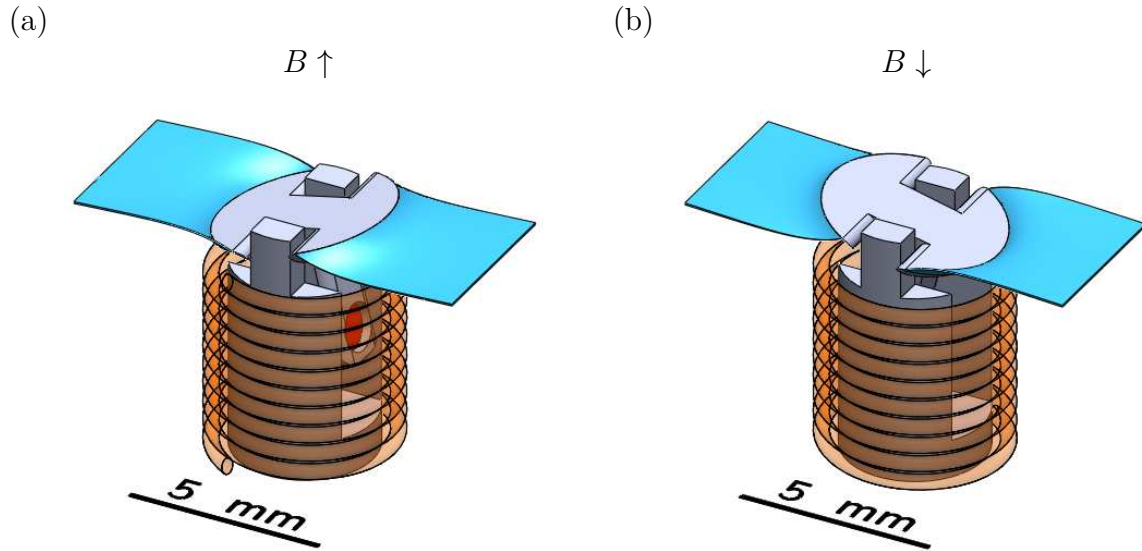

Fig. 4.2: Deformation of the interface by the Dipolar Capillary Actuator. When a current is injected into the coil, a vertical magnetic field is created around the magnet contained in the floater. The magnet tries to align itself with the magnetic field, which tilts the floater and deforms the interface. (a) Deformation of the interface when an upwards magnetic field is generated. (b) Deformation of the interface when a downwards magnetic field is generated.
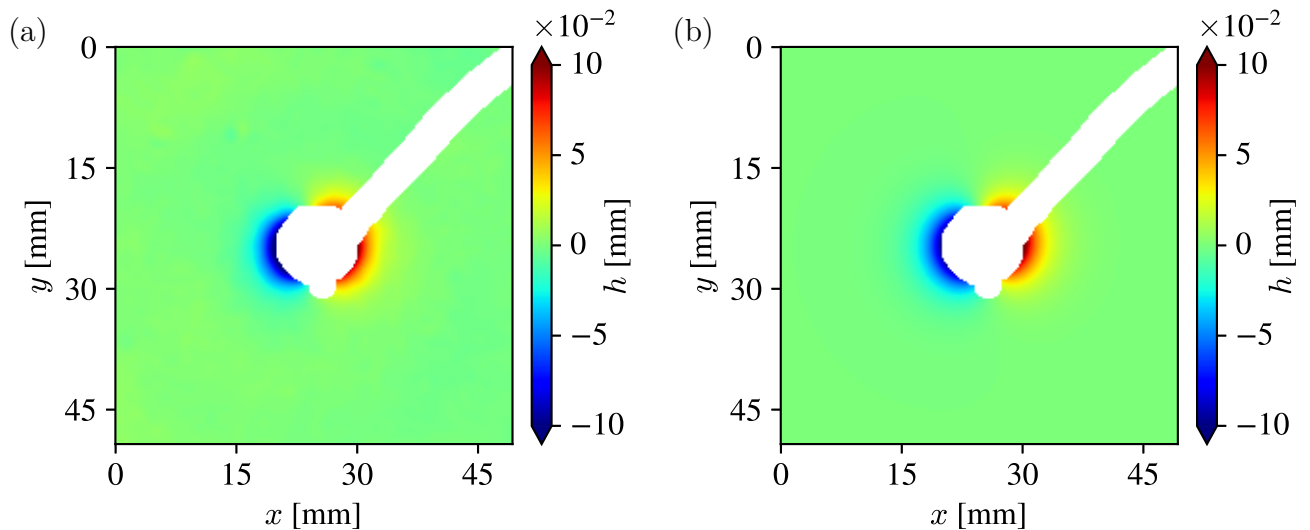
Fig. 4.3: When a current is injected into a DCA, the floater tilts and a capillary multipole is created. The resulting deformation of the interface presents two lobes of opposite signs which corresponds to a dipolar charge. The white line starting from the upper right corner corresponds to the cable that powers the DCA. (a) Surface profile around a DCA measured by the Fast Checkerboard Demodulation method. The DCA is powered by a current of 0.275 A. (b) Surface profile around a DCA as fitted with Eq. (4.1).

The value of the dipolar capillary charge created by the DCA is controlled by the current injected into its coil. Indeed, the magnetic field generated by the coil, that causes the floater to tilt, is proportional to the current into the coil. In order to determine how the deformation of the surface can be tuned with the DCA, we measured its dipolar charge $\pm Q$ as a function of the current. The charge was obtained by imaging the interface with the FCD method and fitting Eq. (4.1) on the data. Fig. 4.4 shows the evolution of the dipole created by a DCA as a function of the current injected in its coil. A linear trend is observed.
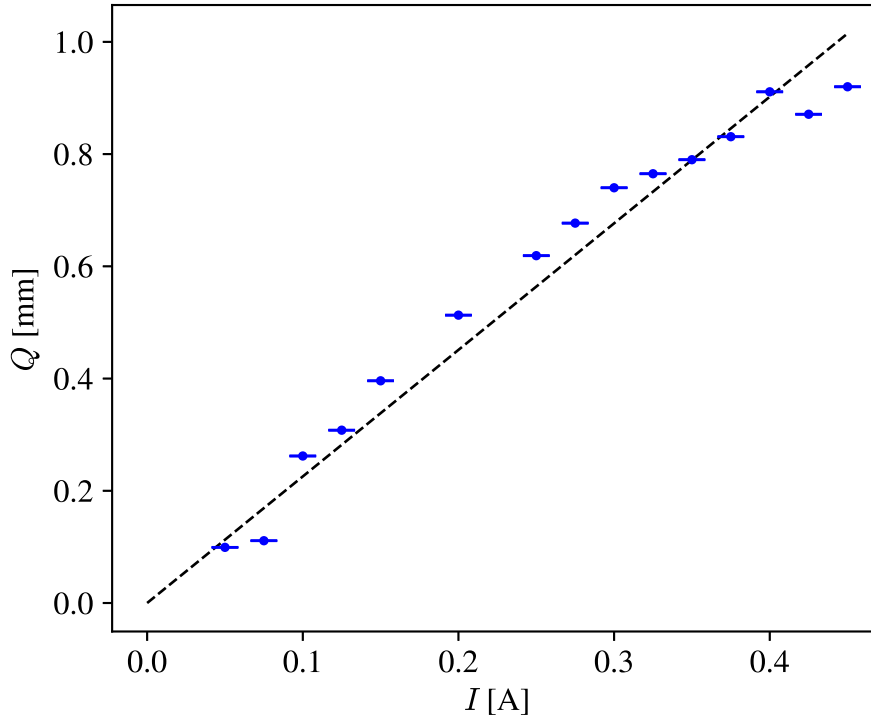

Fig. 4.4: Capillary charge of the DCA as a function of the current intensity injected into its coil. A linear trend is observed. The charge was obtained by imaging the interface with the Fast Checkerboard Demodulation method and fitting Eq. (4.1) on the data. The error bars are the errors on the capillary charge from the fit and are smaller than the dots.

The relationship between the charge of the DCA and the current injected in its coil can be understood by considering the torques that apply to a floating dipole in a vertical magnetic field. This situation is illustrated in Fig. 4.5. The dipole has a magnetic moment $\vec{\mu}$ and undergoes a magnetic torque $\vec{\tau}_B$ that tends to align it with the field . Surface tensions on both ends, $\vec{\gamma}_l$ and $\vec{\gamma}_r$, exert torques $\vec{\tau}_l$ and $\vec{\tau}_r$ that tend to bring the dipole back to an horizontal position. The equilibrium is reached when the sum of the torques is zero. Projecting the torques on an axis perpendicular to the plan of the page, this condition writes

$$\tau_l + \tau_r = \tau_B \tag{4.2}$$

Taking into account that surface tensions on both ends have the same intensity and expressing the value of the torques, the equilibrium can be rewritten as

$$2R\gamma \sin(\varphi + \beta) = \mu B \sin \alpha \tag{4.3}$$

Using trigonometric formulas, we get

$$2R\gamma \sin \varphi \cos \beta + 2R\gamma \cos \varphi \sin \beta = \mu B \cos \beta \tag{4.4}$$

Let us now consider small tilt angles. In this case, $\cos\beta \approx \cos\varphi \approx 1$, $R \approx R_c$ and $\sin\varphi \approx \tan\varphi$. Eq. (4.4) becomes

$$2R\gamma\sin\varphi + 2R\gamma\sin\beta = \mu B \tag{4.5}$$

From the definition of the capillary charge (Eq. (1.19)) and the small angles approximation, we have

$$Q \approx R\sin\varphi \tag{4.6}$$

As it can be seen on Fig. 4.5, $\sin\beta$ can be expressed as

$$\sin\beta = h_c/R \tag{4.7}$$

where h_c is the height of the interface at the contact line. From the capillary dipolar expression of Eq. (4.1) and the small angles approximation, we get

$$h_c = QK_1\left(\frac{R_c}{\lambda}\right) \approx QK_1\left(\frac{R}{\lambda}\right) \tag{4.8}$$

Replacing Eqs. (4.6)-(4.8) into Eq. (4.5), the equilibrium becomes

$$2\gamma Q + 2\gamma QK_1\left(\frac{R}{\lambda}\right) = \mu B \tag{4.9}$$

This leads to the following linear relationship between Q and B

$$Q = \frac{\mu B}{2\gamma\left[1 + K_1\left(\frac{R}{\lambda}\right)\right]} \tag{4.10}$$

As the magnetic field generated by a coil is proportional to the injected current I, a linear relationship between Q and the current is also predicted.
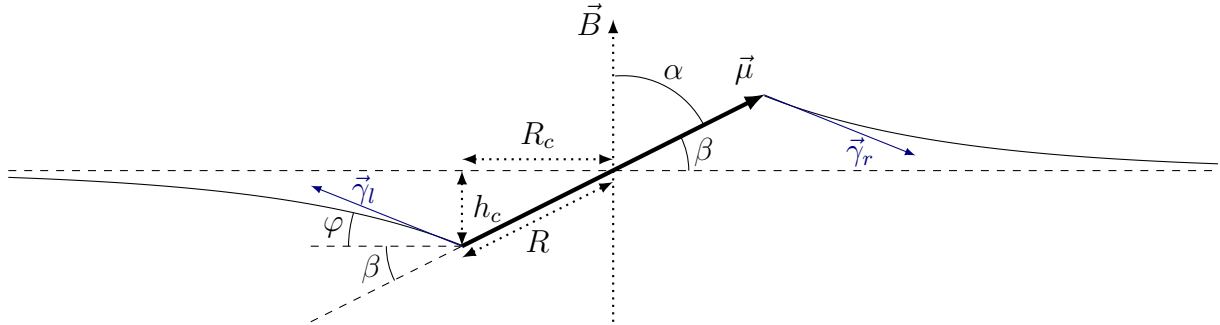
Fig. 4.5: Dipole of magnetic moment $\vec{\mu}$ floating at a liquid surface when a vertical magnetic field $\vec{B}$ is applied. The dipole tends to orient itself with the external field and deform the interface. Surface tension tends to bring the dipole back at the horizontal.

4.2 Capillary tweezers

In order to create a global deformation of the liquid surface in a specific area, a circular array of DCAs has been built. Inside this array, the distortions created by all DCAs combine. This allows to shape the surface and to manipulate floating particles. Indeed, as explained in Chap. 1, a floating particle will move along the interface to decrease its energy. By shaping the interface, we can choose the position of minimal energy. Such a device can be used as capillary tweezers.

The typical length on which the deformation of the interface decays to zero is the capillary length λ and is equal to 2.7 mm for pure water, as seen in Chap. 1. Therefore, the radius of the circular array should be in the order of the capillary length to achieve significant deformation in its centre. The proposed capillary tweezers is shown on Fig. 4.6. Its inner diameter has been set to 4.75 mm, which is a bit larger than the capillary length, in order to be able to displace millimetre particles over significant distances. The circular array consists of six DCAs that are placed symmetrically around the inner area. This is the maximum number of DCAs that can be put around a 4.75 mm circle. Capillary tweezers could be made with fewer DCAs but using more DCAs allows for more elaborated shapes of the interface inside the device as more local deformations are combined to give the total deformation. A six bi-directional current source was built to power the capillary tweezers. This source is driven by a micro-controller and the current in each DCA, and so its capillary charge, can be set individually.
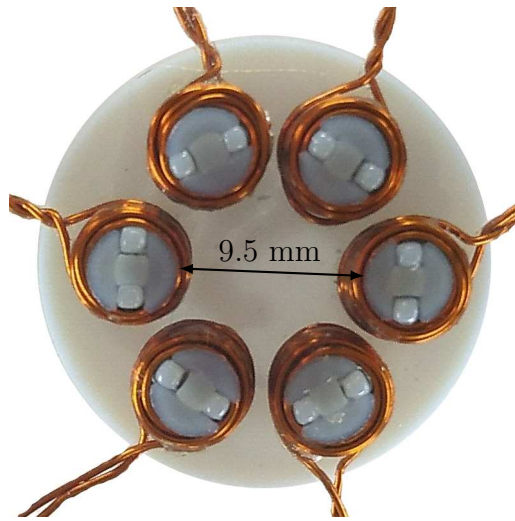

9.5 mm

Fig. 4.6: Proposed capillary tweezers to manipulate any floating particle. It is composed of six Dipolar Capillary Actuators placed along a ring that delimits a circular inner area of a 4.75 millimetres radius. The liquid interface inside this device can be curved to specific shapes in order to trap and manipulate floating particles.

4.3 Trapping

In order to manipulate floating particles, our capillary tweezers can create a trap in their center by orienting all DCAs radially. Indeed, in this configuration, setting all DCAs at the same capillary charge forms a valley or a hill at the center of the inner area as shown on the simulated profiles of Fig. 4.7. These profiles are computed from the theoretical expression of a dipolar capillary charge (Eq (4.1)) and the superposition principle. The black triangle indicates the location of the center of the trap. As explained in Chap. 1, using the Nicolson method [21], the energy of a particle on a fluid interface can be reduced to its gravitational energy. From Eq (1.23), this gives

$$E = -2\pi\gamma Q h(x, y) \tag{4.11}$$

A floating particle with a negative (positive) capillary charge will therefore decrease its energy by moving down (up) the interface, ending in the valley (hill) created inside the capillary tweezers.

The power of these capillary tweezers is that they only require that the particle has a capillary charge. There is no need for special properties such as magnetic or electric ones. We

performed trapping experiments for a glass bead of a 1 millimetre radius and an oil drop at an air-water interface. Both different particles were successfully trapped in the center of the capillary tweezers as shown on Fig. 4.8. Bubbles could also be trapped by creating a hill in the center of the capillary tweezers.
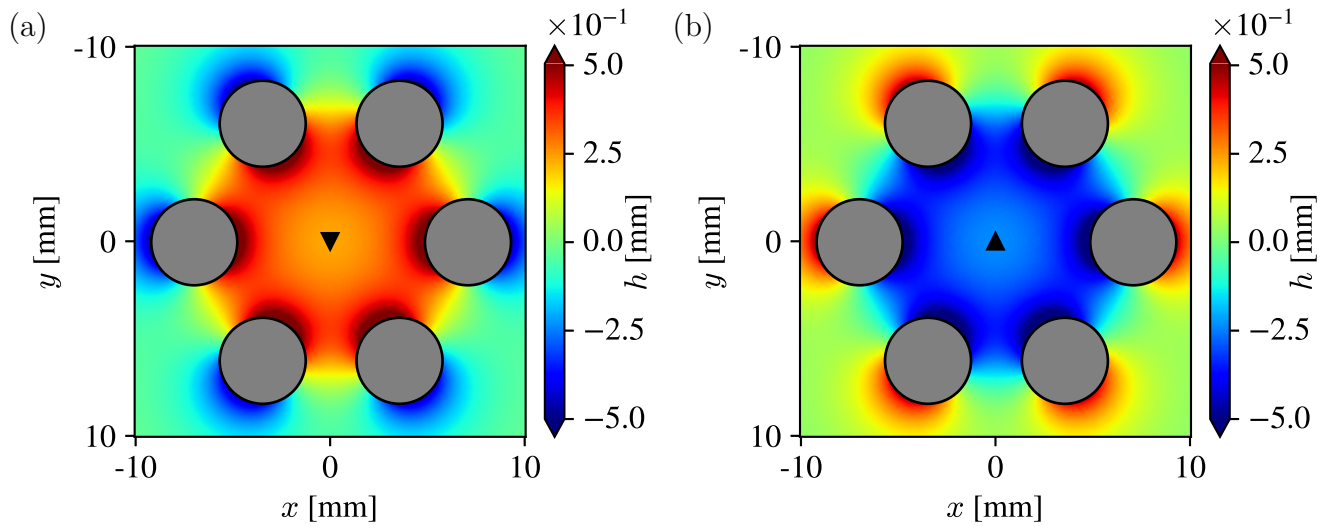
Fig. 4.7: Trap at the center of a ring made of six DCAs oriented radially. The DCAs have all the same capillary charge of 0.6 mm. The black triangle indicates the center of the trap. (a) Simulation of the surface topography when the positive poles of the DCAs are towards the center. A minimum is created inside the tweezers. (b) Simulation of the surface topography when the negative poles of the DCAs are towards the center. A maximum is created inside the tweezers.

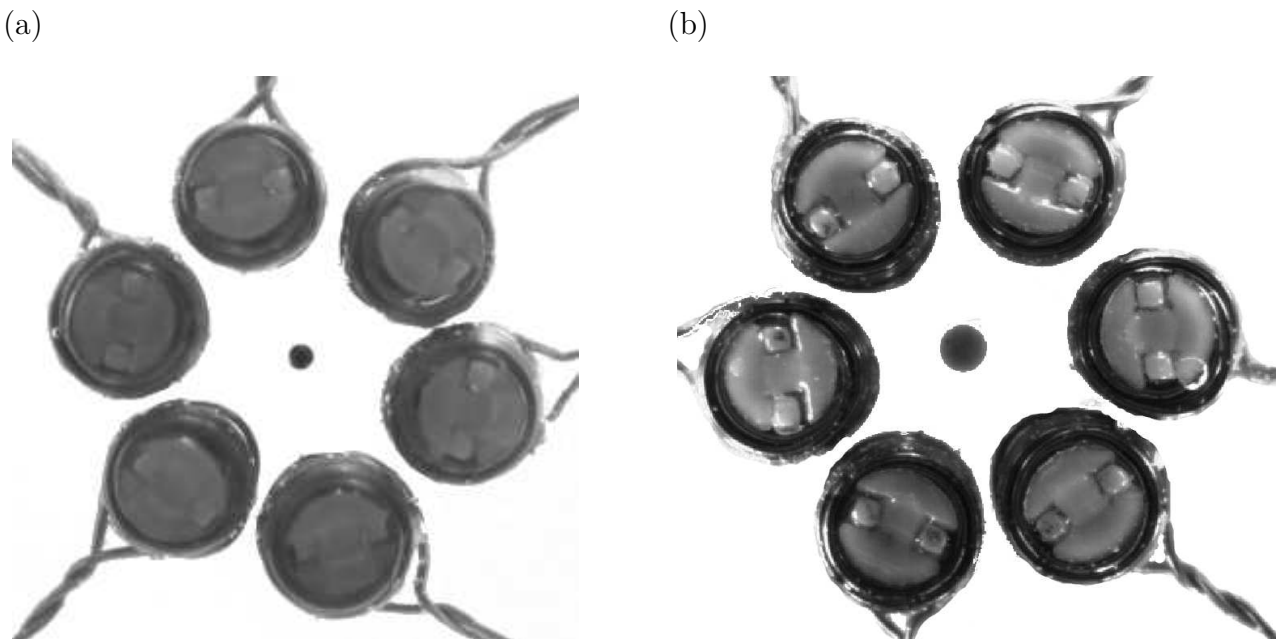**Fig. 4.8:** Trapping experiments of particles at the center of a ring made of six DCAs oriented radially towards the center of the ring. The DCAs have all the same capillary charge. (a) Glass bead of 1 millimetre radius at the surface of water . (b) Mineral oil drop at the surface of water. A blue dye is added to the oil to distinguish it from water.

The position of the trap, and therefore the position of the particle, is controlled by the charge ratio of the DCAs of the capillary tweezers. By changing the charge on one or several DCAs, the trap can be displaced from the center to any position inside the tweezers. This strategy allows us to move and position accurately the particle at a specific place. Fig. 4.9 shows simulated profiles of the liquid and the displacements of the trap when the capillary charges of some DCAs are increased.

We performed experiments to move and position a floating glass bead of 1 mm radius and a floating mineral oil drop using this strategy. The different steps of the displacement of the particles are shown on Figs. 4.10 and 4.11. We started by trapping the floating objects at the center of the capillary tweezers. Then, we increased the capillary charge of the DCAs one by one as in the simulations of Fig. 4.9. Both particles are successfully displaced, in a similar way to the trap of Fig. 4.9. These results demonstrate the ability of the capillary tweezers to manipulate various floating entities.
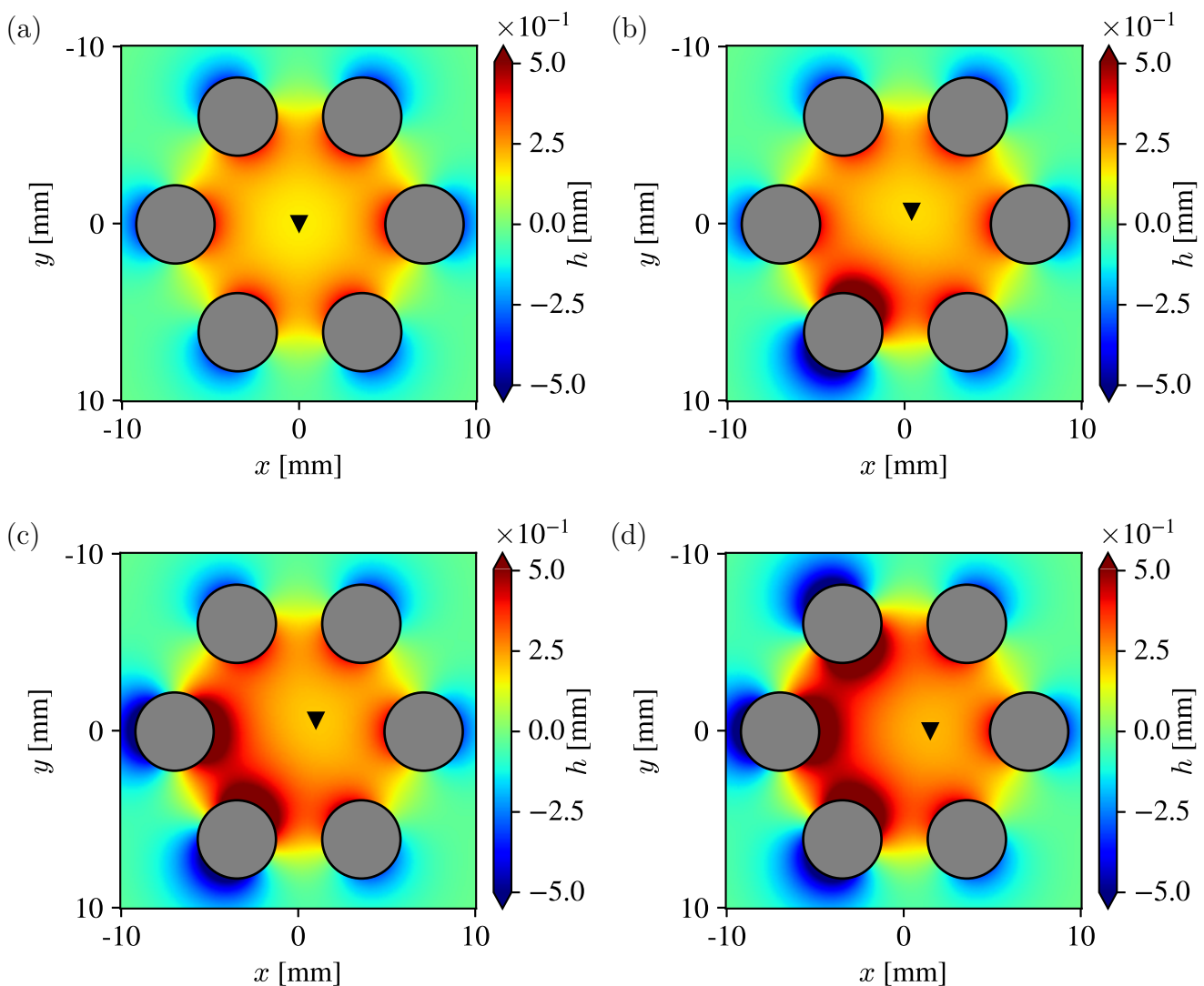
Fig. 4.9: The charge of each DCA of the capillary tweezers can be tuned individually to modify the position of the trap. This allows to displace a particle and position it accurately. Here are simulations of theoretical shapes of the interface when the charges of some DCAs are increased. The black triangle indicates the center of the trap. (a) All DCAs have the same capillary charge of 0.4 mm. (b) Five DCAs have a capillary charge of 0.4 mm and the last one has a charge of 0.8 mm. (c) Four DCAs have a capillary charge of 0.4 mm and two adjacent DCAs have a charge of 0.8 mm. (d) Three DCAs have a capillary charge of 0.4 mm and three adjacent DCAs have a charge of 0.8 mm.

The proposed capillary tweezers can found many applications in microfabrication and in microfluidics. For example, these tweezers could be used to displace floating droplets in a specific area where they would be analysed or to control the location where a self-assembly would take place. Morever, elaborated deformations of the interface presenting several valleys and/or hills could be obtained inside capillary tweezers. Such deformations would allow to manipulate components of different types simultaneously and to assemble heterogeneous structures.
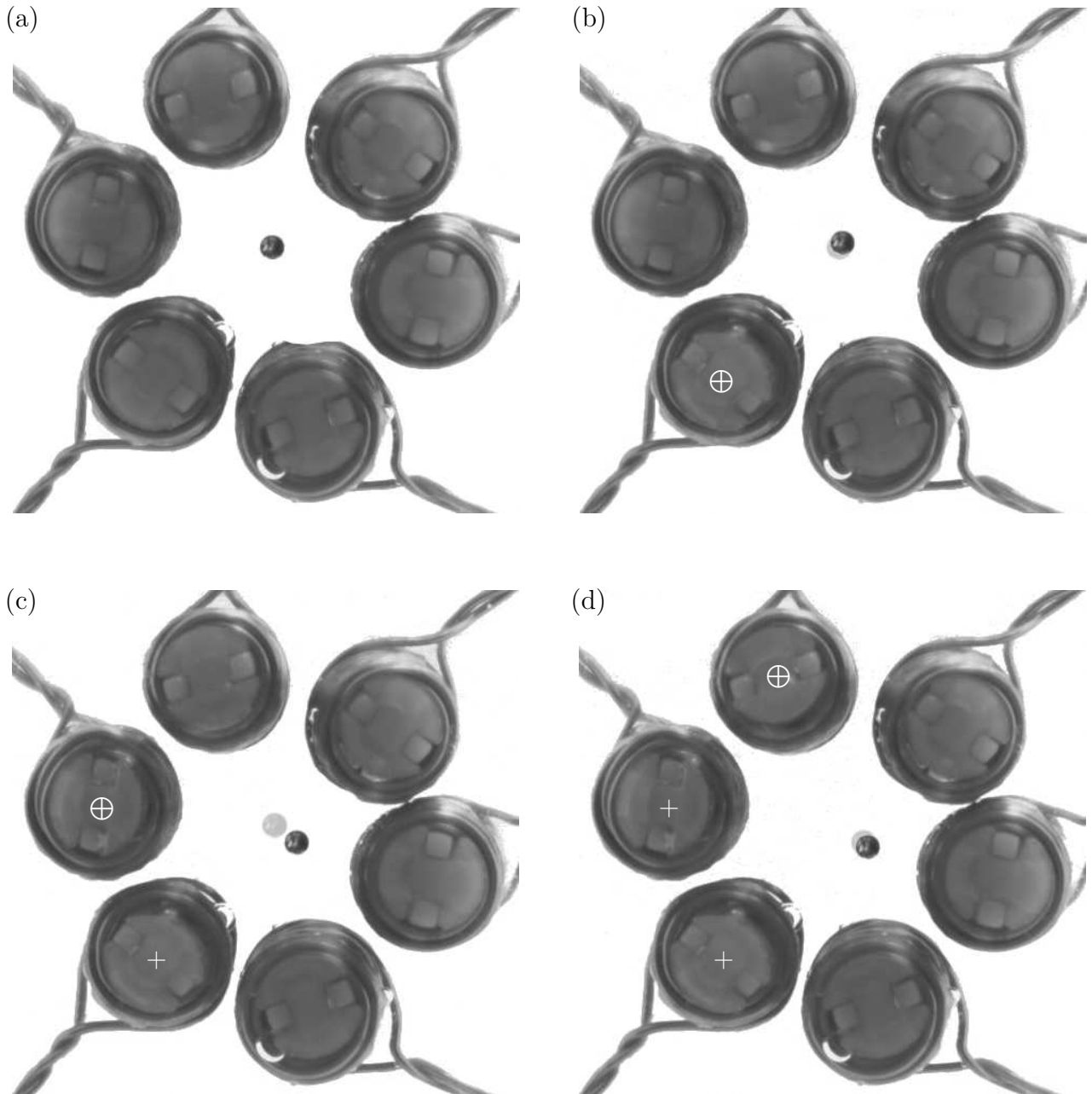
Fig. 4.10: Experiment of trapping and moving a glass bead of 1 mm radius floating at the surface of water. (a) At the beginning, all DCAs have similar capillary dipolar charges and the particle is trapped at the center of the capillary tweezers. (b)-(d) To change the position of the trap and displace the bead, the capillary charges of several DCAs are increased one by one. The light gray disk represents the position of the particle at the previous step. At each step, the DCA whose capillary charge is increased is marked by a white "⊕" symbol and the DCAs whose capillary charge was increased at the previous steps are marked by with "+" symbol.
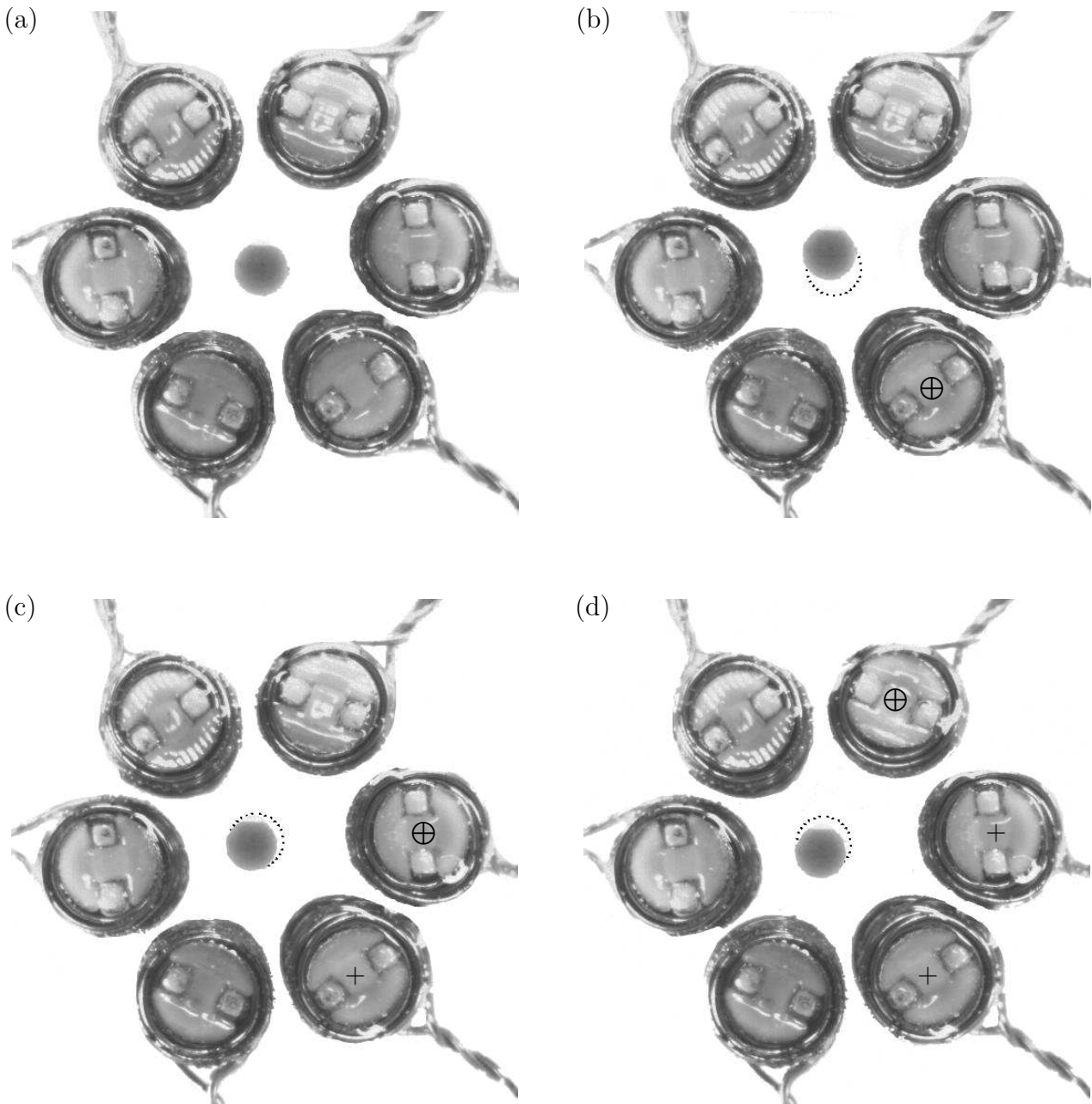
Fig. 4.11: Experiment of trapping and moving a mineral oil drop floating at the surface of water. A blue dye is added to the oil to distinguish it from water. (a) At the beginning, all DCAs have similar capillary dipolar charges and the particle is trapped at the center of the capillary tweezers. (b)-(d) To change the position of the trap and displace the drop, the capillary charges of several DCAs are increased one by one. The dashed circle represents the position of the particle at the previous step. At each step, the DCA whose capillary charge is increased is marked by a "$\oplus$" symbol and the DCAs whose capillary charge was increased at the previous steps are marked by with "$+$" symbol.

4.4 Transporting

In the previous section, we injected constant currents in the coils of the DCAs in order to apply constant magnetic fields around the floaters. These currents and fields were increased step by step to place the particle at a specific location. As in Chap. 3, we will now consider alternative currents, and therefore oscillating magnetic fields, in order to transport a floating object along the capillary tweezers.

With a sinusoidal field, the locomotion of a particle along the tweezers can be achieved by trapping it successively at each DCA as follows. On the first part of the oscillation, a DCA traps the object at its edge. On the second part of the oscillation, the sign of the field changes. The capillary charge of the DCA changes sign too and the particle is repelled. A neighbouring DCA with an inclination opposite to that of the first DCA captures the object.

The first thing that this strategy requires is that adjacent DCAs are in phase opposition so that their capillary charges are opposed. To achieve this, 180° out of phase currents are injected in adjacent DCAs. In this configuration, local minima and maxima are created in alternation along the ring formed by the capillary tweezers as illustrated on the simulations of Fig. 4.12. Whatever the floating particle, three DCAs are therefore traps and the other three repel it. When the sign of the current in the coils changes, the magnetic field surrounding the magnet of the floater reverses and the charges of the DCAs change sign (Fig. 4.12 (b)). The particle is repelled by the DCA that previously trapped it. In order to decrease its energy, as seen in Chap. 1, the floating object moves along the interface towards an adjacent DCA which becomes a trap. Setting adjacent DCAs in phase opposition thus allows to move the particle from one DCA to another.
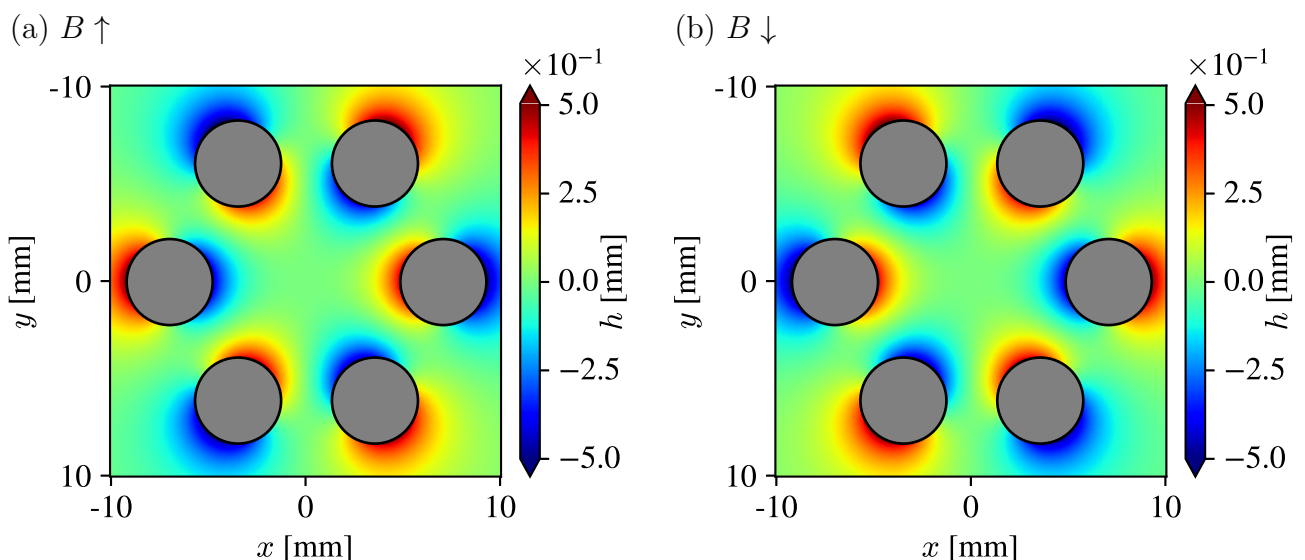

(a) $B \uparrow$ (b) $B \downarrow$

Fig. 4.12: Simulated profiles of the interface in the capillary tweezers when adjacent DCAs are in phase opposition. Local minima and maxima are created in alternation along the ring formed by the capillary tweezers. The module of the charges is 0.6 mm.

However, this is not enough to obtain a net transport of an object along the capillary tweezers. Indeed, when a particle is repelled by a DCA, it can be trapped by the left or right neighbouring DCA with the same probability. There is no preferential direction. Let us consider a heavy particle. As seen in Chap. 1, such particle goes down the interface and is trapped by a local minimum at the edge of a DCA. Because of the symmetry of the capillary tweezers, this local minimum is in the radial direction as illustrated on Fig. 4.12. When the charge of the DCA changes, the local minimum becomes a local maximum and the particle is repelled. Fig. 4.13 shows the opposite gradient of the height of a simulated interface. The slopes of the interface being symmetrical with respect to the radial direction, the object can fall down the surface either to the DCA on its left or to the one on its right, depending on the small perturbations that it will experience. The absence of directed motion can also be highlighted by considering the potential along the trajectory of the particle. Using the Nicolson approximation [21] explained in Chap. 1, the energy of the floating object reduces to its gravitational potential energy $U_g = mgh$, where m is the mass of the particle and g is

the gravitational acceleration. As m and g are constant, the potential has the shape of h and is symmetrical along the trajectory of the particle. This prevents a net motion of the floating object.
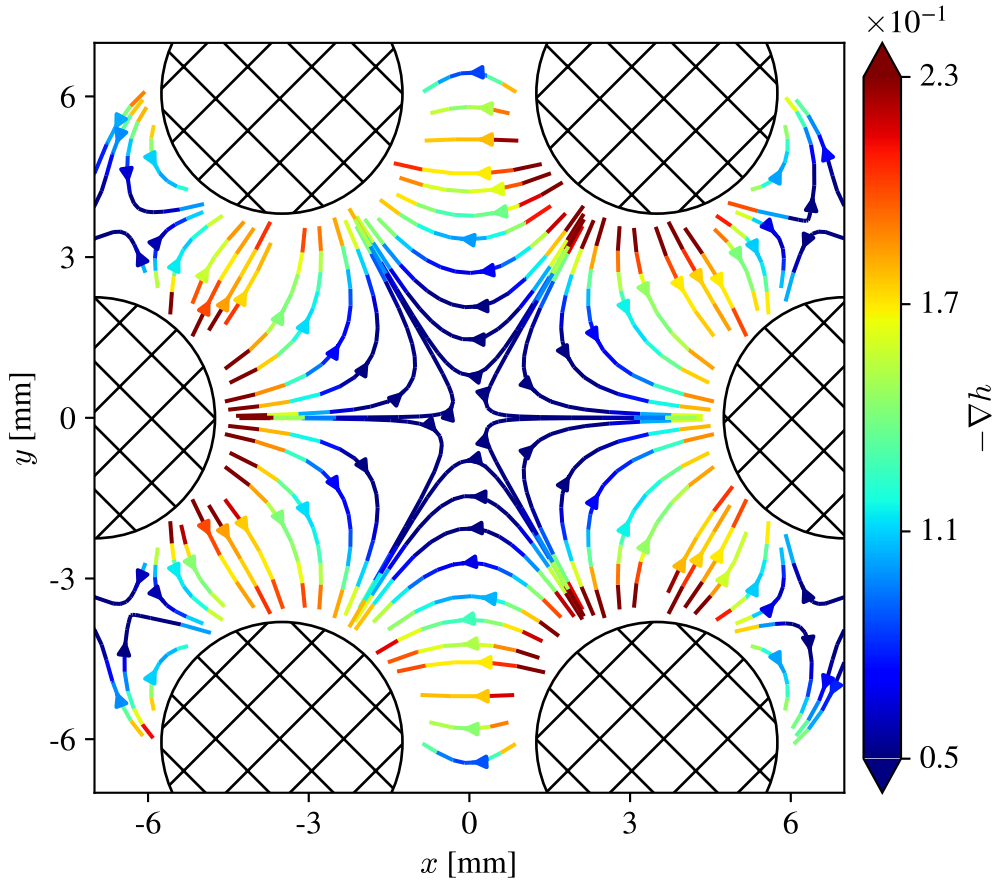

Fig. 4.13: Simulation of capillary tweezers with adjacent DCAs in phase opposition. All DCAs are oriented radially. Streamlines represent the opposite gradient of height of the interface computed from the superposition of six dipolar capillary charges. The slopes of the interface being symmetrical with respect to the radial direction, a particle repelled by a DCA can be trapped by the left or right neighbouring DCA with the same probability. The module of the charges is $0.6\,\mathrm{mm}$.

A net transport of a particle requires that the potential along its trajectory is asymmetrical. In order to achieve this, the orientation of the DCAs is tilted from the radial direction. We chose to turn them by 45° which is the intermediate orientation between the extreme radial and tangential positions. Fig. 4.14 shows simulations of the profile of the interface in the capillary tweezers in this configuration.

In order to check that tilting the DCAs breaks the symmetry of the potential, we performed transport experiments with a floating glass bead of $1\,\mathrm{mm}$ radius. When the DCAs are oriented as in Fig. 4.14, the bead moves clockwise along the tweezers. Fig. 4.15 shows the opposite gradient of the height of a simulated interface and the trajectory of the particle. The hashed circles are the DCAs. The positions of the bead are the filled circles and come from experiments. The current position of the particle is in black and past positions are in gray. When the bead leaves a DCA, we can observe that the profile of the interface is no more symmetrical with respect to the radial direction because of the orientation of the DCAs and the resulting positions of local minima (see Fig. 4.14). By moving to the left, the particle follows the slopes of the interface. Considering the Nicolson approximation [21], we can define

an effective potential in which the bead evolves as

$$U_{\text{eff}} = \frac{U_g}{mg} = h \tag{4.12}$$

This effective potential is just the gravitational potential energy divided by the constant mg. From the simulated profiles of the interface and the experimental positions of the bead, the effective potential along the trajectory of the particle can be computed. It is shown on Fig. 4.16. We can see that this potential is asymmetric. This ensures a net motion of the particle.

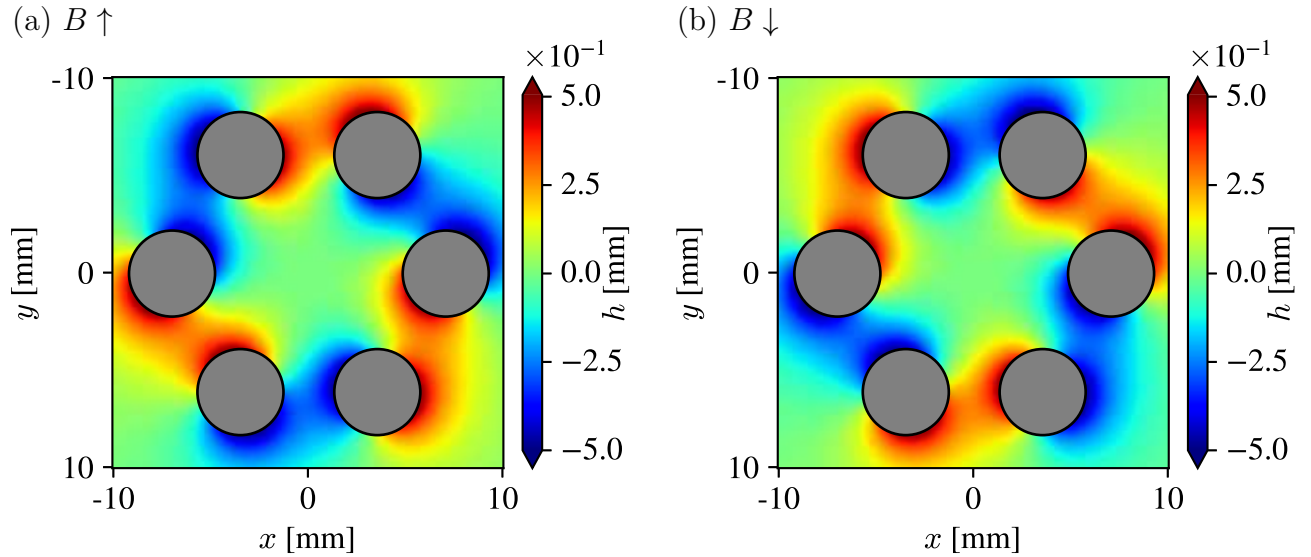(a) $B \uparrow$ (b) $B \downarrow$

Fig. 4.14: Simulated profiles of the interface in the capillary tweezers when adjacent DCAs are in phase opposition and tilted by an angle of 45° from the radial direction. Local minima and maxima are created in alternation along the ring formed by the capillary tweezers. The module of the charges is 0.6 mm.
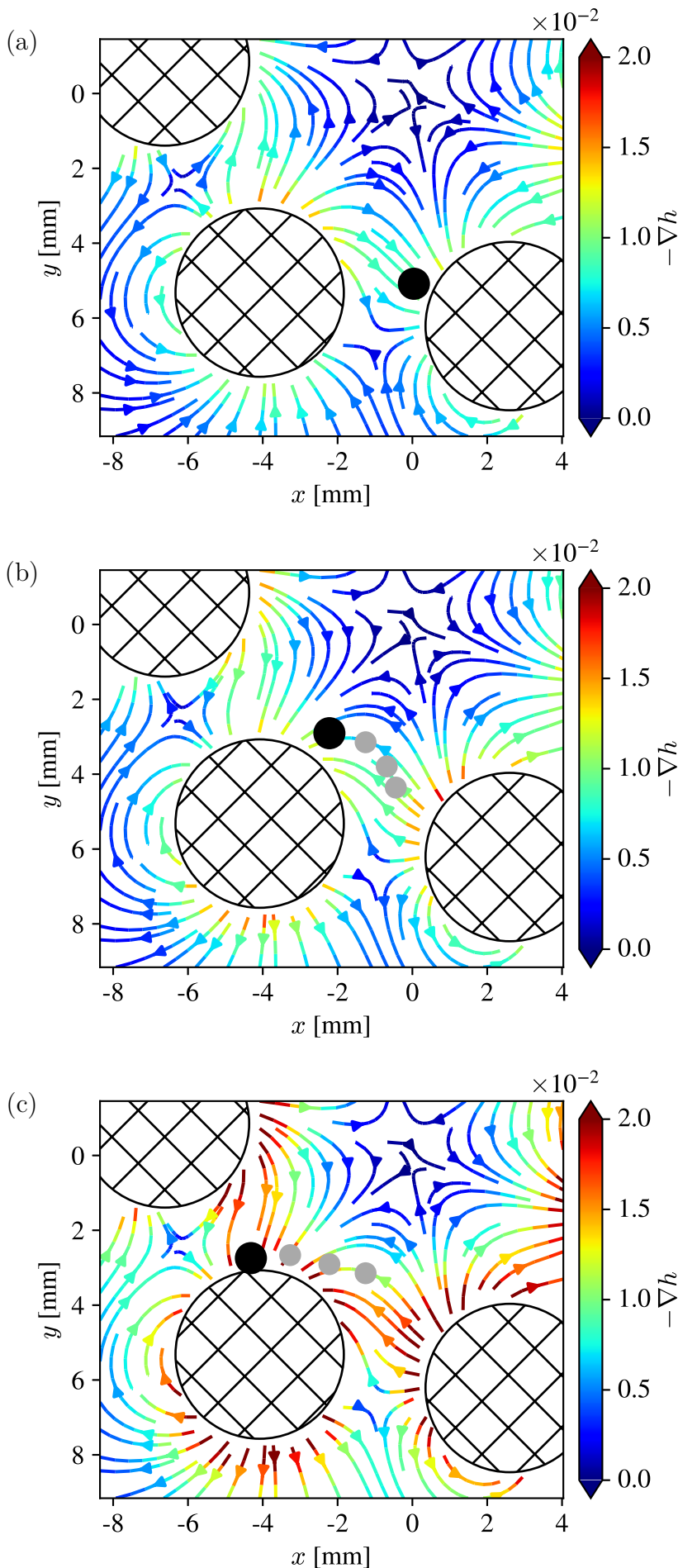
Fig. 4.15: Transport of a floating glass bead of 1 mm by our capillary tweezers. The DCAs (hashed circles) are tilted from the radial direction by an angle of 45° as in Fig. 4.14. A sinusoidal current is injected into each coil. Two adjacent DCAs are in phase opposition and have opposite charges. The positions of the glass bead are marked by filled circles and come from experiments. Its current position is in black and past positions are in gray. On the background, streamlines represent the opposite gradient of height of the simulated interface computed from the superposition of six dipolar capillary charges. (a) At the start, the bead is captured at the local minimum of a DCA. (b) The DCAs change their inclination and the trapping DCA in (a) becomes repulsive. The particle follows the streamlines and goes to the left DCA. (c)The glass bead falls in the local minimum of the new trapping DCA.

Fig. 4.16: Motion of a floating glass bead of 1 mm in the capillary tweezers. Adjacent DCAs are in phase opposition so that their capillary charges are opposed. Tilting the DCAs from the radial direction by an angle of 45° breaks the symmetry of the potential. This results in a net transport of the particle. (a) Trajectory of the glass bead. The DCAs are represented by gray disks. The positions of the particle correspond to the black circles. (b) Effective potential along the trajectory.
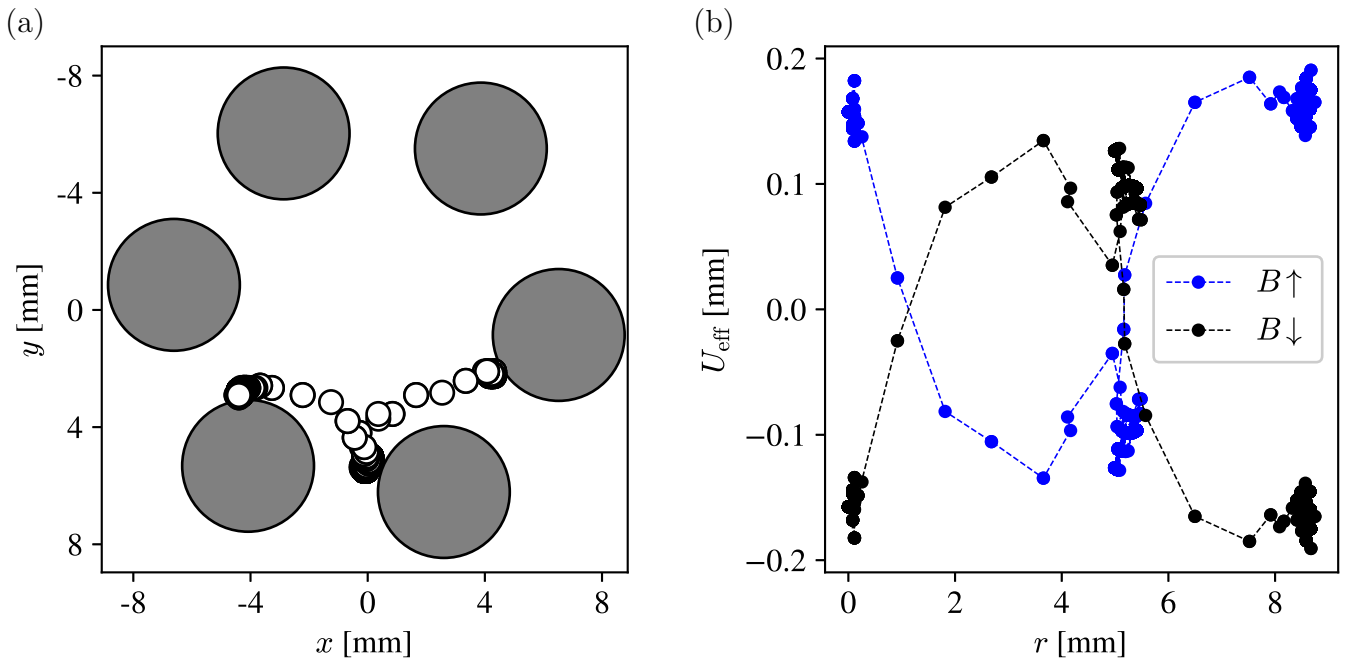
These results show that changing the configuration of the DCAs in the capillary tweezers allows to perform new operations. By setting adjacent DCAs in phase opposition and tilting them, we are able to move an object along the capillary tweezers as long as we want. These tweezers could therefore be used to transport floating particles over large distances. Moreover, as several local minima and maxima are created, multiple particles can be trapped at different locations and then be moved simultaneously. The nature (heavy or light) of the trapped entities can be different. Heavy ones will be captured by local minima and light ones by local maxima. The asymmetry of the potential guarantees that all the particles are displaced in the same direction, no matter their nature. Fig. 4.17 shows the simultaneous transport of a single bead and a dimer composed of two beads. The beads of the dimer stick together only by a capillary bridge.
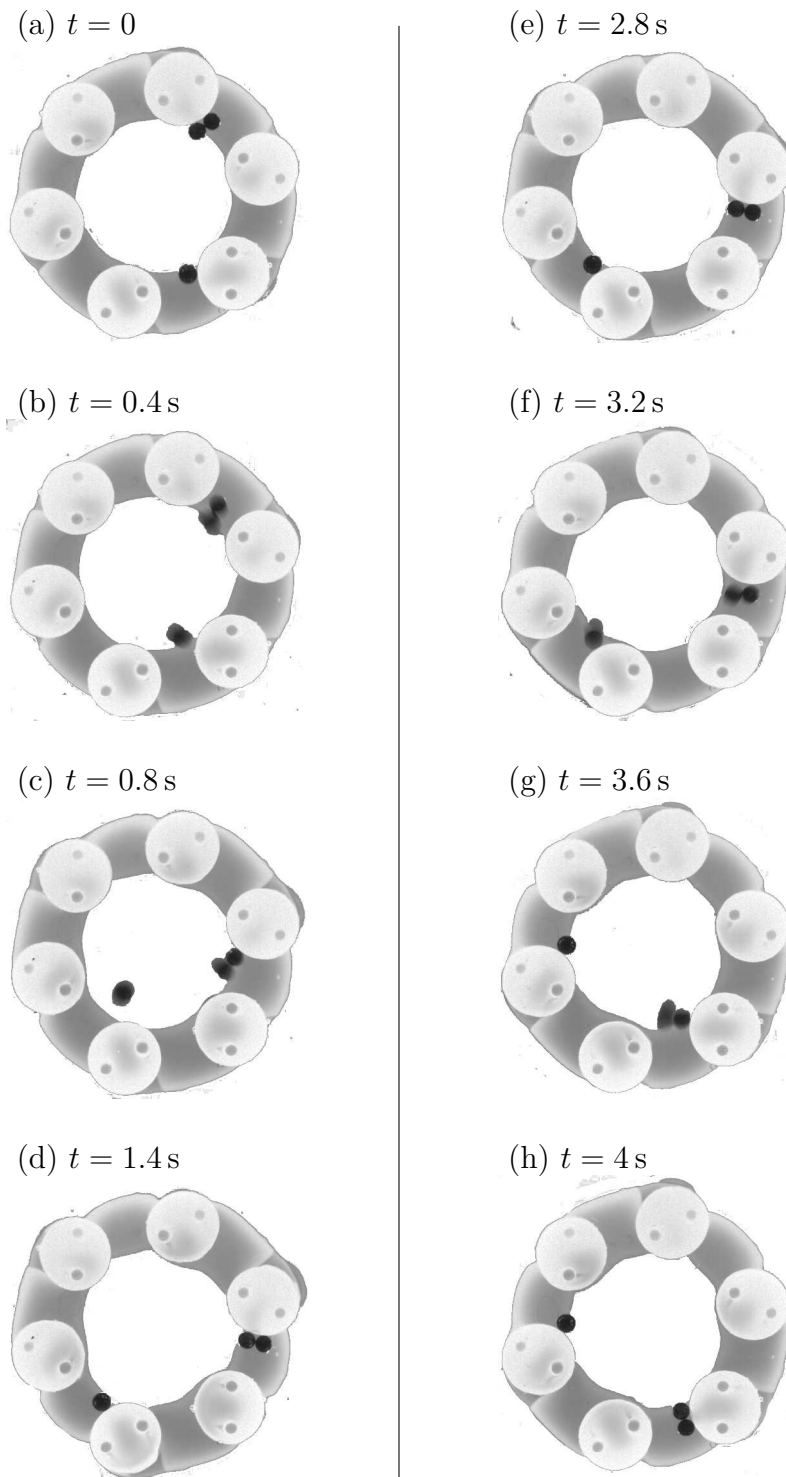
Fig. 4.17: A single glass bead of 1 mm and a dimer are transported simultaneously by the capillary tweezers. The dimer is composed of two glass beads of 1 mm that stick together only by a capillary bridge. The DCAs are tilted from the radial direction by an angle of 45° and a sinusoidal current is injected into each coil. Two adjacent DCAs are 180° out of phase and have opposite charges. The transport speed is fixed by the frequency of the electric current. In this experiment, the frequency is set to 0.2 Hz.

4.5 Summary

The first strategy proposed in Chap. 3 requires to modify the geometry of the floating objects, which is not always possible. In order to overcome this limitation and to be able to handle a single particle, we developed a second strategy based on a global deformation of the interface in a specific area.

This chapter showed how we built an actuator, the Dipolar Capillary Actuator, that is able to produce a controllable dipolar capillary charge. Multiple actuators can be placed along a ring to form capillary tweezers. Depending on the orientations of the DCAs, the surface of the liquid inside the tweezers can be deformed to create a global minimum (maximum) or several local minima (maxima). Heavy (light) objects will fall into a minimum (maximum) and controlling the position of this minimum (maximum) allows to move a particle. This technique of manipulation can be used with any type of floating objects. We demonstrated that a floating droplet can be positioned as easily as a hard bead.

We also showed that the configuration of the DCAs can be modified in order to transport particles along the capillary tweezers. First, we injected alternative currents in phase opposition in adjacent DCAs, so that their capillary charges are opposite. Then, we tilted the orientation of each DCA from the radial direction by an angle of 45°. With this configuration, local minima and maxima are created in alternation along the ring formed by the capillary tweezers. A heavy (light) particle placed in our capillary tweezers will be captured at one of the three minima (maxima). When the alternative current inverts, the DCAs change sign and the particle is repelled. It moves along the interface to the new minima (maxima) created at the next DCA. We showed that the orientation of the DCAs at 45° from the radial direction breaks the potential in which the particles evolves. This ensures that the particle goes always in the same direction. A net transport is therefore obtained.

5 General conclusion and perspectives

5.1 Conclusion

In this thesis, we are focusing on the capillary forces experienced by mesoscopic floating objects. By deforming the liquid interface into specific shapes, we exploit these forces in order to assemble and manipulate components. For this purpose, we developed two complementary strategies: modify the particle shape or change the menisci at the interface.

Chap. 1 introduced surface tension and presented specific resulting phenomena. We showed that deforming a liquid interface induces capillary forces that come from surface tension. When multiple particles float at a liquid surface, they experience interactions that can lead to their assembly. We gave the liquid profile around a single spherical object and derived the expression of the force between two floating spheres. We explained how aggregates can be formed with basic particles and presented some methods to build floating objects that self-assemble into elaborated structures. The proposed examples illustrated how powerful capillary self-assembly can be in creating structures. They also showed that (almost) all floating components considered so far were passive and formed static assemblies. Starting from these examples and the state of art in capillary interactions, we can imagine new active components and new strategies to manipulate floating objects.

Chap. 2 was dedicated to the imaging of the topography of a fluid interface. As capillary forces come from the deformations of the liquid surface, a reliable and efficient method to measure them was required. We cited different techniques and chose to focus on Background Oriented Schlieren method. We presented different implementations of the BOS technique with their advantages and limitations. The main drawback of these implementations is that they are limited to weak deformations of the interface. In order to be able to measure higher deformations of the surface, we proposed a new method based on an enhanced optical setup. With the techniques described in Chap. 2, we were able to evaluate the liquid profile and the capillary interactions between the floating objects considered in the rest of this thesis.

Chap. 3 presented the first strategy we developed to manipulate and assemble floating mesoscopic particles. It consists in making controllable components that create specific deformations of the interface in their neighbourhood. We explained how we fabricated soft cross-shaped objects and how we actuated them by inserting small neodymium magnets in their branches. We showed that a vertical magnetic field can be used to control the deformation of the surface caused by the objects and therefore their capillary interactions. We successfully formed a reversible self-assembly that is able to switch between two structures. In addition to constant magnetic fields, oscillating fields have also been applied to the controllable

components. These components generate capillary waves when the frequency of the field is greater than a threshold value. Our floating objects can exploit these waves to perform some motion. We showed that they can be transformed in spinners by adding some asymmetry between the left and right sides of their branches. These spinners form a reversible rotating self-assembly when an oscillating component is added to a constant vertical magnetic field.

Chap. 4 proposed another strategy to manipulate floating particles. Rather than deforming locally the interface with controllable floating components, the surface is shaped globally in a specific area by actuators. We presented the Dipolar Capillary Actuator that is able to create a controllable dipolar capillary charge. Then, we showed how multiple actuators can be placed along a ring to form capillary tweezers. The interface inside the tweezers can be deformed to position and displace floating particles whatever their nature. We demonstrated that a floating droplet can be positioned as easily as a hard bead. We also showed that the configuration of the DCAs can be modified in order to transport particles along the capillary tweezers.

5.2   Perspectives

This thesis provides promising results that can found many applications in microrobotics and microfuildics. The proposed controllable components can lead to the creation of functional structures that are able to change their behaviour. They can also be used to developed new types of self-assembled robots. Our capillary tweezers can manipulate various particles and could be used to assemble heterogeneous components. They could also transport chemicals to a specific area where they would be mixed or analysed. However, there are still many other possibilities to exploit capillary forces to manipulate and assemble objects. A single thesis cannot claim to cover the whole subject. This work paves the way to further research.

When we created controllable floating components, we had to choose a shape. Many other designs can be imagined. Keeping cross-shaped objects, the branch length ratio and/or the number of branches can be changed. Other structures could be formed in this way. For example, as shown in Sec. 1.6.2, Poty et al. [51] obtained a triangular pattern by self-assembling cross-shaped components whose branch length ratio is $\sqrt{3}$. We also considered a single orientation of the magnets in the branches. Placing magnets with different orientations will result in a combination of attractive and repulsive forces between adjacent objects that may lead to the self-assembly of open structures.

Other studies can focus on the behaviour of our controllable spinners in an oscillating magnetic field. Indeed, the evolution of their rotation speed as a function of the frequency of the field is not obvious as shown on Fig. 5.1. Peaks can be observed. They may result from mechanical resonant frequencies. The interaction between counter-clockwise and clockwise spinners is another topic that can be explored. We observed that a mixture of both spinners phase separates when an oscillating magnetic field is applied. This is illustrated in Fig. 5.2.

It would also be interesting to design other spinners from our controllable components and compare them. This only requires that the branches of the components are asymmetrical. For example, another spinner can be created by increasing the bevel on one side of the branches of the controllable component as illustrated on Fig. 5.3. As the spinners proposed in Sec. 3.3, these objects mainly rotate towards the heaviest half of the branch. However, in a small frequency range, their direction of rotation is reversed as shown on Fig. 5.4. Such spinners deserve more attention as they allow new possibilities of motion. If we could exploit gravity waves to obtain a straight-line movement, they would be able to perform a complete motion remotely controlled by the frequency of the magnetic field.
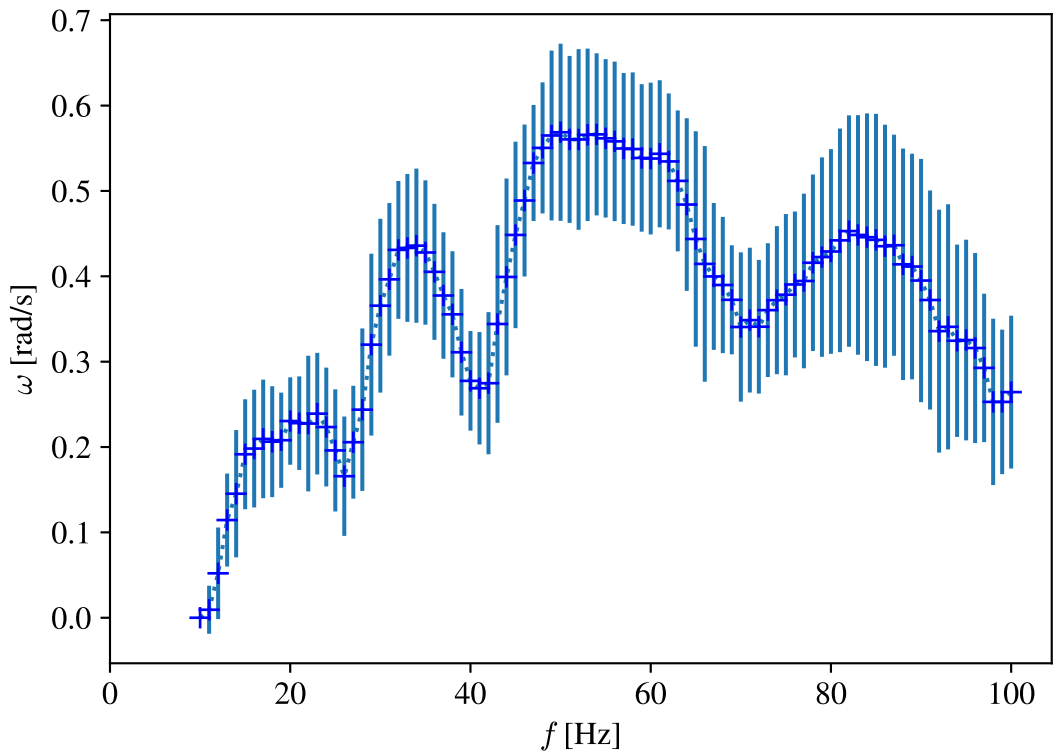
Fig. 5.1: Rotation speed ω of the controllable spinners as a function of the frequency f of the oscillating magnetic field. The spinners float at the surface of water. The magnetic field has an amplitude of $21\,\mathrm{G}$.

(a) $t = 0$ (b) $t = 15\,\mathrm{min}$ (c) $t = 30\,\mathrm{min}$

Fig. 5.2: Phase separation of a mixture of 8 counter-clockwise and 8 clockwise spinners in a circular container. The counter-clockwise spinners are coloured in green and the clockwise spinners are coloured in red.
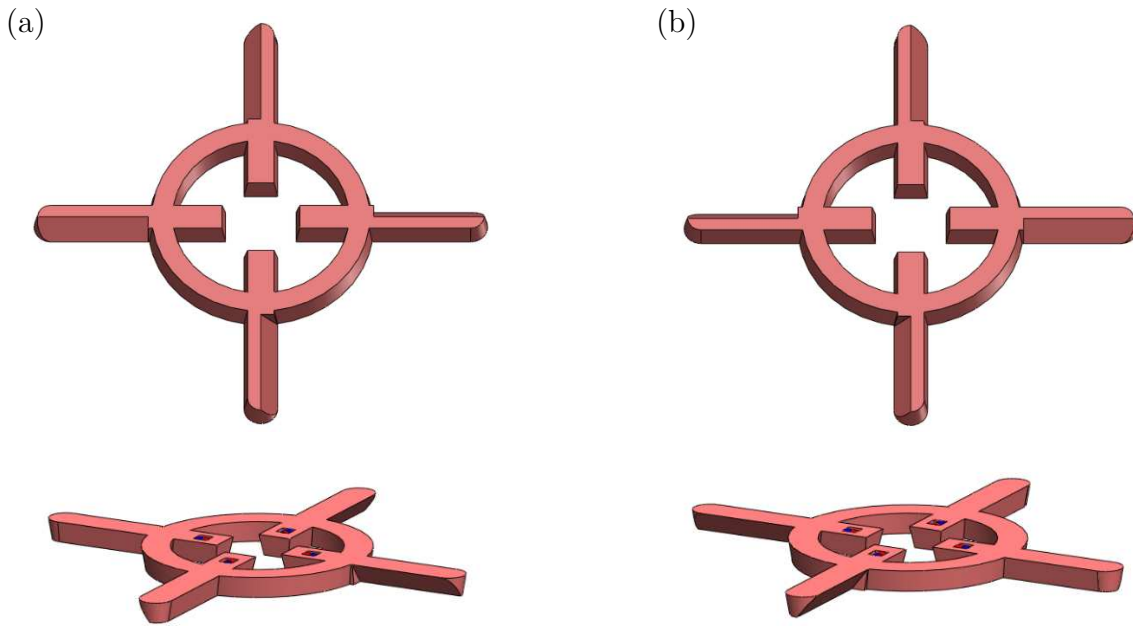
Fig. 5.3: Controllable spinners obtained by increasing the bevel on one side of the branches of the controllable component of Fig. 3.8. (a) Bevel increased on the right side of the branches. This spinner mainly rotates counter-clockwise in an oscillating magnetic field. (b) Bevel increased on the left side of the branches. This spinner mainly rotates clockwise in an oscillating magnetic field.
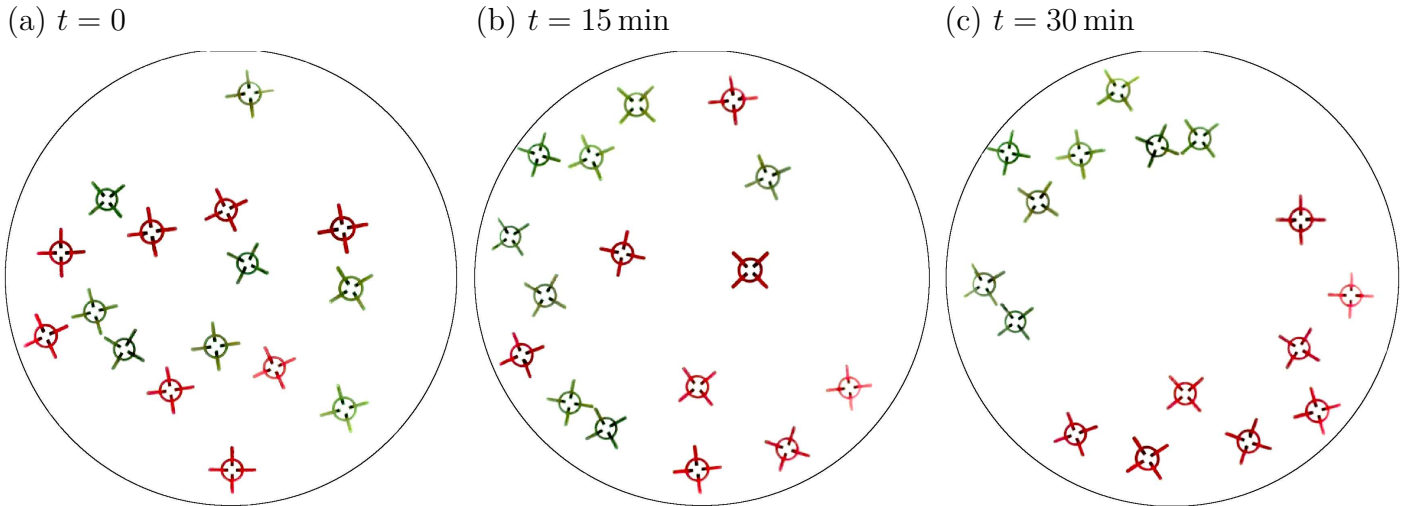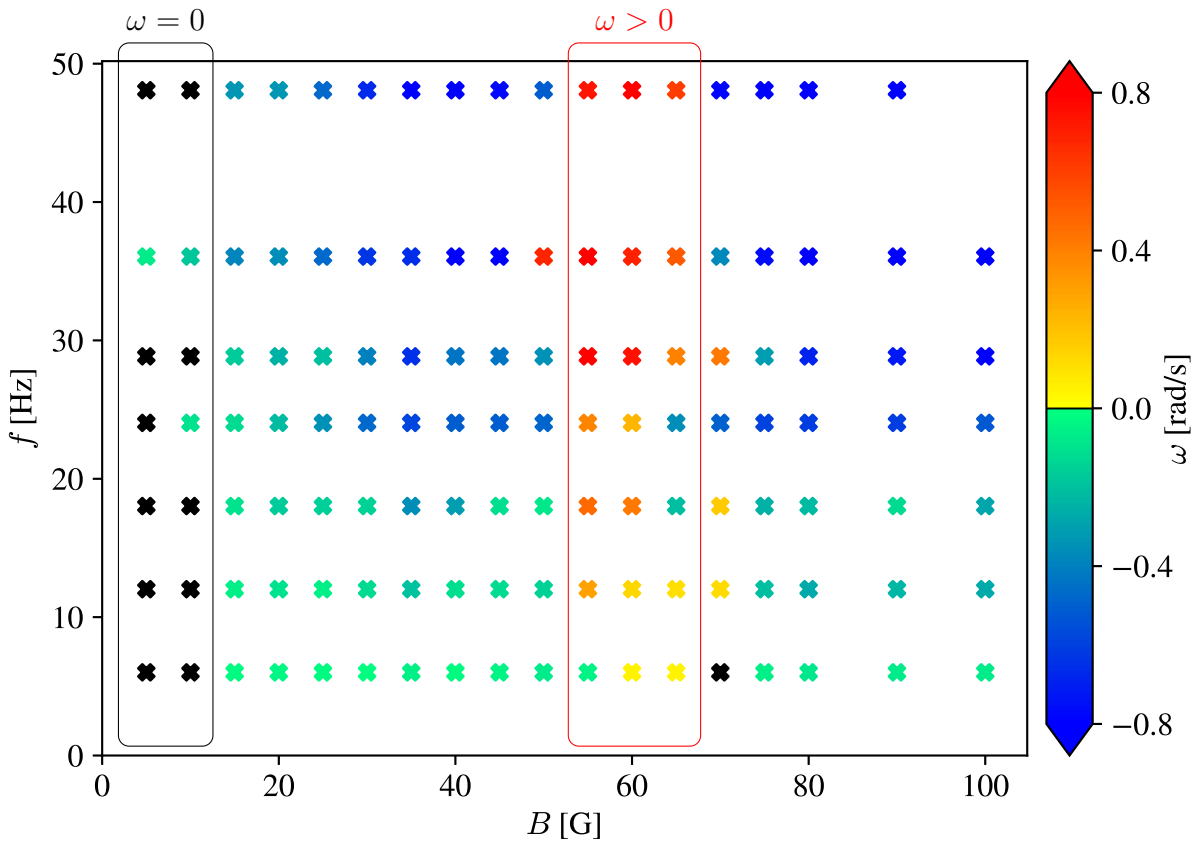

Fig. 5.4: Phase diagram of the rotation of a spinner created by increasing the bevel on the right side of the controllable component as in Fig. 5.3 (a). Beyond a threshold frequency, the spinner emits capillary waves and starts to rotate. It mainly rotates counter-clockwise ($\omega < 0$), towards the heaviest half of its branches as the counter-clockwise spinner of Fig. 3.11 (b). However, in a small frequency range, its rotation reverses and it turns clockwise.

The capillary tweezers proposed in this thesis could be the starting point for further research. We explored some configurations of the DCAs along the tweezers but many others can be imagined. Numerical simulation is an easy way to test configurations that could be realized experimentally. For example, the simulated profiles of Fig. 5.5 show the creation of two minima in the capillary tweezers. The distance between these minima can be changed by tuning the charges of the DCAs. In this way, it would be possible to assemble and separate particles that have weak interactions.
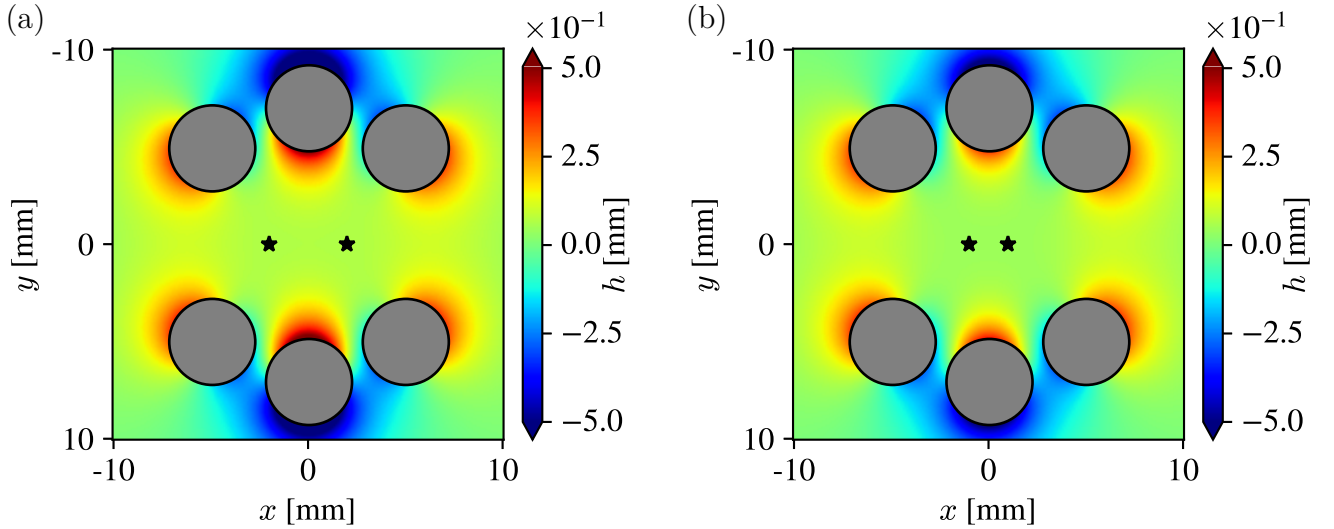
Fig. 5.5: Examples of a configuration of the DCAs that creates two local minima in the capillary tweezers. Simulated profiles. The local minima are indicated by a black cross. In (b), the capillary charges of the DCAs at 90° and 270° on the circular tweezers are reduced by 25% compared to (a). This brings the local minima closer together.

The capillary tweezers could also be used to manipulate new particles. We tried to perform experiments with soapy water in order to manipulate bubbles. However, the floaters of the DCAs rely on surface tension to float because of the weight of the magnets. Soap decreasing surface tension, they tend to sink. This could be solved by improving the design of the DCAs to decrease their weight. Another actuation mechanism could also be considered.

References

[1] P. Polimeno, A. Magazzu, M. A. Iati, F. Patti, R. Saija, C. D. E. Boschi, M. G. Donato, P. G. Gucciardi, P. H. Jones, G. Volpe, and O. M. Maragò. Optical tweezers and their applications. *J. Quant. Spectrosc. Radiat. Transf.*, **218**, 131 (2018).

[2] J. R. Moffitt, Y. R. Chemla, S. B. Smith, and C. Bustamante. Recent advances in optical tweezers. *Annu. Rev. Biochem.*, **77**, 205 (2008).

[3] H. Zhang and K.-K. Liu. Optical tweezers for single cells. *J. R. Soc. Interface*, **5**, 671 (2008).

[4] J. Millen. (UCL Physics & Astronomy). *flickr* (2015). `https://www.flickr.com/photos/uclmaps/16841346482/`. CC BY 2.0 license.

[5] NASA. *flickr* (2016). `https://www.flickr.com/photos/nasa2explore/31530257961/`. CC BY 2.0 license.

[6] G. M. Whitesides, J. P. Mathias, and C. T. Seto. Molecular self-assembly and nanochemistry: a chemical strategy for the synthesis of nanostructures. *Science*, **254**, 1312 (1991).

[7] S. Zhang. Fabrication of novel biomaterials through molecular self-assembly. *Nat. Biotechnol.*, **21**, 1171 (2003).

[8] A. Wang, J. Huang, and Y. Yan. Hierarchical molecular self-assemblies: construction and advantages. *Soft Matter*, **10**, 3362 (2014).

[9] C. J. Morris, S. A. Stauth, and B. A. Parviz. Self-assembly for microscale and nanoscale packaging: Steps toward self-packaging. *IEEE Trans. Adv. Packaging*, **28**, 600 (2005).

[10] M. Mastrangeli, S. Abbasi, C. Varel, C. Van Hoof, J.-P. Celis, and K. F. Böhringer. Self-assembly from milli-to nanoscales: methods and applications. *J. Micromech. Microeng.*, **19**, 083001 (2009).

[11] G. M. Whitesides and B. Grzybowski. Self-Assembly at All Scales. *Science*, **295**, 2418 (2002).

[12] M. Boncheva and G. M. Whitesides. Making things by self-assembly. *MRS bull.*, **30**, 736 (2005).

[13] A. S. Iyer and K. Paul. Self-assembly: a review of scope and applications. *IET Nanobiotechnol.*, **9**, 122 (2015).

[14] P. G. de Gennes, F. Brochard-Wyart, and D. Quéré. *Gouttes, bulles, perles et ondes.* Belin (Collection Échelles), Paris (2002).

[15] D. L. Hu, B. Brian Chan, and J. W. M. Bush. The hydrodynamics of water strider locomotion. *Nature*, **424**, 663 (2003).

[16] M. W. Denny. Paradox lost: answers and questions about walking on water. *J. Exp. Biol.*, **207**, 1601 (2004).

[17] D. L. Hu and J. W. M. Bush. Meniscus-climbing insects. *Nature*, **437**, 733 (2005).

[18] A. Marchand, J. H. Weijs, J. H. Snoeijer, and B. Andreotti. Why is surface tension a force parallel to the interface? *Am. J. Phys.*, **79**, 999 (2011).

[19] M. V. Berry. The molecular mechanism of surface tension. *Phys. Educ.*, **6**, 79 (1971).

[20] D. Vella and L. Mahadevan. The "Cheerios effect". *Am. J. Phys.*, **73**, 817 (2005).

[21] M. M. Nicolson. The interaction between floating particles. *Proc. Cambr. Phil. Soc.*, **45**, 288 (1949).

[22] D. Y. C. Chan, Henry, JD Jr, and L. R. White. The interaction of colloidal particles collected at fluid interfaces. *J. Colloid Interface Sci.*, **79**, 410 (1981).

[23] C. Allain and M. Cloitre. Interaction between particles trapped at fluid interfaces: I. Exact and asymptotic solutions for the force between two horizontal cylinders and II. Free-energy analysis of the interaction between two horizontal cylinders. *J. Colloid Interface Sci.*, **157**, 261 and 269 (1993).

[24] P. A. Kralchevsky and N. D. Denkov. Capillary forces and structuring in layers of colloid particles. *Curr. Opin. Colloid Interface Sci.*, **6**, 383 (2001).

[25] M. Poty and N. Vandewalle. Equilibrium distances for the capillary interaction between floating objects. *Soft Matter*, **17**, 6718 (2021).

[26] M. Abramowitz and I. A. Stegun. *Handbook of mathematical functions.* Dover, New York (1965).

[27] D. Stamou, C. Duschl, and D. Johannsmann. Long-range attraction between colloidal spheres at the air-water interface: The consequence of an irregular meniscus. *Phys. Rev. E*, **62**, 5263 (2000).

[28] E. A. van Nierop, M. A. Stijnman, and S. Hilgenfeldt. Shape-induced capillary interactions of colloidal particles. *EPL*, **72**, 671 (2005).

[29] J. C. Loudet, A. M. Alsayed, J. Zhan, and Yodh A. G. Capillary Interactions Between Anisotropic Colloidal Particles. *Phys. Rev. Lett.*, **94**, 01830 (2005).

[30] L. Botto, E. P. Lewandowski, M. Jr. Cavallaro, and Stebe K. J. Capillary interactions between anisotropic particles. *Soft Matter*, **8**, 9957 (2012).

[31] J. C. Loudet and B. Pouligny. How do mosquito eggs self-assemble on the water surface? *Eur. Phys. J. E* , **34**, 1 (2011).

[32] K. D. Danov, P. A. Kralchevsky, B. N. Naydenov, and G. Brenn. Interactions between particles with an úndulated contact line at a fluid interface: Capillary multipoles of arbitrary order. *J. Colloid Interface Sci.*, **287**, 121 (2005).

[33] K. D. Danov and P. A. Kralchevsky. Capillary forces between particles at a liquid interface: General theoretical approach and interactions between capillary multipoles. *Adv. in Colloid Interface Sci.*, **154**, 91 (2010).

[34] P. A. Kralchevsky, V. N. Paunov, N. D. Denkov, I. B. Ivanov, and K. Nagayama. Energetical and force approaches to the capillary interactions between particles attached to a liquid-fluid interface. *J. Colloid Interface Sci.*, **155**, 420 (1993).

[35] G. A. Korn and T. M. Korn. *Mathematical Handbook for Scientists and Engineers.* McGraw-Hill, New York (1968).

[36] P. A. Kralchevsky and K. Nagayama. Capillary interactions between particles bound to interfaces, liquid films and biomembranes. *J. Colloid Interface Sci.*, **85**, 145 (2000).

[37] M. Boncheva, D. A. Bruzewicz, and G. M. Whitesides. Millimeter-scale self-assembly and its applications. *Pure Appl. Chem.*, **75**, 621 (2003).

[38] G. M. Whitesides and M. Boncheva. Beyond molecules: Self-assembly of mesoscopic and macroscopic components. *Proc. Natl. Acad. Sci. U.S.A.*, **99**, 4769 (2002).

[39] L. Bragg. A model illustrating intercrystalline boundaries and plastic flow in metals. *J. Sci. Instrum.*, **19**, 148 (1942).

[40] L. Bragg and J. F. Nye. A dynamical model of a crystal structure. *Proc. R. Soc. London*, **Ser. A 190**, 474 (1947).

[41] J. C. Loudet, A. G. Yodh, and B. Pouligny. Wetting and Contact Lines of Micrometer-Sized Ellipsoids. *Phys. Rev. Lett.*, **97**, 018304 (2006).

[42] H. Lehle, E. Noruzifar, and M. Oettel. Ellipsoidal particles at fluid interfaces. *Eur. Phys. J. E*, **26**, 151 (2008).

[43] S. Dasgupta, M. Katava, M. Faraj, T. Auth, and G. Gompper. Capillary assembly of microscale ellipsoidal, cuboidal, and spherical particles at interfaces. *Langmuir*, **30**, 11873 (2014).

[44] B. Madivala, J. Fransaer, and J. Vermant. Self-assembly and rheology of ellipsoidal particles at interfaces. *Langmuir*, **25**, 2718 (2009).

[45] R. Daniello, K. Khan, M. Donnell, and J. P. Rothstein. Effect of contact angle on the orientation, stability, and assembly of dense floating cubes. *Phys. Rev. E*, **89**, 023014 (2014).

[46] N. Bowden, I. S. Choi, B. A. Grzybowski, and G. M. Whitesides. Mesoscale self-assembly of hexagonal plates using lateral capillary forces: synthesis using the "capillary bond". *J. Am. Chem. Soc.*, **121**, 5373 (1999).

[47] Bowden, N. B. and Arias, F. and Deng, T. and Whitesides, G. M. Self-assembly of microscale objects at a liquid/liquid interface through lateral capillary forces. *Langmuir*, **17**, 1757 (2001).

[48] D. B. Wolfe, A. Snead, C. Mao, N. B. Bowden, and G. M. Whitesides. Mesoscale self-assembly: capillary interactions when positive and negative menisci have similar amplitudes. *Langmuir*, **19**, 2206 (2003).

[49] I. S. Choi, N. Bowden, and G. M. Whitesides. Shape-selective recognition and self-assembly of mm-scale components. *J. Am. Chem. Soc.*, **121**, 1754 (1999).

[50] M. Weck, I. S. Choi, N. L. Jeon, and G. M. Whitesides. Assembly of mesoscopic analogues of nucleic acids. *J. Am. Chem. Soc.*, **122**, 3546 (2000).

[51] M. Poty, G. Lumay, and N. Vandewalle. Customizing mesoscale self-assembly with three-dimensional printing. *New J. Phys.*, **16**, 023013 (2014).

[52] N. P. Bae, J.and Bende, A. A. Evans, J.-H. Na, C. D. Santangelo, and R. C. Hayward. Programmable and reversible assembly of soft capillary multipoles. *Mater. Horiz.*, **4**, 228 (2017).

[53] J. Metzmacher, M. Poty, G. Lumay, and N. Vandewalle. Self-assembly of smart mesoscopic objects. *Eur. Phys. J. E*, **40**, 108 (2017).

[54] M. Golosovsky, Y. Saado, and D. Davidov. Self-assembly of floating magnetic particles into ordered structures: A promising route for the fabrication of tunable photonic band gap materials. *Appl. Phys. Lett.*, **75**, 4168 (1999).

[55] G. B. Davies, T. Kruger, P. V. Coveney, J. Harting, and F. Bresme. Assembling Ellipsoidal Particles at Fluid Interfaces Using Switchable Dipolar Capillary Interactions. *Adv. Mater.*, **26**, 6715 (2014).

[56] N. Aubry and P. Singh. Physics underlying controlled self-assembly of micro-and nanoparticles at a two-fluid interface using an electric field. *Phys. Rev. E*, **77**, 056302 (2008).

[57] M. Janjua, S. Nudurupati, I. Fischer, P. Singh, and N. Aubry. Electric field induced alignment and self-assembly of rods on fluid–fluid interfaces. *Mech. Res. Commun.*, **36**, 55 (2009).

[58] M. Golosovsky, Y. Saado, and D. Davidov. Energy and symmetry of self-assembled two-dimensional dipole clusters in magnetic confinement. *Phys. Rev. E*, **65**, 061405 (2002).

[59] N. Aubry, P. Singh, M. Janjua, and S. Nudurupati. Micro-and nanoparticles self-assembly for virtually defect-free, adjustable monolayers. *Proc. Natl. Acad. Sci. U.S.A.*, **105**, 3711 (2008).

[60] W. Wen, L. Zhang, and P. Sheng. Planar magnetic colloidal crystals. *Phys. Rev. Lett.*, **85**, 5464 (2000).

[61] N. Vandewalle, N. Obara, and G. Lumay. Mesoscale structures from magnetocapillary self-assembly. *Eur. Phys. J. E*, **36**, 127 (2013).

[62] G. Grosjean, M. Hubert, and N. Vandewalle. Magnetocapillary self-assemblies: Locomotion and micromanipulation along a liquid interface. *Adv. Colloid Interface Sci.*, **255**, 84 (2018).

[63] Y. Collard, G. Grosjean, and N. Vandewalle. Magnetically powered metachronal waves induce locomotion in self-assemblies. *Commun. Phys.*, **3**, 1 (2020).

[64] Y. Collard. *Magnetocapillary self-assemblies: Floating crystals, Metastable states and Locomotion.* PhD thesis, Université de Liège (2022).

[65] K. Creath and J. C. Wyant. Moiré and fringe projection techniques. *Opt. Shop Test.*, **2**, 653 (1992).

[66] S. S. Gorthi and P. Rastogi. Fringe projection techniques: Whither we are? *Opt. Lasers Eng.*, **48**, 133 (2010).

[67] J. Salvi, S. Fernandez, T. Pribanic, and X. Llado. A state of the art in structured light patterns for surface profilometry. *Pattern recognition*, **43**, 2666 (2010).

[68] K.D. Hinsch. Holographic interferometry of surface deformations of transparent fluids. *Appl. Optics*, **17**, 3101 (1978).

[69] S. Yang and G. Zhang. A review of interferometry for geometric measurement. *Meas. Sci. Technol.*, **29**, 102001 (2018).

[70] G. S. Settles. *Schlieren and shadowgraph techniques: visualizing phenomena in transparent media.* Springer Science & Business Media (2001).

[71] N. Degen. An overview on schlieren optics and its applications: Studies on mechatronics (2012). ETH-Zürich.

[72] G. S. Settles and M. J. Hargather. A review of recent developments in schlieren and shadowgraph techniques. *Meas. Sci. Technol.*, **28**, 042001 (2017).

[73] J. Rienitz. Schlieren experiment 300 years ago. *Nature*, **254**, 293 (1975).

[74] A. Przadka, B. Cabane, V. Pagneux, A. Maurel, and P. Petitjeans. Fourier transform profilometry for water waves: how to achieve clean water attenuation with diffusive reflection at the water surface? *Exp. Fluids*, **52**, 519 (2012).

[75] P. J. Cobelli, A. Maurel, V. Pagneux, and P. Petitjeans. Global measurement of water waves by fourier transform profilometry. *Exp. Fluids*, **46**, 1037 (2009).

[76] S. B. Dalziel, G. O. Hughes, and B. R. Sutherland. Synthetic schlieren. In *Proc. 8th Int. Symp. on Flow Visualization*, volume 62 (1998).

[77] G. E. A. Meier. Hintergrund schlierenmessverfahren, *Deutsche Patentanmeldung* (1999). DE 199 42 856 A1.

[78] H. Richard and M. Raffel. Principle and applications of the background oriented schlieren (bos) method. *Meas. Sci. Technol.*, **12**, 1576 (2001).

[79] S. B. Dalziel, G. O. Hugues, and B. R. Sutherland. Whole-field density measurements by 'synthetic schlieren'. *Exp. Fluids*, **28**, 322 (2000).

[80] G. E. A. Meier. Computerized background-oriented schlieren. *Exp. Fluids*, **33**, 181 (2002).

[81] L. Venkatakrishnan and G. E. A. Meier. Density measurements using the background oriented schlieren technique. *Exp. Fluids*, **37**, 237 (2004).

[82] M. Raffel, J. T. Heineck, E. Schairer, F. Leopold, and K. Kindler. Background-oriented schlieren imaging for full-scale and in-flight testing. *J. Am. Helicopter Soc.*, **59**, 1 (2014).

[83] A. Eddi, E. Sultan, J. Moukhtar, E. Fort, M. Rossi, and Y. Couder. Information stored in Faraday waves: the origin of a path memory. *J. Fluid Mech.*, **674**, 433 (2011).

[84] Y. M. Lau, J. Westerweel, and W. van de Water. Using Faraday Waves to Measure Interfacial Tension. *Langmuir*, **36**, 5872 (2020).

[85] A. Eddi, E. Fort, F. Moisy, and Y. Couder. Unpredictable Tunneling of a Classical Wave-Particle Association. *Phys. Rev. Lett.*, **102**, 240401 (2009).

[86] A. P. Damiano, P.-T. Brun, D. M. Harris, C. A. Galeano-Rios, and J. W. M. Bush. Surface topography measurements of the bouncing droplet experiment. *Exp. Fluids*, **57**, 163 (2016).

[87] N. Vandewalle, M. Poty, N. Vanesse, J. Caprasse, T. Defize, and C. Jérôme. Switchable self-assembled capillary structures. *Soft Matter*, **16**, 10320 (2020).

[88] O. K. Sommersel, D. Bjerketvedt, S. O. Christensen, O. Krest, and K. Vaagsaether. Application of background oriented schlieren for quantitative measurements of shock waves from explosions. *Shock Waves*, **18**, 291 (2008).

[89] M. J. Hargather. Background-oriented schlieren diagnostics for large-scale explosive testing. *Shock Waves*, **23**, 529 (2013).

[90] T. Mizukaki, K. Wakabayashi, T. Matsumura, and K. Nakayama. Background-oriented schlieren with natural background for quantitative visualization of open-air explosions. *Shock Waves*, **24**, 69 (2014).

[91] M. J. Hargather and G. S. Settles. Background-oriented schlieren visualization of heating and ventilation flows: Hvac-bos. *HVAC&R Res.*, **17**, 771 (2011).

[92] A. Mazumdar. Principles and techniques of schlieren imaging systems. *Columbia University Computer Science Technical Reports* (2013).

[93] C. Mauger, L. Méès, M. Michard, A. Azouzi, and S. Valette. Shadowgraph, schlieren and interferometry in a 2d cavitating channel flow. *Exp. Fluids*, **53**, 1895 (2012).

[94] K. Kindler, E. Goldhahn, F. Leopold, and M. Raffel. Recent developments in background oriented schlieren methods for rotor blade tip vortex measurements. *Exp. Fluids*, **43**, 233 (2007).

[95] E. Goldhahn and J. Seume. The background oriented schlieren technique: sensitivity, accuracy, resolution and application to a three-dimensional density field. *Exp. Fluids*, **43**, 241 (2007).

[96] J. Kurata, K. T. V. Grattan, H. Uchiyama, and T. Tanaka. Water surface measurement in a shallow channel using the transmitted image of a grating. *Rev. Sci. Instrum.*, **61**, 736 (1990).

[97] F. C. Elwell. *Flushing of embayments*. PhD thesis, University of Cambridge (2005).

[98] F. Moisy, M. Rabaud, and K. Salsac. A synthetic Schlieren method for the measurement of the topography of a liquid interface. *Exp. Fluids*, **46**, 1021 (2009).

[99] J. Kolaas, B. H. Riise, K. Sveen, and A. Jensen. Bichromatic synthetic schlieren applied to surface wave measurements. *Exp. Fluids*, **59**, 128 (2018).

[100] S. Wildeman. Real-time quantitative Schlieren imaging by fast Fourier demodulation of a checkered backdrop. *Exp. Fluids*, **59**, 97 (2018).

[101] L. K. Rajendran, S. P. M. Bane, and P. P. Vlachos. Dot tracking methodology for background-oriented schlieren (BOS). *Exp. Fluids*, **60**, 162 (2019).

[102] M. Grédiac, B. Blaysat, and F. Sur. Comparing several spectral methods used to extract displacement fields from checkerboard images. *Opt. Lasers Eng.*, **127**, 105984 (2020).

[103] T. Utami and R. E. Blackwelder. A cross-correlation technique for velocity field extraction from particulate visualization. *Exp. Fluids*, **10**, 213 (1991).

[104] C. D. Meinhart, S. T. Wereley, and J. G. Santiago. PIV measurements of a microchannel flow. *Exp. Fluids*, **27**, 414 (1999).

[105] R. J. Adrian. Twenty years of particle image velocimetry. *Exp. Fluids*, **39**, 159 (2005).

[106] P. Meunier and T. Leweke. Analysis and treatment of errors due to high velocity gradients in particle image velocimetry. *Exp. Fluids*, **35**, 408 (2003).

[107] M. Bornert, F. Brémand, P. Doumalin, J.-C. Dupré, M. Fazzini, M. Grédiac, F. Hild, S. Mistou, J. Molimard, J.-J. Orteu, L. Robert, Y. Surrel, P. Vacher, and B. Wattrisse. Assessment of Digital Image Correlation Measurement Errors: Methodology and Results. *Exp. Mech*, **49**, 353 (2009).

[108] E. Meinhardt-Llopis, J. Sánchez, and D. Kondermann. Horn-schunck optical flow with a multi-scale strategy. *Image Proc. On Line*, **3**, 151 (2013).

[109] P. Weinzaepfel, J. Revaud, Z. Harchaoui, and C. Schmid. DeepFlow: Large Displacement Optical Flow with Deep Matching. In *Proceedings of the IEEE International Conference on Computer Vision (ICCV)*, page 1385 (2013).

[110] S. Wildeman. Matlab implementations of fcd and dic+of methods, *GitHub* (2018). https://github.com/swildeman/fcd, https://github.com/swildeman/dicflow.

[111] M. Raffel, C. E. Willert, and J. Kompenhans. *Particle image velocimetry: a practical guide.* Springer, Heidelberg (1998).

[112] R. R. A. Syms, E. M. Yeatman, V. M. Bright, and G. Whitesides. Surface Tension-Powered Self-Assembly of Microstructures–The State-of-the-Art. *J. Microelectromech. Sys.*, **12**, 387 (2003).

[113] A. Demortière, A. Snezhko, M. V. Sapozhnikov, N. Becker, T. Proslier, and I. S. Aranson. Self-assembled tunable networks of sticky colloidal particles. *Nature Comm.*, **5**, 3117 (2014).

[114] N. Adami, A. Delbos, B. Roman, J. Bico, and H. Caps. Elasto-capillary collapse of floating structures-non-linear response of elastic structures under capillary forces. *arXiv preprint arXiv:1310.0329* (2013).

[115] W.-J. A. de Wijs, J. Laven, and G. de With. Wetting Forces and Meniscus Pinning at Geometrical Edges. *AIChE J.*, **62**, 4453 (2016).

[116] E. Diller, N. Zhang, and M. Sitti. Modular micro-robotic assembly through magnetic actuation and thermal bonding. *J. Micro-Bio Robot*, **8**, 121 (2013).

[117] A. Snezhko and I. S. Aranson. Magnetic manipulation of self-assembled colloidal asters. *Nature Mat.*, **10**, 698 (2011).

[118] G. Lumay, N. Obara, F. Weyer, and N. Vandewalle. Self-assembled magnetocapillary swimmers. *Soft Matter*, **9**, 2420 (2013).

[119] G. Grosjean, G. Lagubeau, A. Darras, M. Hubert, G. Lumay, and N. Vandewalle. Remote control of self-assembled microswimmers. *Sci. Reports*, **5**, 16035 (2015).

[120] L. D. Landau and E. M. Lifshitz. *Fluid Mechanics*. Pergamon Press, New York, 2nd edition (1987).

[121] D. J. Acheson. *Elementary fluid dynamics*. Clarendon Press, Oxford (1990).

[122] E. Raphaël and P.-G. De Gennes. Capillary gravity waves caused by a moving disturbance: wave resistance. *Phys. Rev. E*, **53**, 3448 (1996).

[123] J. W. M. Bush and D. L. Hu. Walking on water: biolocomotion at the interface. *Annu. Rev. Fluid Mech.*, **38**, 339 (2006).

[124] D. L. Hu and J. W. M. Bush. The hydrodynamics of water-walking arthropods. *Journal of Fluid Mechanics*, **644**, 5 (2010).

[125] B. Kwak and J. Bae. Locomotion of arthropods in aquatic environment and their applications in robotics. *Bioinspir. Biomim.*, **13**, 041002 (2018).

[126] B. Kwak, S. Choi, J. Maeng, and J. Bae. Marangoni effect inspired robotic self-propulsion over a water surface using a flow-imbibition-powered microfluidic pump. *Sci. Rep.*, **11**, 17469 (2021).

[127] S. H. Suhr, Y. S. Song, S. J. Lee, and M. Sitti. Biologically inspired miniature water strider robot. In *Robot. Sci. Syst.*, volume 2005, page 319 (2005).

[128] E. Rhee, R. Hunt, S. J. Thomson, and D. M. Harris. Surferbot: a wave-propelled aquatic vibrobot. *Bioinspir. Biomim.*, **17**, 055001 (2022).